ABSTRACT

Title of Document:	DEVELOPMENT AND TESTING OF A MULTIPLEXED TEMPERATURE SENSOR
	Gregory William Anderson, Ph.D. 2008
Directed By:	Professor Marino di Marzo, Department of Mechanical Engineering
	Professor Jungho Kim, Department of Mechanical Engineering

Researchers studying phenomena associated with steep surface temperature gradients, such as boiling, need to be able to obtain a detailed surface temperature distribution. Such a distribution can be obtained by taking measurements at a number of discrete locations on the surface using multiple individual temperature sensors. Because each sensor requires at least two electrical connections, this approach has historically been limited to relatively few temperature measurements; the most extensive measurements made this way are still limited to a 10×10 array.

A new temperature sensor has been developed to address this measurement problem. The new sensor consists of a 32×32 array of diode temperature sensors in a 10.24 mm^2 area, with each component diode measuring 100×100 μm^2. Unlike previous array-type sensors, the new sensor uses a multiplexing scheme to reduce the number of external leads required; only 64 leads are required to obtain measurements from over 1000 individual temperature sensors. The new sensor also incorporates eight resistive

heater elements to provide the heat flux to initiate and sustain boiling. The heaters are capable of delivering up to 100 W/cm^2.

This dissertation describes the design and testing of the new temperature sensor and the supporting hardware and software. The system is demonstrated by determining the local heat transfer coefficients for a jet of FC-72 from a 0.241 mm diameter nozzle. The surface temperature distribution is measured for various combinations of applied heat flux, jet velocity, and nozzle standoff distance; these measurements are then used to determine the local heat transfer coefficient distribution. These measured values compare favorably to those predicted using several correlations available in the literature.

DEVELOPMENT AND TESTING OF A MULTIPLEXED TEMPERATURE SENSOR

By

Gregory William Anderson

Dissertation submitted to the Faculty of the Graduate School of the
University of Maryland, College Park in partial fulfillment
of the requirements for the degree of
Doctor of Philosophy
2008

Advisory Committee:
Professor Marino di Marzo, Co-chair
Professor Jungho Kim, Co-chair
Professor Avram Bar Cohen
Professor Patrick McCluskey
Professor Gary Pertmer

Dedication

For my mother, Sandra Lee Anderson (1944 – 2001).

Acknowledgments

First and foremost, I wish to express my sincere thanks to my advisors, Dr. Marino di Marzo and Dr. Jungho Kim. It was their support, guidance, encouragement, and insight that made this dissertation possible, and I am grateful for the opportunity to work with them.

I would like to thank my friends and colleagues from the Phase Change Heat Transfer Lab — Jack Coursey, Rishi Raj, Payam Delgoshaei, Bahman Abassi, Kevin Moores, Thierry Some, Zan Liu, Hitoshi Sakamoto, Chris Henry, and the revolving German exchange students, Alex Waltzenbach, Martin Karch, and Patrick Schrimpf. It has been an honor and privilege, not to mention an awful lot of fun, working with them. I would also like to thank Jack Touart from the Physics department, and Dr. Zeynep Dilli and Dr. Neil Goldsman for their suggestions and corrections in the semiconductor design.

I would also like to thank my friends and coworkers at the Naval Surface Warfare Center, past and present — Steve Mastro, Mark Zerby, Joe Sullivan, Chris Dafis, Jack Overby, Mike Zink, Frank Ferrese, Don Longo, K. J. Brown, Mark Roberts, Mike Kuszewski, and Sam Doughty.

I am also grateful for the support I have received from my supervisors during the time I have been with the Navy. I would like to thank Dr. Peter Cho, Dr. Mike Golda, Ana Gulian, Al Ortiz, and Dr. Laura Stubbs for their management support (and their patience). I would like to thank Dr. John Barkyomb, Charlie Zimmerman, and the

iii

Table of Contents

List of Tables

List of Figures

xi

Nomenclature

a	Temperature coefficient in plane calibration (mV/°C)
[A]	Matrix of coefficients for 3-D conduction solver
A_{array}	Area covered by the diode array [mm^2]
A_j	P-n junction area [m^2]
A_{top}	Area of the top of the diode array chip [mm^2]
A/D	Analog/Digital converter
ADI	Alternating Direction Implicit
ASIC	Application Specific Integrated Circuit
$\vec{B}$	Vector of coefficients for 3-D conduction solver
b_2	Y-intercept in line equation [°C]
b_3	Offset voltage coefficient in plane calibration equation [mV/mV]
c	Specific heat [mJ/kg K]
C_1	Coefficient in thermocouple equation [V/°C]
C_2	Coefficient in thermocouple equation [V/°C]
CHF	Critical heat flux
D	Nozzle diameter [mm]
	Depth (z-direction) of the 3-D conduction solver solution domain [mm]
D/A	Digital/Analog converter
DAQ	Data acquisition
DIP	Dual inline package

D_n	Electron diffusion coefficient
D_p	Hole diffusion coefficient
E_g	Bandgap energy [eV or J]
EMI	Electromagnetic interference
fps	Frames per second
G	Instrumentation amplifier gain for main signal conditioning circuit
G_{offset}	Instrumentation amplifier gain for DC offset monitoring circuit
GUI	Graphical user interface
H	Height (y-direction) of the 3-D conduction solver solution domain [mm]
HSI	Hue – saturation – intensity color space
h_{local}	Local heat transfer coefficient [mW/mm^2 K]
h_{surf}	Heat transfer coefficient at diode array chip surface [mW/mm^{2}K]
I_0	Saturation current [A]
I_D	Diode current [A]
I_s	Saturation current [A]
k	Thermal conductivity [mW/mm K]
	Boltzmann's constant [J/K]
LASI	LAyout System for Individuals
L	Length (x-direction) of the 3-D conduction solver solution domain [mm]
L_n	Electron diffusion length
L_p	Hole diffusion length
LSB	Least significant bit

m	Temperature coefficient in 2-D linear calibration [mV/°C]
M	Number of discretized elements in the x-direction
MFC	Microsoft Foundation Classes
MOSIS	Metal Oxide Semiconductor Implementation Service
N	Number of discretized elements in the y-direction
N_A	Acceptor concentration [m^{-3}]
N_D	Donor concentration [m^{-3}]
n_i	Intrinsic silicon concentration [m^{-3}]
Nu	Nusselt number
P	Number of discretized elements in the z-direction
PCB	Printed circuit board
PGA	Pin grid array
Pr	Prandtl number
q	Elementary charge on an electron [C]
q''	Heat flux [mW/mm^2]
q''_{local}	Local heat flux [mW/mm^2]
Q	Power generation [W]
r	Radius [mm]
r^2	Regression coefficient
R	Resistance [Ω]
R_0	Resistance at reference temperature [Ω]
R_g	Value for instrumentation amplifier gain resistor [Ω]

R_H	Heater resistance [Ω]
R_p	Parasitic resistance [Ω]
R_s	Stabilization resistor [Ω]
Re	Reynolds number
RGB	Red – green – blue color space
RTD	Resistance temperature device
SIP	Single inline package
SPDT	Single pole double throw switch
T	Temperature [°C]
T_1	Temperature of junction 1 in thermocouple circuit [°C]
T_2	Temperature of junction 2 in thermocouple circuit [°C]
TCLC	Thermochromic liquid crystal
UL	Universal Library
V	Voltage [V]
V_B	Bandgap voltage [V]
V_D	Voltage drop across diode [V]
V_{DC}	DC offset voltage [mV]
$V_{D/A}$	Voltage output by D/A on data acquisition board [mV]
$V_{DCbaseline}$	Nominal DC offset voltage delivered by power supply [mV]
V_m	Measured voltage [mV]
V_{pn}	Voltage drop associated across only the p-n junction [mV]
V_{tc}	Thermocouple voltage [V]

W_n'	Neutral n-type region [m]
W_p'	Neutral p-type region [m]
x	x-coordinate [mm]
y	y-coordinate [mm]
z	z-coordinate [mm]
ZIF	Zero insertion force

Greek

α	Thermal diffusivity [m^2/s]
α_{Is}	Algebraic substitution parameter for parasitic resistance regression equation [mV]
α_R	Temperature coefficient of resistance [$°C^{-1}$]
ΔT	Temperature difference [°C]
Δt	Time step [s]
ΔV	Change in voltage [V]
ΔV_{dc}	DC offset voltage fluctuation [V]
Δx	Size of discretized element in x-direction [mm]
Δy	Size of discretized element in y-direction [mm]
Δz	Size of discretized element in z-direction [mm]
γ	Constant in Blackburn's saturation current equation [—]
ρ	Density [kg/mm^3]

Subscripts

k	current time step index

m	Index of discretized element in the y-direction
n	Index of discretized element in the x-direction
p	Index of discretized element in the z-direction

Chapter 1: Introduction

General Overview

To the lay person, the boiling process might seem to be a simplistic choice of topics for detailed and rigorous scientific research. Put a pot of water on the stove and start heating it: when the water reaches 100 °C, it begins to bubble and steam. Boiling is such a familiar phenomenon that when someone is particularly inept in the kitchen, he is often described as being "unable to boil water."

Boiling is prevalent outside the kitchen as well. Medical instruments are sterilized by boiling, and industrial boilers produce superheated steam to drive turbines for power generation. In power electronics and advanced computing, the relentless drive to make smaller and faster chip is producing ever escalating waste heat fluxes. Boiling and other phase change cooling solutions are promising candidates for managing this waste heat because they transfer large heat fluxes over relatively small temperature differences; this is particularly important in electronics cooling, where devices must be maintained below certain temperatures for reliability reasons.

Looking more closely at what is really happening at or near the heater surface, the casual familiarity starts to break down, revealing many subtle and challenging questions. Despite decades of research, at the sub-millimeter scale — the length scale of the individual bubbles — the phenomena taking place are still not well understood. Complicating matters further is the time scale — a bubble exists for only a few milliseconds, and a new bubble forms to replace it only a few milliseconds after it

departs. During its short life, the bubble's growth depends on a three-dimensional, time-varying flow field incorporating both liquid and vapor. From a mathematical perspective, calling the problem "intractable" is still an understatement. Abandoning the search for a complete analytical solution and approaching the problem numerically helps, but even the most advanced numerical solutions are currently limited to considering the simultaneous interactions of only a few bubbles at a time for short periods of time.

Considering the problem from an experimental perspective, the researcher faces substantial challenges. The small length and time scales associated with these phenomena require small, highly responsive instruments. To further complicate matters, the local flow field has a strong influence on the heat transfer to the bubbles and their resulting growth rate, thus intrusive instruments that disrupt the flow field may seriously disturb the phenomena being studied.

Although there are serious instrumentation obstacles to boiling research, they can be overcome. On the macroscopic scale — where most engineering applications take place — many models have been developed with varying degrees of success. On the microscopic scale, researchers have devised successively more ingenious solutions to the instrumentation problem, taking advantage of advances in microelectronic fabrication to develop increasingly smaller and more responsive instruments. They then develop larger sensors by combining many of these small instruments.

Phenomena Background

This dissertation describes the development of a new temperature sensor intended for use studying boiling and demonstrated using jet impingement. The dissertation opens

therefore with a brief discussion of the state of the art in understanding boiling, followed by a brief discussion of single phase jet impingement. This is followed by a discussion of thermometry in general.

Boiling

Boiling is defined in a variety of ways in the literature, but the common elements among the many definitions are a) heat transfer to a liquid at or exceeding its saturation temperature and b) a change of phase from liquid to vapor. These definitions encompass a wide variety of heat transfer phenomena, and boiling is typically classified in a number of ways:

• Flow vs. pool: in flow boiling (also called convective boiling) the bulk liquid is in motion relative to the heater surface; in pool boiling the fluid is stationary relative to the heater surface.

• Saturated vs. subcooled: in saturated boiling, the bulk fluid is at the saturation temperature; in subcooled boiling the fluid is at a lower temperature.

The following discussion considers only pool boiling.

Although boiling is not a "solved problem," there are characteristics that are widely accepted within the boiling community. The most obvious example of these is the boiling curve. The boiling curve, attributed [1] to Nukiyama's seminal paper [2] (in which he also first identified critical heat flux), provides a broad overview of the boiling process. It relates the surface temperature to the heat flux throughout the complete range of boiling phenomena, as shown in Figure 1.
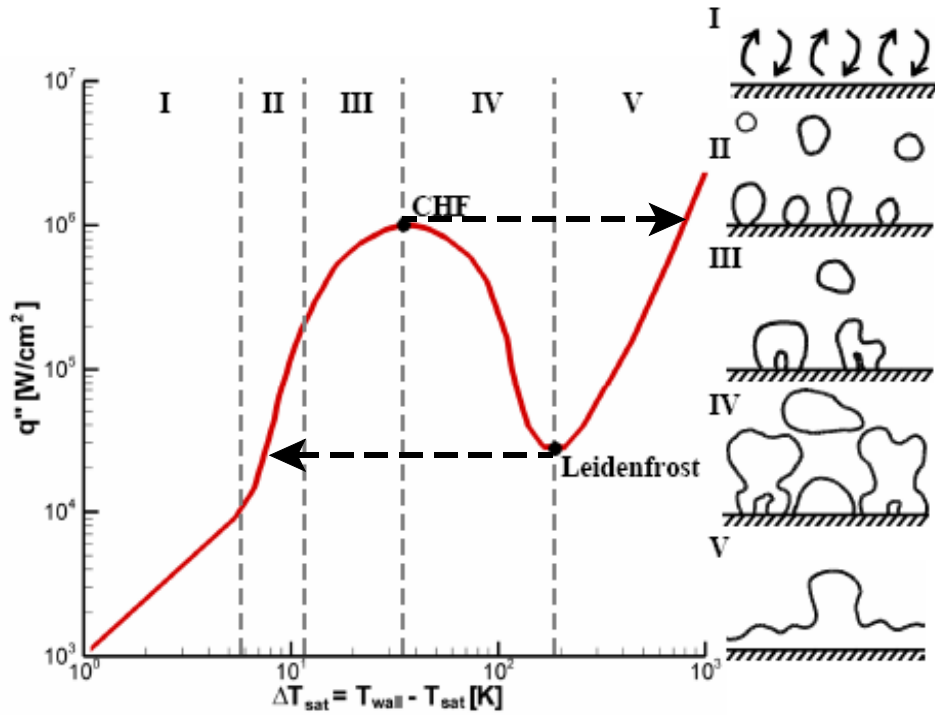
Figure 1   Boiling curve (after Coursey [3])

Using the boiling curve, boiling is divided into five regimes; to better illustrate

these regimes, consider a container of water heated from below. As the water is heated

from room temperature, the energy supplied increases the water temperature. This

temperature increase continues until the water near the heater surface reaches its

saturation temperature; this marks the beginning of regime I, natural convection. Because

liquid at its saturation temperature does not undergo a phase change to vapor unless it is

already in contact with some vapor, bubbles do not yet form in regime I. As the liquid

continues to be heated past its saturation temperature, bubbles begin to form at tiny pits

and cavities on the heater surface, known as nucleation sites. Their formation marks the

transition to regime II, nucleate boiling. Nucleate boiling is associated with a sharp

4

increase in the heat transfer coefficient; thus even a small increase in heater temperature is associated with a significant heat flux. At first, the bubbles nucleate, grow, and depart slowly enough that there is a distinct separation between each bubble and the next; for this reason, regime II is also known as the individual bubble regime. As the heating continues, the waiting time between bubbles decreases, so that one bubble will have barely departed before the next nucleates, until the bubbles merge into continuous columns of vapor rising from the surface. This marks the beginning of regime III, the regime of slugs and columns, also known as the high-heat-flux nucleate boiling regime. This process cannot continue indefinitely; eventually, vapor is produced so rapidly that it interferes with the liquid flow to the heater. The heat flux at which this occurs is known as the critical heat flux (CHF), and it marks the beginning of regime IV, transition boiling. In this regime, large portions of the heater are covered by a vapor blanket, and liquid only makes intermittent contact with the heater surface; for this reason, the transition regime is also known as the partial film boiling regime [4]. This regime is also characterized by a decrease in the heat transfer coefficient as the surface temperature increases. This creates an unstable condition. The red line in Figure 1 can only be obtained if the heater surface temperature is carefully controlled. In most practical situations, the power dissipated by the heater is controlled, rather than the heater surface temperature, and exceeding CHF causes a sudden increase in heater temperature as the system enters regime V, film boiling. This is indicated by the dashed arrow away from CHF in Figure 1. The sudden temperature increase often has catastrophic effects on the heater, and CHF is also referred to as the burnout heat flux. In the film boiling regime, a

5

continuous vapor blanket covers the entire heater, and the heater surface is so hot that conduction through this blanket is sufficient to evaporate the liquid on the other side. The surface temperature at which the vapor film becomes stable is known as the Leidenfrost point. If the heater is subsequently cooled after entering the film boiling regime, an interesting hysteresis effect becomes evident. The surface will follow the red line in Figure 1 until the surface temperature reaches the Leidenfrost point and the vapor blanket collapses. If the heater power is controlled, this collapse is associated with the dashed arrow away from the Leidenfrost point back to regime II, nucleate boiling. If the heater temperature is carefully controlled instead, the system will retrace the red line, and the heater will traverse the transition boiling regime again.

The distinction between subcooled and saturated boiling can be thought of as shifting the boiling curve upwards. Subcooling tends to enhance heat transfer in the natural convection regime by increasing the temperature difference. In the nucleate boiling regime, subcooling has little effect. CHF is strongly affected by subcooling, however; one explanation for this suggests that the rising vapor columns condense in the subcooled bulk liquid, which allows more liquid to reach the surface [5]. Another explanation suggests that the increase in CHF is explained by the sensible heating required to raise the bulk fluid to the saturation temperature [5]. The latter explanation may also explain why subcooling also increases heat transfer in the transition regime, although as Carey explains, there are no quantitative estimates for the magnitude of the effect [5]. Finally, film boiling shows some degree of enhancement due to subcooling,

but the magnitude of the effect decreases as the heat flux and surface temperature increase [5].

Early work in boiling focused primarily on the boiling curve, and although the curve is still used, later researchers recognized that a better understanding of local processes is critical for developing a deeper understanding of boiling.

The ebullition cycle, which describes the life cycle of an individual bubble, offers a useful framework for studying these local processes. There are many different
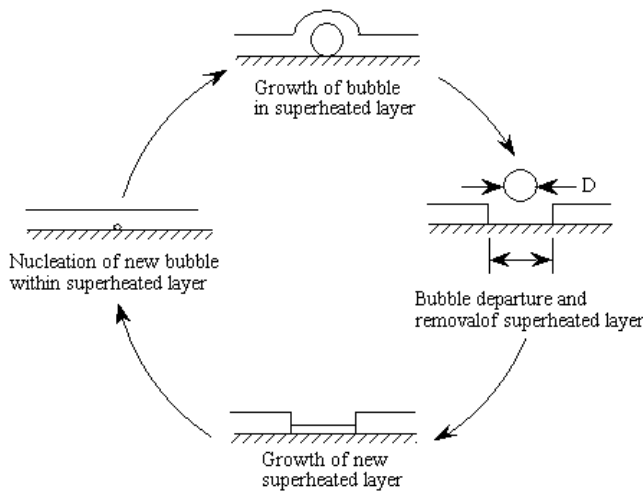
Figure 2   Ebullition Cycle (after Kim [6])

representations for the ebullition cycle, but one candidate model is depicted in Figure 3 [6]. According to this model, the cycle begins with the growth of a superheated liquid layer adjacent to the surface. At some point, a bubble forms at an active nucleation site, which then grows and departs, carrying away superheated liquid in the process. As a new superheated liquid layer begins to grow, the cycle continues.

7

Within the framework of the ebullition cycle, questions about local phenomena governing boiling take shape. Some questions pertain to bubble nucleation — what causes a site to become active (or to become inactive)? How do nearby sites interact? How does the geometry of the site affect its behavior? Other questions pertain to bubble growth — how much of the energy required to vaporize the liquid is provided by the superheated layer around the growing bubble and how much is provided by the heater surface directly? Of the heater's contribution, how much is delivered by microlayer evaporation compared to thin film evaporation? Still other questions pertain to bubble departure — what role does surface tension play in bubble departure? How does gravity affect departure? How much does the local fluid motion influence departure? As the bubble departs, how much of the superheated liquid does it carry away? After the bubble departs, how long does it take for the next bubble to nucleate? Will the same site produce another bubble, or will a nearby site produce the next one?

There are many plausible answers to these questions, and resolving them depends on making highly detailed surface temperature and surface heat flux measurements. The measurement techniques commonly in use, described in detail in Chapter 2, are restricted in their ability to obtain these distributions. Electrical sensors, such as thermocouples and RTDs, are capable of high speed measurements but are difficult to implement in large numbers. Optical techniques, such as liquid crystal thermography, are capable of making measurements at many locations but are limited to low frequencies. Optical methods also impose serious restrictions on the experiment design.

This dissertation describes a new device using electrical sensors (diodes) that combines the optical techniques' ability to make measurements at many locations with the electrical sensors' ability to take high speed measurements.

Single Phase Jet Impingement

The ability of the new sensor to obtain a detailed surface temperature distribution is demonstrated using single phase jet impingement. The behavior of a single round jet impinging on a flat surface is well characterized and provides an excellent test case.

As with boiling, the literature defines jet impingement in a variety of ways. These definitions can be summarized as: a coherent stream of a fluid issuing from an orifice and striking a surface. Also like boiling, this definition encompasses many configurations, which are classified in the following ways:

- Single phase or boiling: in single phase jets, the heat transfer is limited to sensible heating or cooling, while in jet impingement boiling, the heat transfer also includes a contribution due to the latent heat of the fluid.

- Orifice shape: common orifice shapes are round elliptical, or a long, narrow slot.

- Free-surface or submerged: in a submerged jet, the fluid is discharged into a surrounding fluid with the same phase, e.g. a liquid jet into a liquid environment or a gaseous jet into a gaseous environment. In a free-surface jet, a liquid jet is discharged into a gaseous environment.

- Number, spacing, and pattern of jets: whether the jet is singular or part of an array. If it is part of an array, how far apart are the individual nozzles, and how are they arranged (rectangular array, staggered, etc.)

9

The present work is concerned with only a single, round, single phase, submerged jet.

There are three regions in a typical jet, illustrated schematically in Figure 3. The first region is the free jet and includes the fluid stream between the nozzle and the location at which the surface begins to influence the flow pattern. Within this region, jet entrains fluid from the environment, causing it to slow down and become wider. The second region is the impingement (or stagnation) zone and includes the region immediately surrounding the point of impingement. Within this region, the heat transfer coefficients can be very large. The third region is the wall jet and includes the fluid moving away from the point of impingement. This region is characterized by a decreasing heat transfer coefficient with increasing distance from the stagnation point.
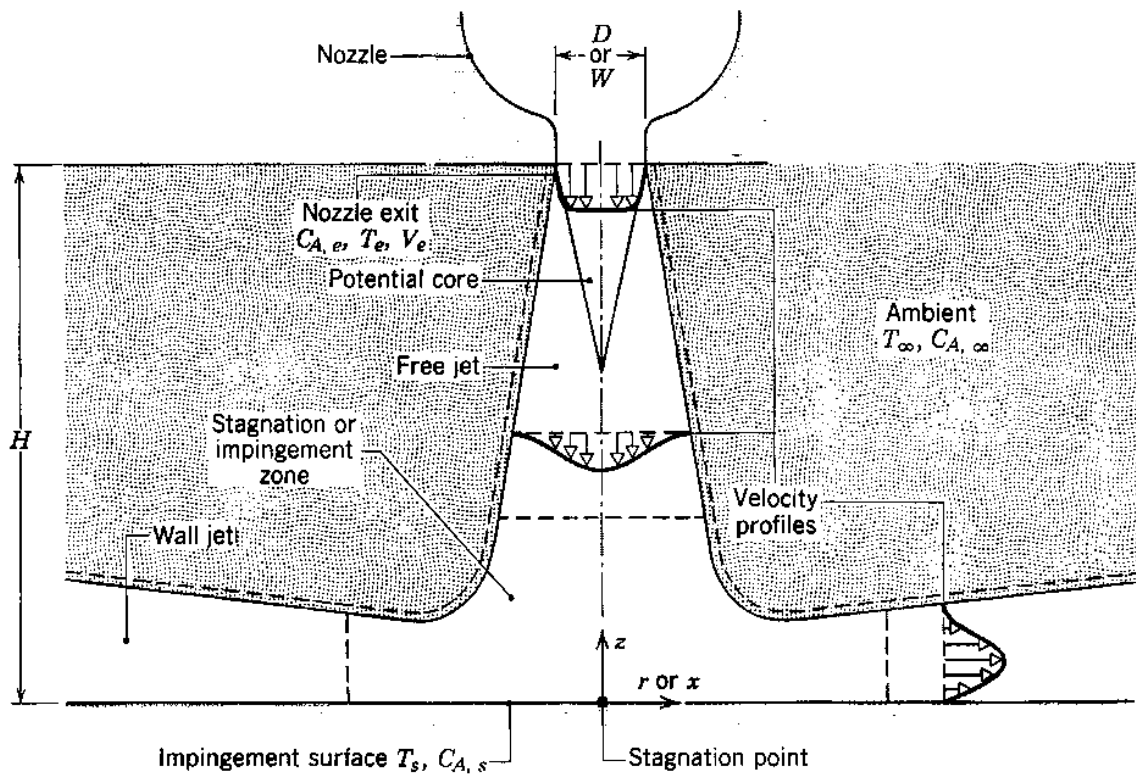
Figure 3   Schematic of submerged impinging jet (From Incropera & DeWitt [7])

Early work in jet impingement primarily focused on determining an average heat transfer coefficient for the surface. The review of early work conducted by Martin [8] is still considered by many researchers to be definitive; this review focused primarily on gas jets. A later review by Webb and Ma [9] discusses both free and submerged liquid jets; a still later review by Zuckerman and Lior [10] discusses the effect of turbulence on the heat transfer.

Temperature and Temperature Measurement

There are generally two types of definition for temperature:

- The relative, intuitive definition of "hot" and "cold."

- A rigorous, physical definition that relates the temperature to the average kinetic energy of the constituent particles in the material [11].

Unfortunately, neither of these definitions lends itself to a convenient practical approach to temperature measurement. However, just as the concepts of "hot" and "cold" are familiar, the concept of "thermal equilibrium" is also familiar. Put simply, thermal equilibrium refers to the tendency of hot and cold objects to reach the same level of "hotness" or "coldness" when they have been left in contact with each other for a long time; this concept is inherent in the second definition of temperature described above. This observation leads to the zeroth law of thermodynamics, which states: "If two systems are separately in thermal equilibrium with a third, then they are in thermal equilibrium with each other." [12] By associating a specific temperature with that state of thermal equilibrium, the zeroth law gives practicality to the second definition stated

above. The zeroth law also enables the measurement of temperature, because the "third system" may be a measurement device.

The first device for measuring temperature was invented by Galileo in the late 16th century [13], although there is evidence that other inventors developed similar instruments at about the same time [14]. These early "thermoscopes" used the expansion of air with temperature, later known as Boyle's Law, to distinguish one temperature from another [14], but they did not employ any sort of quantitative scale. Sometime later, around the middle of the 17th century, scientists began using liquid in glass thermometers; these used the expansion of various liquids — typically mercury or some type of alcohol — to distinguish between temperatures [12], but they also lacked a standard scale based on repeatable calibration points [13]. Although the ancient Greek physician Galen established the first temperature scale based on nine points (four each above and below some middle point derived from mixing equal parts boiling water and ice) [14], the first widely accepted temperature scale for scientific purposes was developed by D. Gabriel Fahrenheit in 1724; soon after, Anders Celsius followed with an alternative scale in 1742 [13]. In the 19th century, Lord Kelvin suggested that there is a temperature at which all thermal motion should stop; he termed this "absolute zero" and determined that it should correspond to -273.15 °C [13]. Today, the SI system considers the kelvin to be one of the seven base units from which all other recognized units are derived [15].

Unlike other quantities, such as length, temperature is not compared directly against some reference standard; instead, temperature is measured through its indirect effect on some other property. Because so many material properties have some degree of

temperature dependence, there are potentially many types of thermometers. Table 1

presents some types of temperature sensors. As noted previously, the first three types –

liquid in glass, constant volume gas, and constant pressure gas – were among the earliest

thermometers. These three types represent only a small fraction of the options available

for temperature measurement. Of the thermometers developed since then, the operating

principles range from the very simple, such as the heat sensitive paints and crayons,

which melt at a pre-determined temperature, to the very complicated, such as coherent

anti-Stokes Raman scattering, which requires a sophisticated laser and spectrometer

assembly.

Table 1   Types of temperature sensors (from Childs [16])

	Sensor type	Temperature dependent property	Measured quantity
1	Liquid-in-glass thermometer	Thermal expansion	Length
2	Constant volume / pressure gas thermometer	Thermal expansion	Pressure / Volume
3	Bimetallic strip	Thermal expansion	Length
4	Thermocouple	Seebeck effect	Voltage
5	Platinum RTD	Electrical resistance	Resistance
6	Thermistor	Electrical resistance	Resistance
7	Diode / Transistor	Electrical conductance	Voltage
8	Capacitance thermometer	Electric permittivity	Capacitance
9	Noise thermometer	Johnson noise	Power
10	Quartz thermometer	Vibration	Time
11	Paramagnetic thermometer	Vibration	Inductance
12	Nuclear magnetic resonance thermometer	Vibration	Inductance
13	Thermochromic liquid crystals	Reflection	Color
14	Thermographic phosphors	Fluorescence	Intensity
15	Heat sensitive crayons / paints	Chemical	Color
16	Pyrometric cones	Chemical	Shape
17	Infrared thermometer / thermal imager	Thermal radiation	Radiation intensity
18	Schlieren	Density	Wavelength
19	Inferometry	Density	Interference fringes
20	Line reversal	Density	Color
21	Absorption / Emission Spectroscopy	Absorption / Emission	Wavelength
22	Rayleigh / Raman scattering	Elastic / Inelastic scattering	Wavelength
23	Coherent anti-Stokes Raman scattering	Scattering	Wavelength
24	Degenerative four wave mixing	Scattering	Wavelength
25	Laser-induced fluorescence	Emission	Time
26	Speckle methods	Interference	Length
27	Acoustic thermography	Sound velocity	Time

According to Childs [16], there are nine criteria to be considered when selecting a temperature measurement sensor, listed in Table 2. Note that not all of these criteria are independent. For example: level of contact affects the thermal disturbance; sensor size affects both transient response and thermal impact; and uncertainty profoundly affects cost. Additionally, certain criteria are closely related and are likely to be considered

Table 2   Temperature sensor selection criteria (after Childs [16])

No.	Criterion	Description	
1	Uncertainty	Amount by which the reported value might reasonably be expected to deviate from the actual value	Accuracy
2	Thermal Disturbance	Degree to which the presence of the sensor disrupts the local temperature field in the vicinity of the sensor	
3	Sensor Size	Amount of the material being measured with which the sensor will interact	Objective
4	Transient Response	Rapidity with which changes in the local temperature field can be identified and reported by the sensor	
5	Availablity	Amount of preparation necessary before using the sensor	Logistical
6	Cost	Financial and logistical impact of acquiring and using the sensor	
7	Temperature Range	Span of temperatures for which a measurement is possible	Other
8	Level of Contact	Degree to which the sensor must directly interact physically with the material being measured	
9	Sensor Protection	Vulnerability of the sensor to damage due to conditions within the material being measured (reactivity, physical impact, etc.)	

together. Uncertainty and thermal disturbance both directly contribute to the fidelity of the measurement and are grouped together under the heading "Accuracy." The sensor size (spatial resolution) and transient response (temporal resolution) together represent the primary direction of the present research, so they are grouped together under the heading "Objective." The availability and cost criteria both primarily affect the

acquisition and operation of the equipment, so they are grouped together under the

heading "Logistics." The remaining criteria are collected together into a fourth category,

"other," not so much because they are closely related to each other so much as they are

not closely related to any of the previous criteria

Dissertation Objectives

This dissertation describes the development of a new temperature sensor. This new sensor should achieve the following goals:

- Incorporate a 32 × 32 array of diodes.

- Achieve 100 μm spatial resolution.

- Incorporate resistive heaters to produce up to 100 W/cm^2.

- Achieve 1 kHz data collection rate.

- Demonstrate the ability to measure the local heat transfer distribution for an impinging jet.

Dissertation Structure

This new sensor uses a multiplexing scheme to share leads among a 32 × 32 array of diodes; although there are over 1000 individual diodes only 64 electrical connections are required. The sensor is designed to acquire data over the entire array at 1 kHz. Because the new sensor also incorporates eight heaters capable of supply a heat flux of up to 100 W/cm^2, it provides a self-contained test platform for boiling research that combines the strengths of optical temperature measurement techniques (many measurements) with the advantages of electrical sensors (high speed).

Chapter 2 presents a review of the temperature measurement techniques currently employed by boiling and jet impingement researchers.

Chapter 3 provides an overview of the diode array design. This chapter opens with an discussion of semiconductor behavior, followed by a discussion of diode

behavior and the nature of their temperature sensitivity. It concludes with a summary of the specific diode array designs.

Chapters 4 and 5 describe the hardware and software developed to support the diode array sensor. Chapter 4 discusses the interface board and data acquisition hardware and software. Chapter 5 discusses the 3-D conduction solver used to determine the heat flux delivered to the fluid based on the surface temperature distribution. Chapter 5 also discusses a finite element model of the diode array used in conjunction with the 3-D conduction solver.

Chapters 6 describes the tests conducted to characterize and demonstrate the sensor's behavior. Chapter 6 reports on the characterization tests, which include: single-diode and full-array calibrations to determine the temperature response, a transient test to determine the response time, tests over a range of sensing currents to determine the parasitic resistance, and a natural convection test to identify faulty diodes and verify substrate conduction losses.

Chapter 7 reports on the jet impingement performed to demonstrate the diode array. These tests varied the surface heat flux, the nozzle flow rate, and the nozzle standoff distance. The local heat flux was determined using the 3-D conduction solver, and the resulting heat transfer coefficients were compared against the values predicted by several correlations available in the literature.

Finally, Chapter 8 summarizes the major features of the dissertation and presents suggestions for future work.

Chapter 2: Literature Review

Introduction

Temperature measurement is a fundamental activity in heat transfer research, and researchers have developed many techniques for making these measurements. The most commonly used techniques in boiling and jet impingement research are thermocouples, resistance temperature devices, and thermochromic liquid crystals; these approaches will be discussed further in the sections that follow. A final section discusses the use of diode thermometers. Although other techniques are used as well — infrared cameras and liquid-in-glass thermometers, for example (see Theofanous, et al. [17], Hofmann, et al.[18], and Kohn and Popa [19]) — they represent a small fraction of the research and will not be discussed.

Thermocouples

For many temperature measurement applications, the thermocouple is the predominant temperature sensor. Simple and inexpensive, a thermocouple is produced by joining two different materials and operates according to the Seebeck effect, in which a temperature gradient in a material induces a small electrical potential [20]. Because of the Seebeck effect, a thermocouple subjected to a temperature difference produces a potential difference; the magnitude of this potential difference is related to the temperature difference that produced it according to Eq. 2:

$$V_{tc} = C_1\left(T_1 - T_2\right) + C_2\left(T_1^2 - T_2^2\right) \tag{2}$$

where C_1 and C_2 are constants that depend on the thermocouple material. There is a common misconception that the potential difference is generated at the thermocouple junction; the potential difference is actually generated at the portions of the thermocouple wire that experience a temperature gradient. Because the different materials that make up the thermocouple have different Seebeck coefficients, the temperature gradient produces a different potential difference in each wire — the junction simply provides the electrical connection that allows the net voltage difference to be measured. In many applications, the temperature gradient is largest near the junction, so the distinction is minor. Table 3 lists the most common thermocouple types along with the temperature sensitivity of each [20].

Table 3   Types of thermocouple and their temperature sensitivity

Type	Composition	Sensitivity	Type	Composition	Sensitivity
K	Chromel-Alumel	41 µV/°C	R	Platinum 13% Rhodium-Platinum	8 µV/°C
E	Chromel-Constantan	68 µV/°C	S	Platinum 10% Rhodium-Platinum	7 µV/°C
J	Iron-Constantan	54 µV/°C	T	Copper-Constantan	43 µV/°C
N	Nicrosil-Nisil	30 µV/°C			

The transient response of the thermocouple depends primarily on two parameters: the size of the thermocouple and the degree of thermal contact between the thermocouple and the material of interest. A small thermocouple responds more quickly to temperature changes than a large thermocouple does. When measuring the temperature of a fluid, the convection coefficient determines the degree of thermal contact; when measuring the temperature of a solid, the contact resistance determines it. Thus a thermocouple in an

agitated fluid or in close thermal contact with a solid responds more quickly than one in a quiescent fluid or in loose thermal contact with a solid.

Boiling

Thermocouples have a long history of application in boiling research. In one early application, thermocouples are imbedded in the heater at various depths. Given a known heater material and monitoring the temperature at fixed points separated by a known distance, the heat flux delivered to the surface can be determined. This technique is often used to verify the electrical power supplied to the heater (as in Berenson [21] and Han and Griffith [22]). Similarly, given a known heat flux and the depth of the uppermost imbedded thermocouple, the surface temperature can be determined without having a sensor directly on the surface. This technique is still used, as in Son, et al. [23] and Héas, et al. [24]. This technique is limited to making steady state measurements, however, and can only provide a single surface temperature.

Other researchers have made single-temperature transient measurements. In their study of the high-heat flux nucleate boiling regime, Yu and Mesler [25] monitored a single, surface thermocouple using an oscilloscope, and were able to make transient measurements at between 1500 and 4000 Hz. Héas, et al. [24] studied the influence of a thick heater on the onset of boiling, and so made nominally transient measurements in order to distinguish pre- and post- event temperatures, but their temporal resolution was only approximately 1 Hz. Similarly, Qi, et al. [26] used a single Type E thermocouple to relate the temperature at nucleation to surface texture characteristics. In a later paper, Qi and Klausner [27] extended this approach using five thermocouples on specific

nucleation sites. In each case, the measurements must have had some transient character in order to associate a particular temperature with a specific event; because the intent was only to identify this temperature, the specific temporal resolution was unreported.

The earlier idea of using multiple thermocouples to determine both temperature and heat flux was developed further by Chen and Hsu [28], who developed a dedicated heat flux sensor. This sensor consisted of thermocouple wires flattened to a thickness of 25 μm and separated by mica sheets 5 μm thick. They used this sensor to study the initial and subsequent heat transfer between a superheated surface and liquid, such as would take place during transition boiling; monitoring the thermocouples with an oscilloscope, they were able to obtain transient data at between 32,000 and 800,000 Hz.

As researchers became interested in studying the local processes, they needed to measure the local temperature distribution over the surface as well. Liaw and Dhir [29] use sixteen 30-gauge Chromel-Alumel (Type K) thermocouples at four vertical locations (8, 26, 52, 77 mm) on a vertical-facing heater, with four thermocouples embedded at various depths within the surface at each vertical location. Wayner and Coccio [30] used a line of seventeen Iron-Constantan (Type J) thermocouples; within the most sensitive regions, these thermocouple were spaced at 0.1 ± 0.001 in. intervals — in less sensitive regions, they were spaced further apart.   Buchholz, et al. [31] used two sets of thermocouples. The first set consisted of eighteen sheathed, 0.25 mm diameter thermocouples of an unspecified type. Fourteen of these thermocouples were embedded 0.375 mm below the heater surface. The other four were embedded 6 mm below the surface; these four were used for heater control and to protect against burnout / over

temperature conditions. The second set was used to make more finely spatially resolved measurements; this set consisted of a 6 x 6 micro thermocouple array located in the center of the heater. These micro thermocouples were Copper-Constantan (Type T), with the Copper wire having a diameter of 50 μm and the Constantan wire having a diameter of 38 μm. These were spaced at 0.2 mm so that the resulting micro thermocouple grid covered a 1 x 1 mm^2 region. This array was also surrounded by another ring of eight Copper-Constantan thermocouples, these were made using 50 μm diameter Constantan thermocouple wire; these provide an additional group of fast-response thermocouples in conjunction with the micro thermocouple array.

Table 4 summarizes use of thermocouples in boiling research.

Table 4   Thermocouple applications in boiling research

No.	Researcher	Thermocouple Type / Configration	Spatial Resolution	Measurement Frequency
1	Berenson	2x axial locations (unspecified type)	Single surface temperature / heat flux	Steady state
2	Han and Griffith	3x axial locations (unspecified type)	Single surface temperature / heat flux	Steady state
3	Wayner and Coccio	17x surface array, Type J	2.54 mm or greater intervals	Steady state
4	Yu and Mesler	1x surface, Type K	Single surface temperature	1500 – 4000 Hz
5	Liaw and Dhir	16x surface and embedded, Type K	18 – 26 mm intervals	Steady state
6	Chen and Hsu	1x surface heat flux gauge (2x unspecified type thermocouple)	Single surface temperature / heat flux	32 – 800 kHz
7	Héas, et al.	2x axial locations, Type K	Single surface temperature / heat flux	1 Hz
8	Qi, et al.	1x Type E	Single surface temperature	Nucleation event only
9	Buchholz, et al.	18x unspecified type embedded in heater, 8x + 36x Type T micro thermocouple array on surface	0.2 mm, 1.2 mm spacing	25 kHz
10	Qi and Klausner	5x located at artificial cavities, unspecified type	1 per cavity	Nucleation event only

Jet Impingement

Thermocouples are also commonly used in jet impingement research. However, differences in research goals between jet impingement and boiling lead to differences in the way thermocouples are employed in the respective experiments. In particular, all of

the jet impingement studies discussed here were conducted at steady state. These studies

also place a greater emphasis on determining the surface temperature distribution.

There were two approaches used to obtain a surface temperature distribution: the

first approach used a thermocouple array. Vader, et al [32] uses a linear array of 17

thermocouples, spaced at 5.08 mm intervals and affixed to the surface using a spring

loaded mechanism. In a later paper by the same research group, Wolf, et al. [33] used 22

Chromel-Alumel thermocouples nominally spaced at 4.9 mm; in this paper, they welded

the thermocouples to the heater surface. Stevens and Webb [34] used 28 thermocouples

spaced at 2.5 mm intervals, and Womac, et al. [35], used seven Copper-Constantan

thermocouples on two radii from the point of impingement, at separations ranging from

1.08 mm to almost 3 mm.   Mohanty and Tawfek [36] used 17 temperature / heat flux

sensors made from three-wire Copper-Constantan thermocouples; these thermocouples

were arranged in a cross-shaped pattern, with the sensors on the x-axis spaced at 12.5 mm

intervals close to the point of impingement and widening to 20 mm at larger radii (on the

off-axis, the sensors were spaced at 20 to 35 mm intervals).

Another approach to obtaining the temperature distribution is by using a single

thermocouple and moving either the nozzle or sensor to obtain a series of measurements.

Sun, et al [37] used a single Iron-Constantan thermocouple affixed to the heater surface

and used a three-dimensional coordinate rack to move the nozzle/jet assembly; they were

able to position the nozzle with an uncertainty of 0.01 mm. Elison and Webb [38] used a

similar arrangement, keeping a single Type T thermocouple stationary on the heater while

using a three-axis positioning table to adjust the nozzle position; they reported a

positional uncertainty of 0.013 mm. Li and Garimella [39] used a fixed nozzle and

moved the heater and thermocouple beneath it. (Note that this approach requires that the

temperature distribution not change as the experimental setup changes. As a result, its

use is inherently limited to steady state testing; it cannot be applied to boiling research.)

Table 5 summarizes the use of thermocouples in jet impingement research.

Table 5   Thermocouple applications in jet impingement research

No.	Researcher	Thermocouple Type / Configuration	Spatial Resolution
1	Vader, et al.	17x linear array, unspecified type	5.08 mm intervals
2	Stevens and Webb	28x linear array, unspecified type	2.5 mm intervals
3	Mohanty and Tawfek	17x cross–shaped pattern, 3–wire copper–constantan (type T) temperature / heat flux gauges	12.5 – 35 mm spacing
4	Womac, et al.	7x on two radii, type T	1.08 – 3 mm intervals
5	Wolf, et al.	22x linear array, type K	4.9 mm intervals
6	Sun, et al.	1x type J on stationary heater, moving nozzle	Not specified
7	Elison and Webb	1x type T on stationary heater, moving nozzle	Not specified
8	Li and Garimella	1x type T on moving heater, stationary nozzle	Not specified

Resistance Temperature Sensors

Because the electrical resistance of a material varies with temperature, another type of sensor makes temperature measurements by measuring changes in electrical resistance. This type of sensor is called a Resistance Temperature Device (RTD). To a first approximation, the relationship between temperature and resistance is given by Eq. 3:

$$R = R_0\left(1 + \alpha_r \, \Delta T\right) \tag{3}$$

Resistance thermometers have an advantage over other temperature sensors in that they may serve as both thermometer and heat source simultaneously.

Boiling

RTDs are commonly used in boiling research. Perhaps because of the convenience of using resistance as the temperature-sensitive parameter of interest, some of the earliest boiling research used resistance thermometry. In his pioneering 1934 work identifying the phenomenon later known as "Critical Heat Flux", Nukiyama [40] determined the temperature of the heater by monitoring the heater resistance using a Wheatstone bridge. Lurie and Johnson [41] studied boiling from a thin ribbon of a iron-nickel material called "Deltamax" which was designed to have a large thermal coefficient of resistance, specifically for use as a combined heat-source / resistance thermometer. They monitored the voltage drop across the heater using an oscilloscope and a Polaroid camera, allowing them to make fast transient measurements. The specific measurement frequency is not specified, however they also took high speed photos at approximately

4200 frames per second. Today, the combined platinum wire heater / RTD is still in use; Kim, et al. [42] used a platinum wire to compare nucleate boiling heat transfer on different size heaters using both water and FC-72.

Researchers have also developed arrays of RTDs to measure local temperature variations. In their paper proposing the microlayer evaporation mechanism, Cooper and Lloyd [43] employed several thin-film resistance thermometers to monitor the temperature fluctuations in the vicinity of a bubble; a typical RTD arrangement used six linear elements with a spacing that varied from 0.5 – 1.5 mm; the inner four RTDs made temperature measurements while the outer two RTDs were used as heaters and triggered the bubble initiation. The temperature measurements were recorded using a high-speed recorder chart with a transient resolution of about 1 ms; some of their tests also incorporated a high-speed camera.

Recently, researchers have developed RTD arrays with many more individual sensor elements using micro fabrication techniques. Rule and Kim [44] developed an array consisting of 96 platinum RTD elements, approximately 0.26×0.26 mm^2 each, deposited in a 10×10 grid on a quartz substrate. Feedback controllers allowed these heaters to operate as constant temperature microheaters; the power delivered to each heater was measured, which provided a local heat flux distribution. Rule and Kim were able to acquire data at several rates: one data acquisition system collected data at 20 Hz, while a second system collected data at 2500 Hz per heater. Because the heater operated in a temperature-controlled mode — rather than the typical power-controlled mode — the risk of heater burnout at CHF was reduced. Kim's research group has continued to use

this heater (or subsequent designs in a similar family) to study a variety of boiling phenomena: Kim and Benton [45] and Kim, et al. [46] studied the effect of subcooling and gravity level, Henry and Kim [47] investigated Marangoni convection in microgravity, and Liu, et al. [48] examined the effect of a non-uniform electric field on bubble departure. Additionally, Myers, et al. [49] used the array without the feedback controllers to study the nucleate boiling in a constant heat flux mode. Other researchers using this type of sensor include Chen, et al. [50], who studied subcooled boiling incipience on a smooth surface. They collected heat flux data at more than 4000 Hz from a single microheater element on an array similar to Kim's; they also took high speed images at 2000 frames per second.   Moghaddam et al. [51] studied the nucleation process using a microheater array of a different design. Their array consisted of heaters located at 13 distinct radii from a central group of microfabricated, artificial nucleation sites. The spatial resolution of this array varied between 22 and 40 μm, and it achieved a sampling frequency of 8 kHz.

Other researchers have taken advantage of micro fabrication techniques to make still smaller individual heaters. Lin, et al. [52] investigated boiling on a single polycrystalline silicon (or polysilicon) 50×2 μm^2 microheater and on an irregular polysilicon microheater, also 50 μm long, but with a step change in width from 2 μm to 3 μm partway along its length; they do not report the measurement frequency. Tsai and Lin [53] studied transient bubble formation on similar polysilicon resistors 95×5 μm^2 and 95×10 μm^2. Although they do not report their data collection rate, several figures in the paper show a time scale on the order of 10 s, making high-speed data collection unlikely.

Jung, et al. [54] studied bubble nucleation on similar polysilicon resistors; they increased heater voltage in increments of 0.1 V every 10 s, and as they approached the nucleation temperature, they decreased the increment to 0.01 V. In a later paper, Jung and Kwak [55] used five of these polysilicon heaters to study boiling on a silicon chip in which the surface had been treated in two different ways. The sensors were spaced 5mm apart, and the researchers were interested in the steady state condition.

Table 6 summarizes the use of RTDs in boiling research.

Table 6   RTD applications in boiling research

No.	Researcher	Experimental Setup	Spatial Resolution	Measurement Frequency
1	Nukiyama	1x Platinum wire heater, (also Nichrome wire and Nickel wire)	Single Measurement	Steady State
2	Lurie and Johnson	1x Deltamax ribbon heater	Single measurement	4200 Hz
3	Cooper and Lloyd	5x Platinum microheaters	0.5, 1.5 mm	1000 Hz
4	Kim, et al.	1x Platinum wire heater	Single measurement	240 Hz
5	Rule and Kim, Kim and Benton, Kim, et al., etc.	96x Platinum microheater array at controlled temperature	0.270 mm, 0.100 mm	20 Hz, 250 Hz, 1kHz, 2.5 kHz,
6	Myers, et al.	96x Platinum microheater array	0.100 mm	1130 Hz
7	Chen, et al.	1x Platinum microheater	0.270 mm	Boiling incipience event
8	Moghaddam, et al.	13x Nickel microheater array	0.022 – 0.040 mm	8000 Hz
9	Lin, et al	1x polysilicon microheater 50 x 2 μm^2	Single measurement	Steady State
10	Tsai and Lin	1x polysilicon microheater	Single heater (95 x 5 μm^2 or 95 x 10 μm^2)	Unspecified (slow)
11	Jung, et al	1x polysilicon microheater	Single heater (50 x 5μm^2 or 50 x 10 μm^2)	Nucleation Event
12	Jung and Kwak	5x polysilicon microheater array	5 mm	Steady State

Jet Impingement

Interestingly, no jet impingement research using resistance measurements was found; the reason for this is not immediately obvious. One possible explanation is that the advantage of a combined heater / temperature sensor is more important in boiling experiments than in jet impingement experiments. In boiling, the length scale depends on the bubble size, which imposes a natural limit on the experiment size, keeping them small. In jet impingement, the length scale depends on the nozzle diameter, which can be selected by the researcher, allowing larger experiments.

Thermochromic Liquid Crystals

The third technique uses thermochromic liquid crystals (TCLCs) to obtain a detailed surface temperature distribution optically. TCLCs reflect different wavelengths of light at different temperatures [16]. These materials start out as colorless and change to red at a particular temperature. As the temperature increases, the material passes through the full rainbow of the spectrum to violet and becomes colorless again. The temperature of the initial change to red is known as the "red start," and the temperature range over which the material reflects a visible color is known as the "color play bandwidth" [56]. The temperature interval over which the reflected color remains the same is known as the "isochrome bandwidth" and may be as small as 0.1 °C [16].

Because the color change is visible to the eye, TCLCs can be used without requiring any special equipment. By knowing the red start temperature and the color play bandwidth, an observed color can be associated with an approximate temperature. The color changes can also be recorded photographically; because the temperature is related to

the color's hue component, the photo can be analyzed using image processing software to determine the temperature distribution. Depending on the image resolution, a detailed surface temperature distribution can be obtained over a large region.

TCLCs also have several disadvantages. First, because they are an optical method, the TCLC-coated surface must be visible during the test. For jet impingement, this can be accomplished relatively easily depending on the fluid used. For boiling, however, this is usually not possible, and the material must be applied to the back of the heater. In order to ensure that the measured temperatures accurately correspond to the local temperature distribution at the heater surface, the heater must be very thin and/or highly thermally conductive.

Unlike other temperature sensors, TCLCs are limited to narrow temperature bands. This limits the range of experimental parameters that can be tested using a particular TCLC formulation. Table 7 lists the red start and color play bandwidth for several commercially available TCLC formulations. The red start temperatures range from -30 to 120 °C, while the color play bandwidth is limited to 20 – 30 °C.

Table 7   Available TCLC formulations (from Childs [16])

Red-start temperature (°C)	Minimum color play bandwidth (°C)	Maximum color play bandwidth (°C)
-30	2	30
0	1	25
30	0.5	25
60	1	20
90	1	20
120	1	20

To illustrate the problem, consider a boiling experiment using FC-72. At 1 atm, the

saturation temperature of FC-72 is 56 °C. None of the TCLC formulations listed in Table

7 could be used in such an experiment. The test would have to be conducted at a lower

pressure, or another fluid would have to be selected.

TCLCs are also sensitive to chemical contamination and to damage from

ultraviolet radiation. To protect against these hazards, the TCLC material is often

encapsulated within a polymer coating; while this protects the TCLC material, the

encapsulation material slows the transient response. A study by Ireland and Jones [57]

indicated that a monolayer of TLC capsules showed a mean time delay of approximately

3 ms, which they attribute to "both a conduction as well as an intrinsic physical lag,"

although Kenning [58] cites other research showing that the response time for an

unencapsulated crystal is similar. A later paper by Ireland and Jones [59] discusses many

issues associated with using liquid crystals for temperature and heat flux measurements.

Anderson and Baughn [60] report a definite and significant hysteresis effect that can

introduce temperature biases of up to 1.2 °C for a broadband TLC; they suggest that

careful experimental design can minimize the experimental impact of this hysteresis.

Boiling

While not as common as thermocouples or RTDs, TCLCs are being used in

boiling research. Kenning[58] used TCLC thermography to visually estimate the local

superheat variations during pool boiling. In a later paper, Kenning and Yan [61]

conducted experiments using unencapsulated material on a stainless steel heater 0.13 mm

and measuring 28.1 × 40.8 mm^2; they photographed the temperature distribution at 200

frames per second, digitized the images at a resolution of 128 × 162 pixels

(corresponding to a spatial resolution of 0.22 × 0.25 mm^2 per pixel, if the whole heater

were digitized), and converted the color representation from RGB to HSI to determine the

temperature. McSharry, et al. [62] used data acquired at 200 fps using unencapsulated

TCLC material on a 0.125 mm thick stainless steel heater to compare two techniques for

identifying active nucleation sites from spatio-temporal temperature data sets. The heater

in their work measured 11.4 × 10 mm^2, and the experimental area was limited to a 64 x

64 pixel array measuring, which was further averaged during analysis to a 32 x 32 array

of temperatures. Chin, et al. [63] studied flow boiling using a 76 μm thick heater made of

Haynes 230 alloy, with the back face covered with encapsulated TLC material. They

recorded the color play using a video camera, which suggests a frame rate of 30 fps, and

digitized a strip 36 × 623 pixels, resulting in a resolution of 0.56 × 0.56 mm^2 / pixel.

Sodtke, et al. [64] used a high-resolution unencapsulated TLC test setup to study the wall

temperature distribution under a bubble in micro-gravity; using a long-working-distance

microscope, they limited the field of view to 800 × 600 μm^2 to achieve a resolution of

1.04 μm/pixel. In another study, Sodtke, et al. [65] used unencapsulated TLCs on a

stainless steel foil heater, and using a long-working-distance microscope, achieved a

resolution of 7.8 μm/pixel. They acquired images at 250 fps.

Table 8 summarizes the use of TCLCs in boiling research.

Table 8   TCLC applications in boiling research

No.	Researchers	Experimental Setup / Temperature Determination	Spatial Bandwidth, Resolution	Measurement Frequency
1	Kenning	Unencapsulated TLC, 0.13 mm thick stainless steel heater / Visual estimation	~ 1mm	0.1 Hz
2	Kenning and Yan	Unencapsulated TLC, 0.13 mm thick stainless steel heater / Image processing	128 x 162 pixel region, 0.22 x 0.25 mm^2 / pixel	200 Hz
3	McSharry, et al.	Stainless steel heater 0.125 mm thick / Image processing	32 x 32 pixel region, 0.36 x 0.31 mm^2 / pixel	200 Hz
4	Chin, et al.	Encapsulated TLC, 76 μm thick Haynes 230 Alloy foil heater / Image processing	36 x 623 pixel region, 0.56 x 0.56 mm^2 / pixel	30 Hz
5	Sodtke, et al.	Unencapsulated TLC, 10 μm thick stainless steel foil heater / Image processing	Unspecified pixel array, 7.8 x 7.8 μm^2 / pixel	250 Hz
6	Sodtke, et al.	Unencapsulated TLC, 10 μm thick stainless steel foil heater / Image processing	800 x 600 μm^2 heater region, 1.04 μm / pixel	Steady state / slow transient

Jet Impingement

Because TCLCs provide a surface temperature distribution over a large area, they

are also often used by jet impingement researchers. In addition, because most jet

impingement experiments are conducted at steady state, the transient response issues that

complicate their use do not apply to jet impingement research. Goldstein and Franchett

[66] studied heat transfer from a jet striking a surface at an angle; they used a

photographic filter to isolate specific isotherms and a polar grid on the surface to

determine the shape of the contours. Baughn and Shimzu [67] also estimated the

temperature contours by sight. Yan, et al. [68] used a similar experimental setup, but

used image capturing hardware and image processing software to identify the temperature

contours, although they do not provide the spatial resolution of their equipment.

Table 9 summarizes the use of TCLCs in jet impingement research.

Table 9   TCLC applications in jet impingement research

No.	Researcher	Method of determining temperature
1	Goldstein and Franchett	Photographic filter
2	Baughn and Shimzu	Visual estimation
3	Yan, et al	Image Processing

Diode Temperature Sensors

Although the operating principles governing diode thermometers are discussed in detail in the next chapter, a brief overview of their history and use is presented here.

The first documented use of a semiconductor diode as a thermometer appears to be in 1961. In a letter to Scientific American , Herbert Harris described an electronic circuit he had constructed "for indicating the temperature at our local hotel, and [I] am gratified by the results." [69] He also provided a graph indicating the temperature vs. voltage drop for
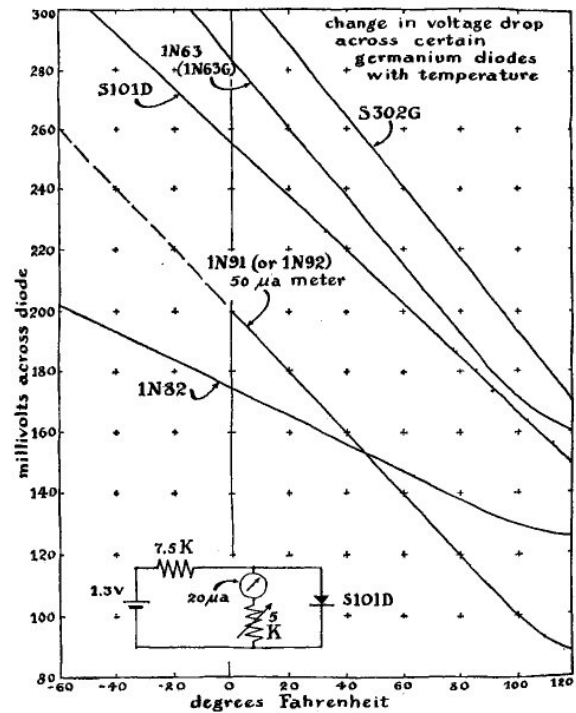
Figure 4   Harris's diode thermometer chart [69]

several commercially available diodes, shown in Figure 4. McNamara [70] developed the diode thermometer further, describing more rigorous tests of six types of commercially available silicon and germanium diodes (a total of 17 diodes), and finding that the sensitivity of the germanium diodes was 1.83 mV/°C, while the sensitivity of the silicon diodes was 2.11 mV/°C. He also found that the response was linear over a broad temperature range – a sensitivity of 2 mV/°C adequately represented the response from -40 to 100 °C, and he recommended that the sensing current be maintained below 1 to 2 mA to limit dissipation within the diode. Sclar and Pollock [71] discussed diode thermometer behavior for cryogenic temperatures as low as 4 K and developed a model explaining the diodes' sensitivity to temperature. A later paper by Shwarts, et al. [72] related the temperature response to the diode's design; they also presented a method for determining the maximum effective operating temperature for a given design. Treharne and Riley [73] used a diode as an analog to an RTD; they replaced the sensing resistor in a wheatstone bridge with a diode — they reported that this arrangement provided a linear 1 mV/°C sensitivity over the temperature range ± 200 °C.

To date, few researchers have used diode thermometers in either boiling or jet impingement research. In a study of liquid nitrogen jet impingement, Vader, et al. [74] used five diode thermometers, although they treated the diodes as RTDs and related the temperature to the resistance rather than to the voltage drop. In a study of thermal effusivity and CHF, Arik and Bar-Cohen [75], used both diode thermometers and thermocouples. Finally, in a spray cooling study, Pautsch and Shedd [76] used nine diode thermometers on their test die.

While the applications described above utilize the diode's temperature sensitivity, none take advantage of the feature for which diodes are best known – conducting current in only one direction. Kim, et al. [77] used this behavior to design a multiplexed diode array, but because of problems with the interconnects along the columns, they were only able address half of the bottom row, for a total of 16 diodes. Han and Kim [78] successfully developed a similar array using 32×32 diodes covering an 8×8 mm^2 region, as well as eight polysilicon heaters arranged in concentric rings. They also reported that each diode required approximately 1 ms to make a measurement; this suggests that they require approximately 1 s to scan the entire array, so their sensor operates at approximately 1 Hz.

It is worth noting that these two groups appear to represent the complete list of prior researchers who have pursued the multiplexed diode array approach.

Summary

This chapter presented an overview of the temperature measurement techniques commonly employed by boiling and jet impingement researchers. While researchers in both fields are interested in determining local temperature distributions, boiling researchers require high-resolution, transient measurements, while jet impingement researchers are concerned with steady state measurements over a larger region.

Thermocouples are commonly used temperature sensors in both fields. In boiling research, the most extensive technique uses a 6×6 micro thermocouple array covering 1 mm^2 and collects data at 25 kHz. Jet impingement research uses arrays with fewer thermocouples and larger spacings, but because the measurements are taken at steady

state, investigators can also use a technique in which a single thermocouple is moved relative to the jet nozzle.

While RTDs are commonly used in boiling research, they appear to be absent from jet impingement research. This may be a consequence of boiling's smaller characteristic length scale; the RTD's ability to combine heat source and temperature sensor is less advantageous for the larger length scales associated with jet impingement. In boiling research, the most extensive technique uses 10×10 microheater array covering 1 mm^2 and collects data at up to 2.5 kHz; a similar array collects data from fewer microheaters, but achieves a linear spacing of between 0.022 mm and 0.040 mm and collects data at 8 kHz.

Thermochromic Liquid Crystals are also frequently employed in both boiling and jet impingement research, though not as frequently as thermocouples or RTDs. TCLCs offer the ability to obtain very detailed temperature distributions by photographing the color play and using image processing software. Their use, however, imposes severe restrictions on the experimental design. They are also limited to narrow temperature ranges and have relatively long response times. A typical distribution obtained using TCLCs might be as large as 128×162 and have a spatial resolution of 0.22×0.25 mm^2/pixel and a measurement frequency of 200 Hz.

While diode thermometers are not currently in widespread use, they offer a potential solution to the logistical issues associated with developing large arrays of individual temperature sensors. These issues, and the solution offered by diode

thermometry, are the central focus of this dissertation and will be discussed in detail in the next chapter.

Chapter 3: Diode Array Design

Introduction

This chapter describes the diode array designs developed in the present work. It begins with a brief general discussion of semiconductor materials and diodes, followed by an overview of the multiplexed diode array concept. After discussing the details of the two designs, the chapter closes by describing the packaging of the completed array.

Semiconductors

Based on their electrical conductivity, materials are described as belonging to one of three categories: conductors, insulators, and semiconductors. Conductors have a high conductivity and easily permit an electrical current to flow, while insulators have a low conductivity and prevent current flow. Although semiconductors ordinarily have a low conductivity, the conductivity can be controlled through a process known as "doping," in which impurities ("dopants") are added in carefully controlled quantities.

Silicon is the most common semiconductor material, and common dopants include aluminum and phosphorous. Silicon is a Group IV element, and has four valence electrons. Aluminum is a Group III element, and phosphorous is a Group V element. In a silicon crystal, each of the silicon atom's four electrons is used to create a covalent bond with a neighboring silicon atom. When a silicon atom is replaced by a phosphorous atom, four of the phosphorous atom's electrons are used to bond to the neighboring silicon atoms. The fifth electron remains free, which increases the conductivity of the overall crystal. Because of this, phosphorous is referred to as a "donor impurity," and

silicon doped with a donor impurity is referred to as "n-type." By comparison, when a

silicon atom is replaced by an aluminum atom, the aluminum atom has only three

electrons available for bonds with the neighboring silicon atoms. The missing electron

forms a "hole", which also increases the conductivity of the overall crystal. For this

reason, aluminum is referred to as an "acceptor impurity," and silicon doped with an

acceptor impurity is referred to as "p-type."

The impurities do more than just change the conductivity, however. When the

two types of doped silicon are brought together, they form a "p-n junction," which has an

interesting property — it only permits current to flow in one direction. When a voltage is

applied across a p-n junction so that the p-type silicon is at a higher potential, the junction

is said to be "forward biased" and allows current to flow; this is illustrated in Figure 5a.

(a) Forward bias
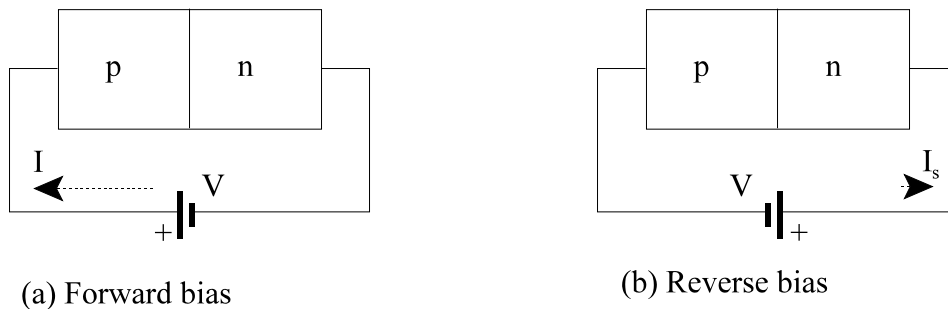
(b) Reverse bias

Figure 5   Forward and reverse biased p-n junctions

If the n-type silicon is at a higher potential, the junction is said to be "reverse biased" and

allows only a tiny current to flow. This current, known as the "saturation current," is so

small however, on the order of 10^{-15} A, that for practical purposes the junction can be said

to block current flow. The reverse biased condition is illustrated in Figure 5b.

Diodes

The simplest semiconductor circuit element is the diode, consisting of a single p-n junction. As would be expected from the properties of p-n junctions, diodes only permit current flow in one direction. Figure 6 depicts several common representations of diodes. Figures 6a and 6b shows the relationship between the p and n regions and the common

Figure 6   Diode representations

schematic diagram symbol shown in Figure 6b. Figures 6c and 6d show a side view and top view of how a diode is laid out in an integrated circuit.

Unlike a resistor, the diode's current-voltage relationship is not described by Ohm's law. Instead, there are two main models for this relationship. The first is the "perfect diode" model, shown as the dashed line in Figure 7. According to this model, no current at all flows in the reverse bias condition, and the diode displays a high resistance for low forward bias voltages condition. At some critical
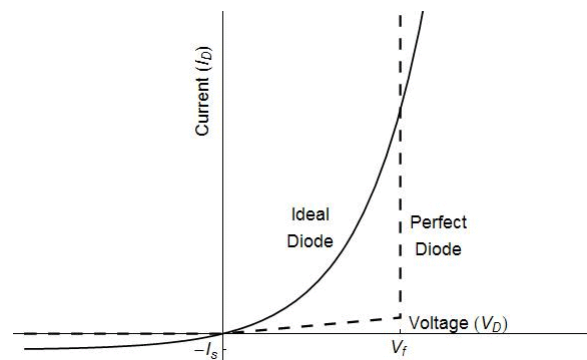
Figure 7   Diode V-I Curve

forward voltage V_f the behavior changes, and the diode conducts any amount of current without any further drop in voltage. This is a useful approximation for circuit design, but it is not very accurate.

The second model is the "ideal diode" model, shown in Figure 7 as the solid line. According to this model, the current increases exponentially with the applied voltage in the forward biased condition, and the saturation current I_s flows in the reverse biased condition. This is expressed mathematically as Eq. 4: [79]

$$I_D = I_S\left(\exp\left(\frac{V_D}{k\,T/q}\right) - 1\right)$$ (4)

The quantity ($k\,T/q$) is known as the thermal voltage, and represents the electrical potential of an electron due to its temperature.

There are several expressions for the saturation current. According to Massobrio and Antognetti [79] the saturation current depends on the dopant concentrations and the junction geometry according to Eq. 5.

$$I_s = q\,A_j\,n_i^2\left(\frac{D_p}{N_D\,L_p} + \frac{D_n}{N_A\,L_n}\right) = q\,A_j\,n_i^2\left(\frac{D_p}{N_D\,W_p{}'} + \frac{D_n}{N_A\,W_n{}'}\right)$$ (5)

Although Eq. 4 includes some small temperature dependence through the thermal voltage, the actual temperature sensitivity of a diode results from temperature sensitive terms in the saturation current equation. According to Blackburn [80], the saturation current can be represented by Eq. 6:

$$I_S = I_0\,T^\gamma\,\exp\left(\frac{-E_g}{k\,T}\right)$$ (6)

where I_0 collects the terms that are not sensitive to temperature, E_g is the bandgap for silicon ($E_g \approx 1.12$ eV at 275 K), and γ is a constant (approximately equal to 3).

Substituting Eq. 6 into Eq. 4 and taking the derivative with respect to T, Blackburn derives Eq. 7:

$$\left[\frac{\partial V_D}{\partial T}\right]_{I_D} = -\gamma\frac{k}{q} + \frac{\left(V_D - E_g/q\right)}{T} \tag{7}$$

which shows that the sensitivity is about 2 mV/K and varies by only 7% between 275 and 475 K. By comparison, Treharne and Riley [73] use Eq. 8:

$$I_S = K\,T^{5/2}\exp\!\left(\frac{-V_B q}{2kT}\right) \tag{8}$$

Here K is a "diode geometry constant" analogous to Blackburn's I_0 constant. Both Blackburn and Treharne and Riley treat the bandgap as a constant, while in reality it has its own temperature sensitivity. Shwarts, et al. [72] include this temperature dependence in their discussion of the temperature limits for diode thermometers. They develop a complicated expression for the temperature sensitivity as a function of temperature, in terms of the p-n junction design parameters which may be of use to any subsequent researchers.

Multiplexed Diode Array Concept

In the previous chapter, several types of electrical temperature transducers were discussed: thermocouples, RTDs, and diodes. Each of these is a two-lead device (there are sensor topologies that use more than two leads per sensor, but this only exacerbates the problem described below and will not be considered here), and using a large number of these sensors poses a serious logistical problem.

To illustrate this point, consider an array of RTDs, similar to that used by Kim's research group. Each resistor requires two leads; therefore a 3 x 3 array such as in Figure 8 requires 18 leads — two leads per sensor for nine sensors. Kim's 10×10 array requires 200 leads for the 100 microheaters. As the array grows larger the problem becomes progressively worse, growing as $2N^2$ for an $N \times N$ array. One solution to this growth would be to multiplex the sensors in order to share leads, but attempting to do this for an array of RTDs produces the circuit shown in Figure 9. Although this circuit requires only six leads, it fails to work at all.
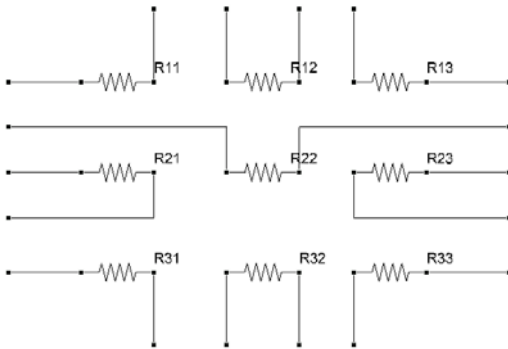
Figure 8   3 x 3 Microheater array, normal
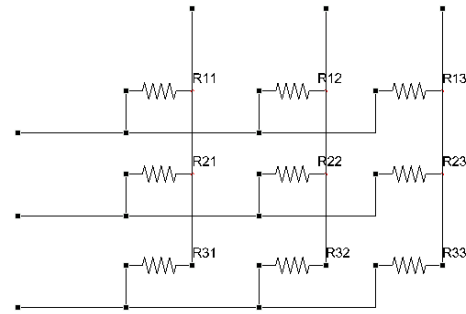
Figure 9   3 x 3 Microheater array, multiplexed

The multiplexing solution fails for an RTD array because resistors permit current to flow in both directions. That is, regardless of which terminal of the resistor has the higher potential, the resistance remains the same. Diodes, on the other hand, only permit current to flow in one direction; for them the multiplexing solution succeeds.

Consider the 3×3 array of diodes multiplexed in the same way as the resistors in Figure 9, as shown in Figure 10. The diodes are connected such that the anodes for all of

the diodes in a given row are connected in parallel, while the cathodes for all of the

diodes in a given column are connected in parallel.

By manipulating the voltage and ground connections for the columns and rows, any arbitrary diode can be individually selected to be forward biased. Since only this diode conducts a current and experiences a voltage drop, it is also referred to as the "active" diode. First, consider the configuration shown in Figure 11. Applying +5 V to row B while grounding rows A and C
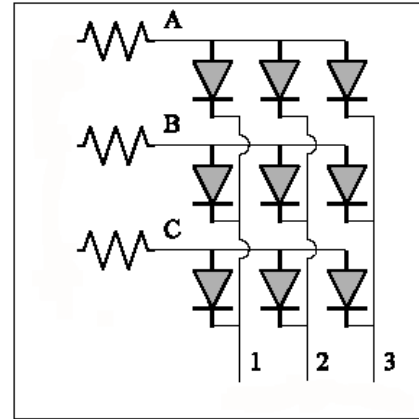
Figure 10   Diode array concept design

selects row B, while grounding column 2 and applying +5 V to columns 1 and 3 selects

column 2. Thus only diode B2 is active, and its voltage drop can be measured at point B.
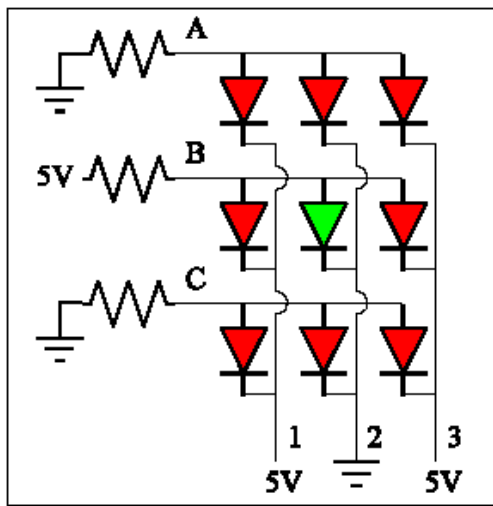
Figure 11   Diode array, single diode active
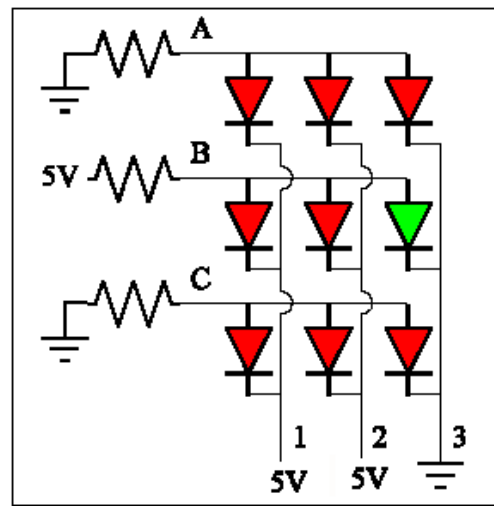
Figure 12   Diode array, next diode in scan

Of the remaining diodes, A1, A3, B1, B3, C1, and C3 are reverse biased, while diodes

48

A2 and C2 are only neutrally biased, because both anode and cathode are grounded. By applying +5 V to column 2 and grounding column 3, B3 becomes the active diode, as shown in Figure 12. The same type of reasoning can be applied to activate a diode in another row; simply ground row B and apply 5 V to row A or C. Each diode in the array can be scanned in this way; because each diode is activated individually, this approach is referred to as "diode-wise scanning."

Although the entire array can be scanned by activating each diode individually, activating groups of diodes simultaneously offers a substantial increase in speed. Consider the configuration shown in Figure 13. Diodes A1, B1, and C1 are active, and the remaining diodes are reverse biased (inactive). The voltages at points A, B, and C are solely determined by diodes A1, B1, and C1 respectively — voltage drops across diodes in other rows have no effect on the voltage measured in any particular row. Therefore nothing is lost by activating the entire column at once. The voltages at A, B, and C can be measured to scan the first column; applying +5 V at the first column and grounding the
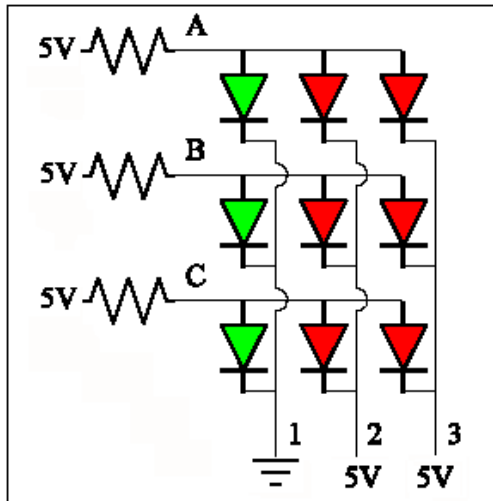
Figure 13   Diode array, single column active   Figure 14   Diode array, next column active
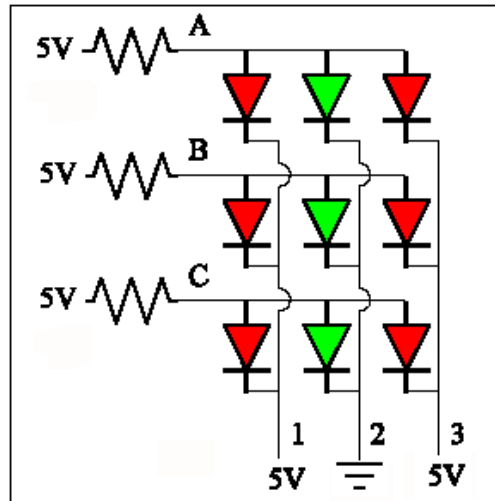
49

second (as shown in Figure 14) activates the second column. The voltages at A, B, and C are measured to scan the second column, and the process is be repeated until the entire array has been scanned; because entire columns are activated simultaneously, this approach is referred to as "column-wise scanning."

The target scanning frequency covered the entire 32×32 array used in the present work at 1 kHz. Using diode-wise scanning (Figures 11 and 12), achieving this would require two switching circuits — one circuit operating at 1024 kHz (1.024 MHz) to select a single row, and a second circuit operating at 32 kHz to select a single column. Using column-wise scanning (Figures 13 and 14), the rows are kept at +5 V continuously, and a single switching circuit operating at 32 kHz switching circuit is needed to select a single column. The present work adopted column-wise scanning; further analysis of the ramification of this choice are discussed in detail in subsequent chapters.

Multiplexed Diode Array Designs

There were two generations of diode array designs used over the course of this project. Both designs incorporated a 32×32 diode array, and both designs incorporated polysilicon resistive heater elements. Also, because of concerns that the surface would be too smooth to provide adequate nucleation sites, each design left one diode position empty; if it were necessary to create an artificial nucleation site, the empty position would be used to avoid damaging the row and column interconnects.

The earlier design was submitted for fabrication as "SingleHeater," and will be referred to hereafter as the Model I design. The Model I design successfully demonstrated the feasibility of the diode array concept, but were several areas in which

the performance could be improved. First, the on-chip traces connecting the columns were undersized for the current they carried, resulting in appreciable voltage drops in the connecting leads along the columns . The heaters were also undersized; although the 54 W/cm^2 heat flux seemed adequate in the design phase, the power delivered to the fluid was reduced by conduction losses through the substrate. Finally, the diode design left a narrow strip of intrinsic (undoped) silicon between the p- and – regions in the p-n junction, forming a p-i-n junction instead. A better design would omit that strip.

The later design addresses these issues. It was submitted for fabrication as "LowRdiodes," and will be referred to hereafter as the Model II design.

Table 10 summarizes the design parameters for both the Model I and Model II designs. The p-n junction dimensions were not optimized; they were based on geometric concerns. At the time the Model I design was being developed, an alternate design was also being developed; this alternate design used diodes on 50 μm centers, so that the overall array would be only 1.6 × 1.6 mm^2. The intent had been to use the same p-n junction design for both diode arrays. Using dimensions of 33.6 × 38.6 μm^2 fit within the constraints of the smaller design and so were also used for the Model I design.

The Model II design took a different approach. Because the primary goal was to reduce the parasitic resistance, the p-n junction design was designed to reduce the resistance associated with the metal-silicon contacts as much as practical. Each such point of contact was associated with 40 – 60 Ω; using a 6 × 6 array of such contacts would reduce this resistance by a factor of 36, while still allowing the column and row leads to be made much wider. Thus, the p-n junction was set at 27.2 × 49.6 μm^2.

51

Table 10   Summary of Model I and Model II design parameters

Design parameter	Model I parameter value	Model II parameter value
p-n junction dimensions	$33.6 \times 38.6 \ \mu m^2$	$27.2 \times 49.6 \ \mu m^2$
Anode (row) connection	Metal2, 4.8 μm wide	Metal1, 43.2 μm wide
Cathode (column)	Metal1, 4.8 μm wide	Metal2, 64.0 μm wide
Heater geometry	2x poly2 serpentines 61.6×3500 μm, connected in parallel and covering $800 \times 800 \ \mu m^2$	4x poly2 strips 56×3700 μm, connected in parallel and covering $400 \times 3700 \ \mu m^2$
Heater arrangement	4×4 grid (16 total)	1×8 array (8 total)
Heater resistance	1200 Ω per serpentine; 600 Ω total	1360 Ω per strip; 340 Ω total
Current limit	24 mA	200 mA
Voltage limit	14.4 V	68 V (22 V)
Maximum power dissipation	0.346 W per heater; 5.54 W total.	13.6 W per heater; 108 W total (1.42 W per heater; 11.4 W total)
Maximum heat flux	54 W/cm^2	919 W/cm^2 (100 W/cm^2)
Total number of leads required	96 total; 32 rows, 32 columns, 2×16 heaters	80 total; 32 rows, 32 columns, 2×8 heaters
Empty diode position	(17,16)	(13,13)

Figures 15 – 18 depict the major elements of the Model I design. Figure 15 shows the Model I base diode cell as designed, while Figure 16 shows a single heater element; the 8×8 diode sub-array can be seen between the heater elements. Figure 17 shows the overall ASIC (Application Specific Integrated Circuit) design, and Figure 18 shows the actual diode array, as fabricated.
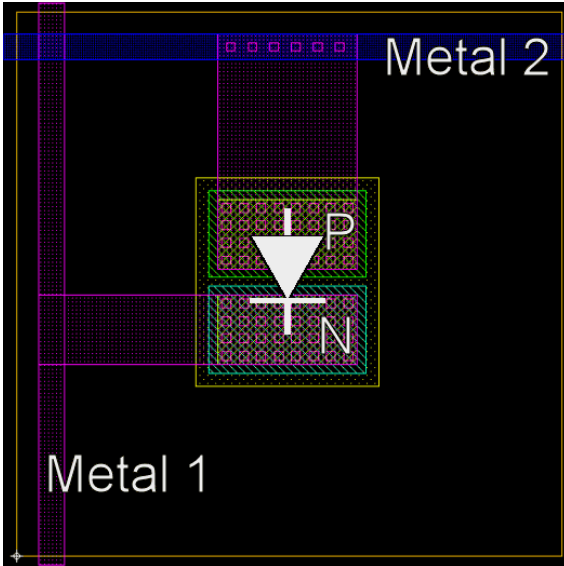
Figure 15 Model I diode cell
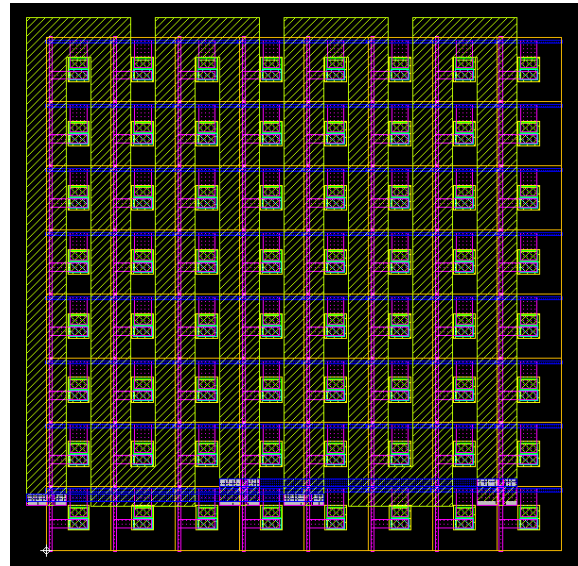
Figure 16 Model I heater cell
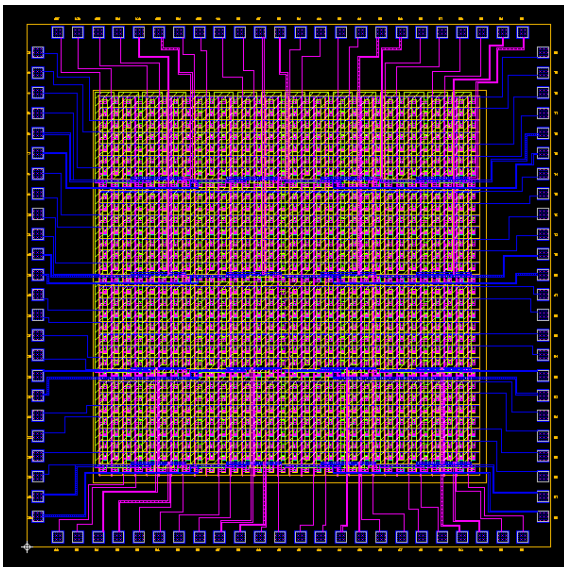
Figure 17 Model I ASIC cell
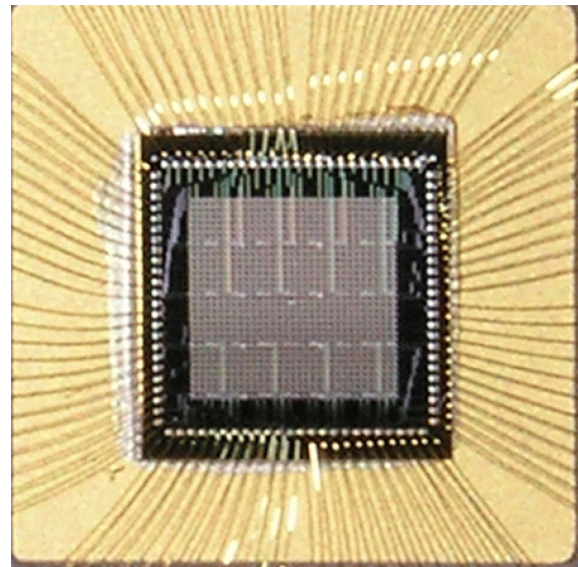
Figure 18 Model I as fabricated
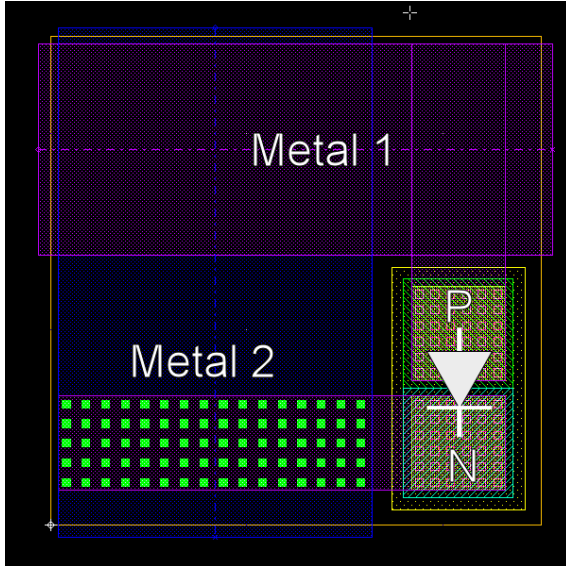
Figure 19   Model II diode (design)
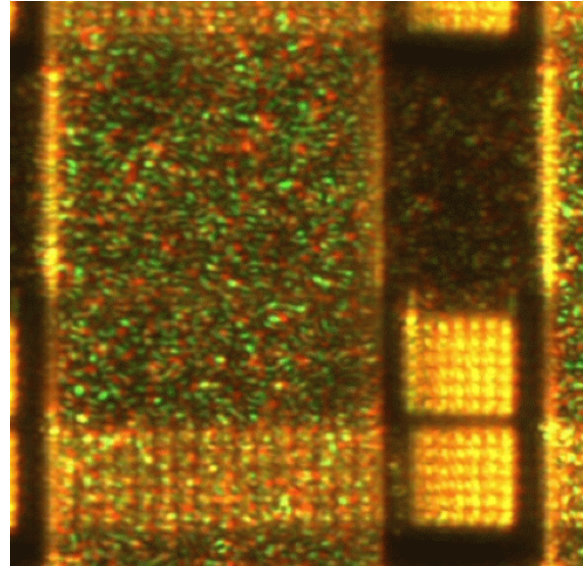
Figure 20   Model II diode (fabricated)

Similarly, Figures 19 – 23 depict the major elements of the Model II design. Figure 19 shows the revised diode design, with the metal layers exchanged and widened significantly. Figure 20 shows a single diode cell as fabricated. Figure 21 shows the revised heater design; because of the extreme aspect ratio (approximately 38:1), the design details are difficult to discern, so frames a and b show magnified views of the top and bottom of the heater,
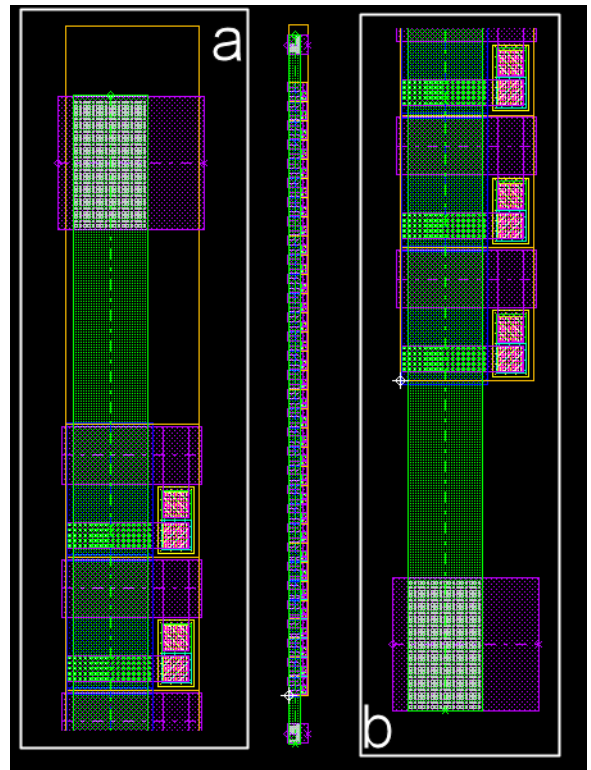
Figure 21   Model II heater design

respectively. Figure 22 shows the overall ASIC design, while Figure 23 shows the final ASIC as fabricated.
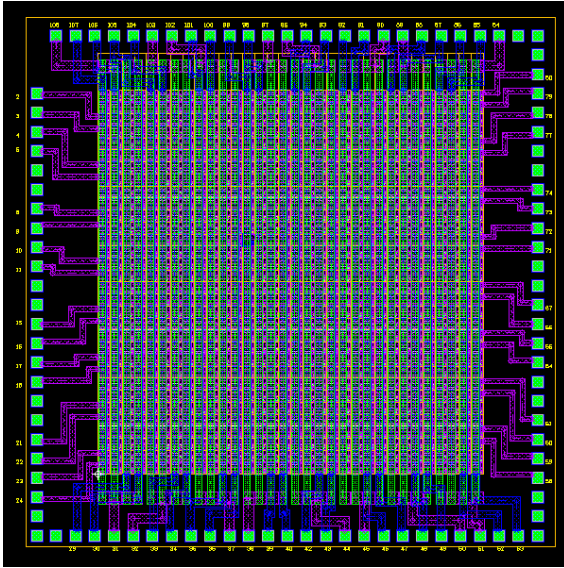
Figure 22   Model II ASIC design   Figure 23   Model II ASIC (fabricated)
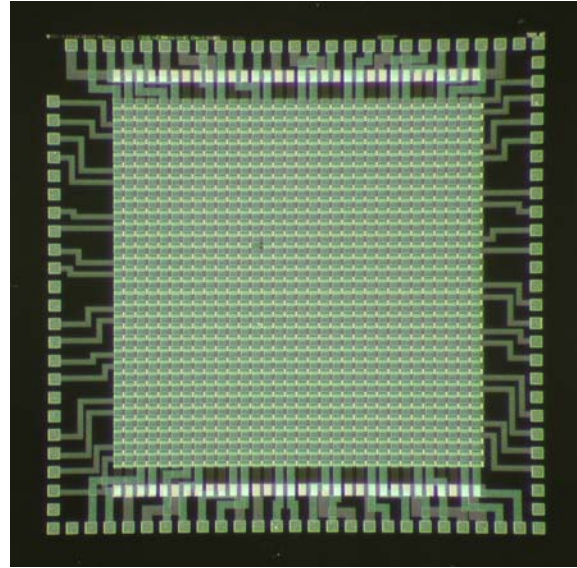
The diode array designs were developed using a freely available IC layout software package called LAyout System for Individuals (LASI). In LASI, shapes drawn on different layers correspond to openings in the various photolithography masks used during the fabrication process. LASI also enforced a hierarchical design methodology, in which the complete design was built up from simpler components called "cells." Each cell was assigned a rank, and could be reused in cells of higher rank [81].

The completed designs were submitted to the MOSIS service (Metal Oxide Semiconductor Implementation Service) for fabrication. Integrated circuit fabrication is a complicated, expensive process — MOSIS offers students and researchers the opportunity to have Application Specific Integrated Circuit (ASIC) designs fabricated at greatly reduced costs. According to the MOSIS website, "MOSIS keeps the cost of

fabricating prototype quantities low by aggregating multiple designs onto one mask set. This allows customers to share overhead costs associated with mask making, wafer fabrication, and assembly." [82]

Using MOSIS, the designs were fabricated by AMI Semiconductor using their 1.5 micron ABN process. This is an n-well process, with two metal layers and two polycrystalline silicon layers [83].

Packaging

The packaging of the two designs differed as well. For the Model I design, all five chips were packaged by MOSIS as part of their fabrication service. Each die was packaged in a Kyocera PGA108M package; this is a ceramic pin grid array with 108 pins and a 350 mil central cavity. The Model II design was packaged in the same ceramic PGA, but with several changes. First, the silicon die was thermally insulated from the package using a 5.5 mil thick layer of kapton tape in order to reduce substrate conduction. Also,
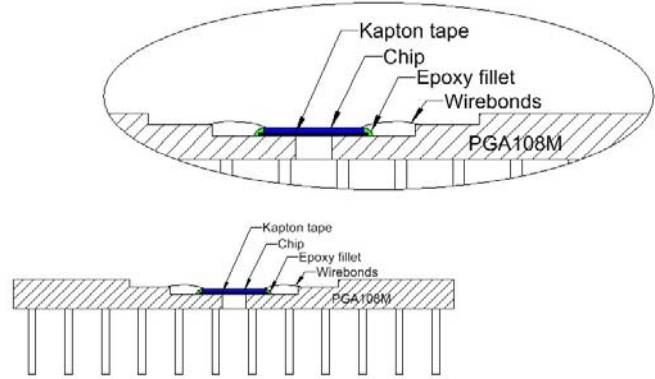
Figure 24   Revised packaging technique for Model II design

Figure 25   Model II design as packaged

a small hole ($\sim$2 mm^2) was drilled in the back of the chip to allow the pressure on both

sides of the chip to equalize, reducing the likelihood of the kapton tape delaminating. A

schematic of the revised packaging is shown in Figure 24, and Figure 25 shows a photo of

the final package.

Because of the special requirements, the Model II designs were not packaged by

MOSIS. Instead, MOSIS delivered the completed chips unpackaged. An initial lot of

three chips were sent to Aspen Technologies for packaging; later, the remaining two chips

were also packaged by Aspen Technologies. Both sets of chips were packaged as

described above — the only difference was that the first lot was connected using

aluminum wire bonds, while the second lot was packaged using gold wire bonds.

Chapter 4: Data Acquisition

This chapter describes the data acquisition system. This includes the specialized circuit board used to control the array, as well as several additional circuit boards necessary for the characterization testing and the data acquisition hardware and software.

Interface board

The interface board handles all of the tasks necessary to make use of the diode array sensor. There are six such functions:

1. Heater control

2. Instrumentation power supply

3. Row voltage supply

4. Column switching

5. Signal conditioning

6. Interface to data acquisition system

The subcircuits necessary to accomplish these tasks are each described in the sections that follow. The board itself, shown in Figure 26, is a four-layer PCB, including one dedicated ground plane.
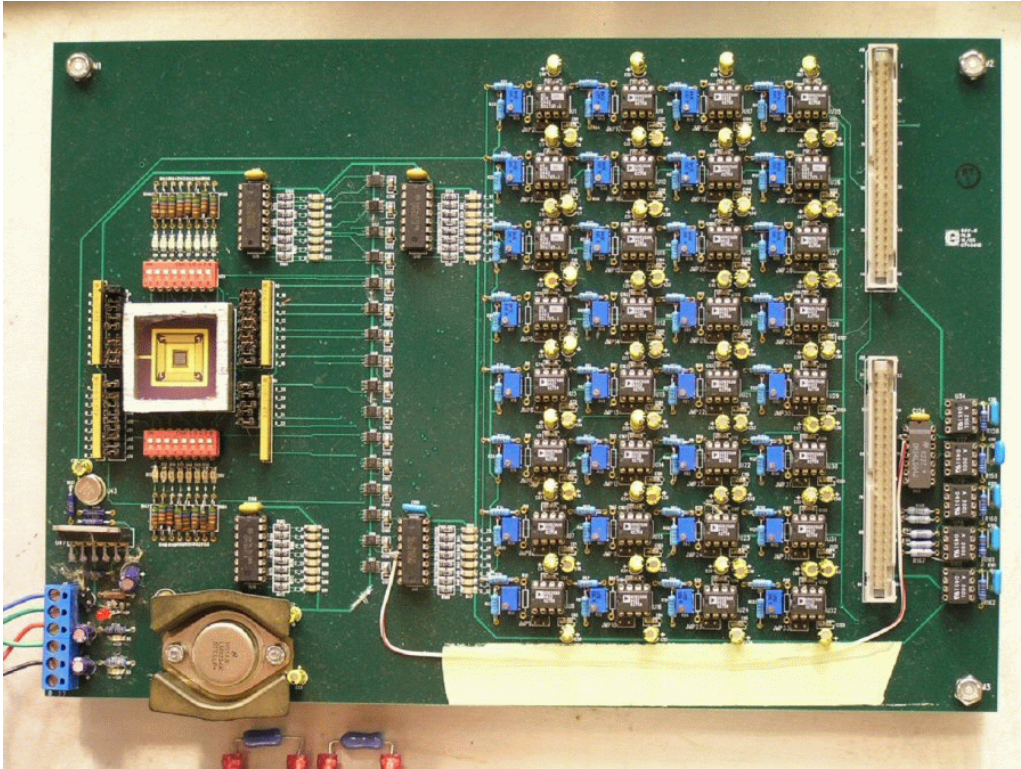
Figure 26   Interface board

Heater Control

The heater control circuit is responsible for controlling which heaters are active and for minimizing the decrease in power dissipation associated with self-heating. It does not control the actual power delivered by the heater; the heater is supplied by a Sorenson LH 35-10 DC power supply, and the heater dissipation is controlled by adjusting this power supply directly. The circuit itself is very simple, consisting of only a set of on-off switches, a set of stabilizing resistors, and a set of indicator LEDs. The schematic is shown in Figure 27, while Figure 28 shows the circuit as implemented on the interface board. Two 8-bit DIP switches were used to activate the heaters individually, corresponding to the 16 heaters in the Model II design; after the Model III design came

into use, the lower bank of switches was made obsolete. Slightly outboard from the

switches, a bank of indicator LEDs can be seen, and still further outboard from these, the

stabilizing resistors are seen. As indicated in Figure 27, all of the active heaters are

supplied by a single voltage source in parallel.
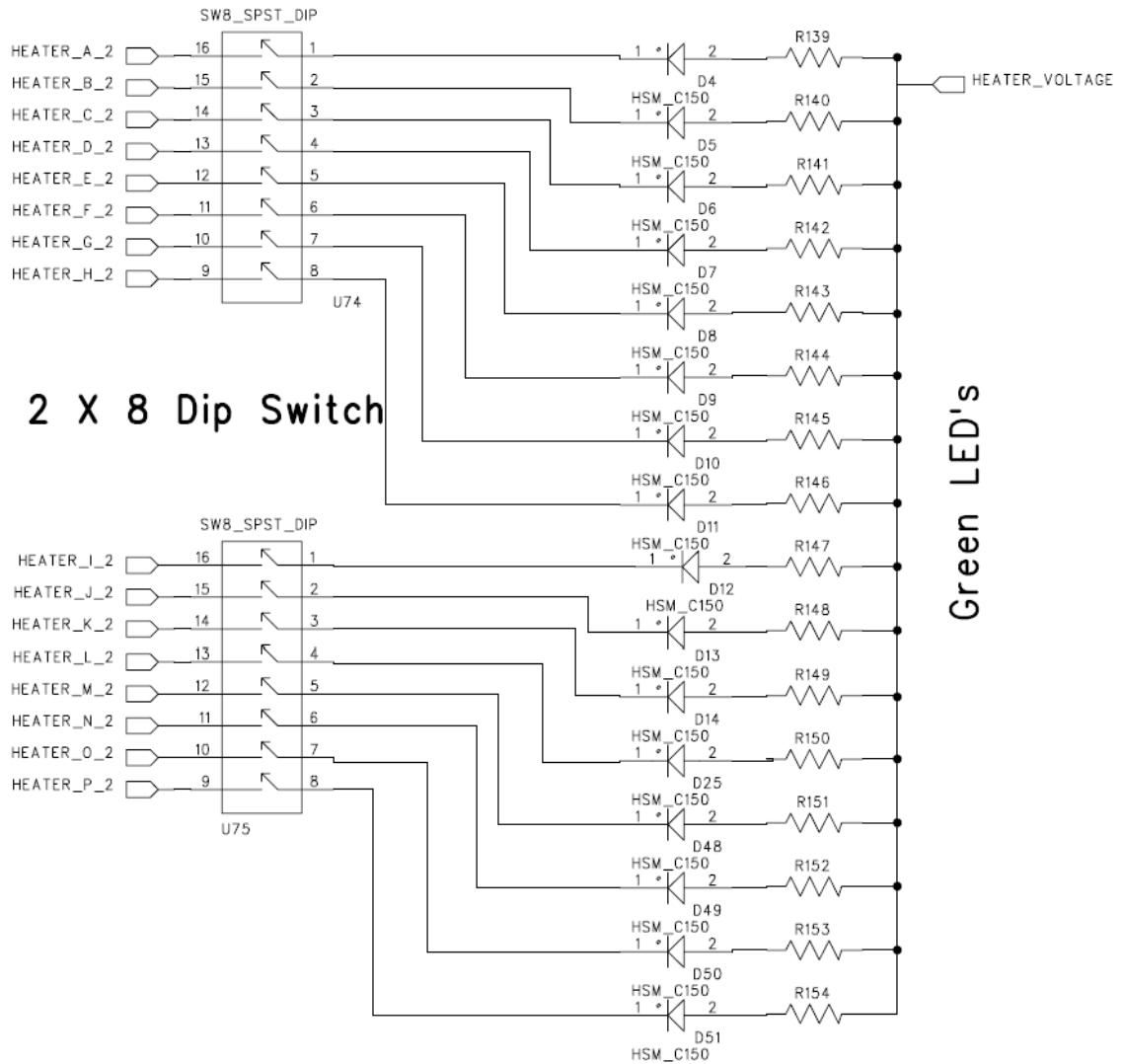
Figure 27   Heater control circuit (Courtesy of Jack Touart)

The stabilization resistors compensate for temperature-induced changes in the

heater resistance to ensure that the heaters dissipate a constant power, regardless of the

temperature of the diode array itself. For a resistive heater by itself (without such a stabilizing resistor), the effect of temperature on the delivered power is given by Eq. 9:

$$\frac{Q(\Delta T)}{Q(T_0)} = \frac{1}{1 + \alpha_R \Delta T} \tag{9}$$

Using the value of α_R for polysilicon suggested by Tsai and Lin [53], 1.2×10^{-3} / K, a change in temperature of 25 °C causes a 3% reduction in the delivered power. Although this is not a tremendous change, including a stabilization resistor is easily accomplished and substantially reinforces the constant heat flux assumption.
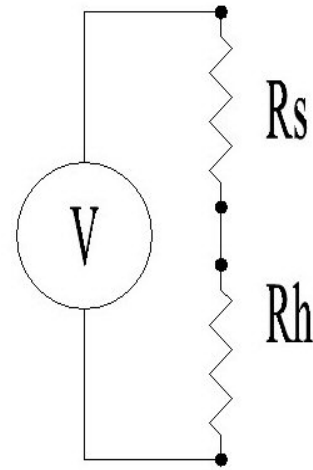
Figure 28　　Heater stabilization circuit

The stabilization resistor forms a voltage divider, as shown in Figure 28　The effect of temperature on the power delivered is now given by Eq. 10:

$$\frac{Q(\Delta T)}{Q(T_0)} = \frac{(R_H + R_S)^2 (1 + \alpha_R \Delta T)}{(R_S + R_H(1 + \alpha_R \Delta T))^2} \tag{10}$$

Again taking $\alpha_R = 1.2 \times 10^{-3}$/K, and choosing $R_S = R_H$ (it can be shown that the sensitivity to ΔT is minimized for this choice), then the same 25 °C temperature difference causes only a 0.021 % decrease in power dissipation. The constant power assumption is therefore much stronger by including the stabilization resistor.

61

Instrumentation Power Supply

  The instrumentation power supply circuits regulate the voltage available to the remaining circuit elements on the interface board. The interface board receives +18 V and -18 V from an HP 3631A DC power supply. These voltages are supplied directly to the AD620 instrumentation amplifiers in the signal conditioning circuit, described in detail in a later section. In addition, the +18 V supply is connected to an LM323A 3-Amp, 5-Volt Positive Regulator. This produces the +5 V supply for the rows. Figure 29 shows the schematic of the circuit.
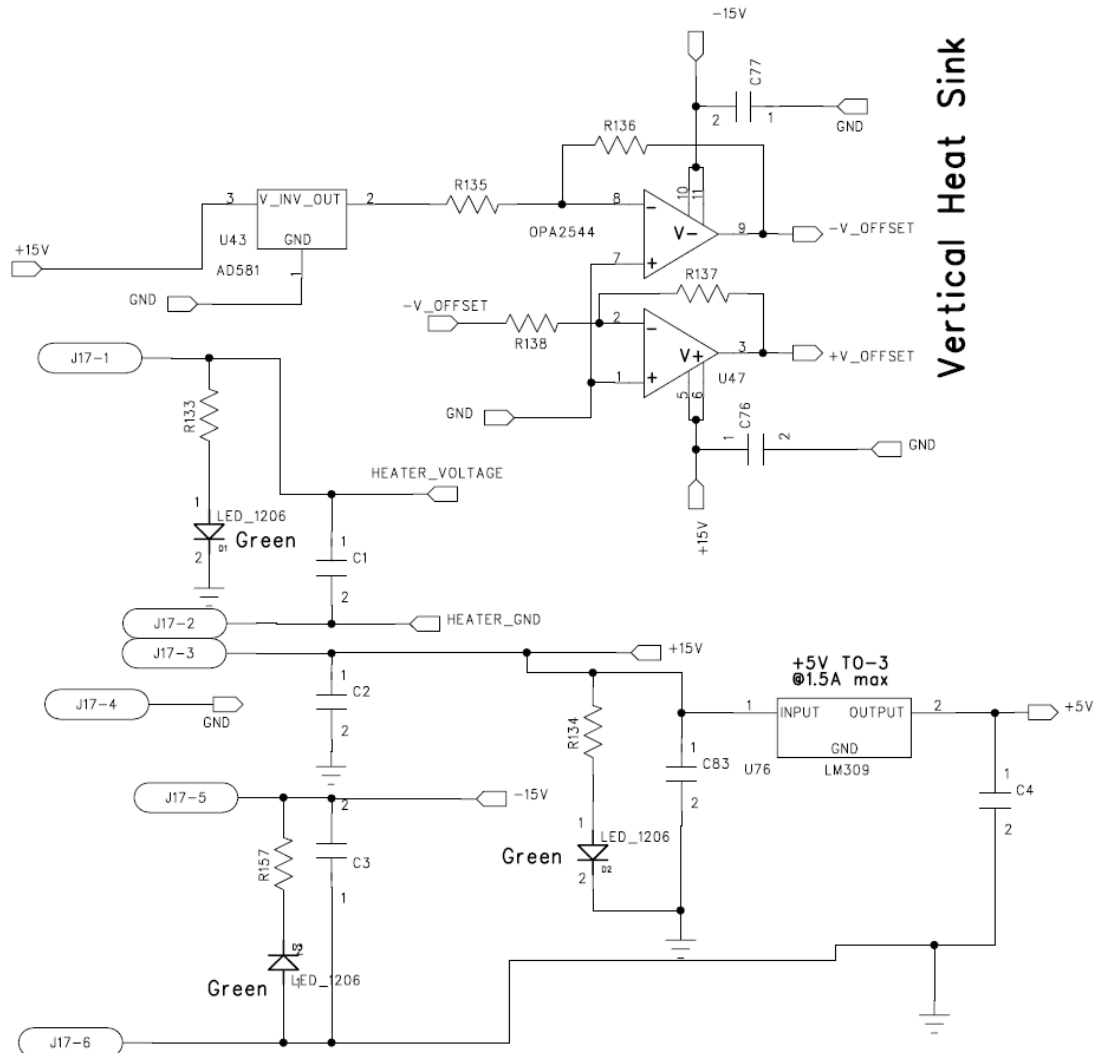
Figure 29   Instrumentation power supply schematic (Courtesy of Jack Touart)

Row Voltage Supply

The row voltage supply circuit is responsible for powering each of the diode array rows. It is connected to the +5 V output from the power supply circuit, and uses four 10-pin bussed SIP resistors to supply the current limiting resistors for each row. Each SIP resistor contains nine individual resistors, supplied by a common voltage. Each row is associated with one of these individual resistors. Several different values for these resistors were considered during the project, but the data reported here all use 47 kΩ resistors, producing a sensing current between 89.3 and 92.6 μA, depending on the voltage drop across the diode. Each row also includes a jumper block, which serves two functions. The set of active rows can be controlled by removing selected jumpers, or the sensing current for a particular row can be measured directly by connecting an ammeter across the jumper pins. Figure 30 shows the schematic for the row voltage supply.
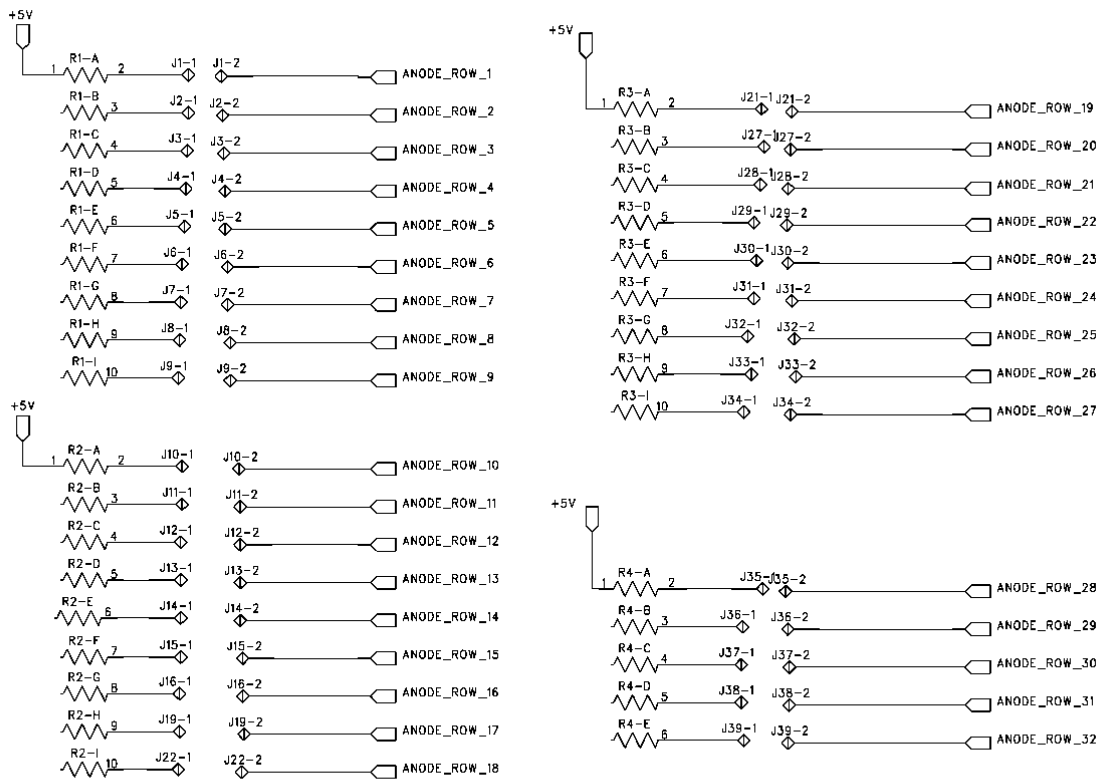
Figure 30   Row voltage schematic (Courtesy of Jack Touart)

Column Switching

The column switching circuit is the most complicated on the interface board. Its task is to produce a 5-bit address identifying which column should be active, decode this information into a 32-bit address, and connect that column to the electrical ground while connecting all other columns to a +5 V supply. Accomplishing these tasks requires three dedicated subcircuits – a 12-bit binary counter, a 32-bit demultiplexer, and 32 SPDT switches.

The 12-bit counter is responsible for producing the 5-bit address identifying the active column. An HP 33120A function generator provides the counter circuit with a 0 – 5 V square wave at 204.8 kHz, or double the desired sampling rate. The LSB (2^0 binary digit) of the counter acts as a divide-by-2 counter for all practical purposes and is used to drive the pacing of the data acquisition boards. The binary digits associated with the 2^6 – 2^{10} positions are then used to supply the 5-bit column address. By driving both the row and column data collection rates from a single counter, the relative phase is assured to be constant, and diode position associated with each data point can easily be determined in post-processing.

Given the 5-bit column address, the next step is to identify the specific column associated with that address. To accomplish this, a 1-of-32 demultiplexing circuit is used. This subcircuit is composed of four 74LS138 decoders and a 74LS04 inverter. Each LS138 decoder has eight output lines; thus the whole circuit has 32 output lines. The one selected line is at a low (ground) state, while the 31 remaining lines are at a high (+5 V) state. In an earlier version of the interface board design, this circuit controlled the columns directly; each column was connected to one of the demultiplexer output lines. This approach worked, but the resistance associated with the LS138 encoders introduced a significant voltage drop at the base of the active column.

This problem was resolved by introducing an AD836 switch at the base of each column. The AD836 is an analog SPDT switch; one position is connected to the ground plane, while the other is connected to the +5 V supply. The position of the switch is controlled by a signal pin; if this pin is high, the switch connects to the +5 V supply,

while if it is low, the switch connects to the ground. This signal pin is connected to the output of the demultiplexer circuit. Although this arrangement mirrors that of the previous design, the on-resistance of the AD836 is only 0.8 Ω, so there is virtually no voltage drop experienced at the column base. Figures 32 and 31 show the schematics for the SPDT switch and demultiplexing circuit, respectively.
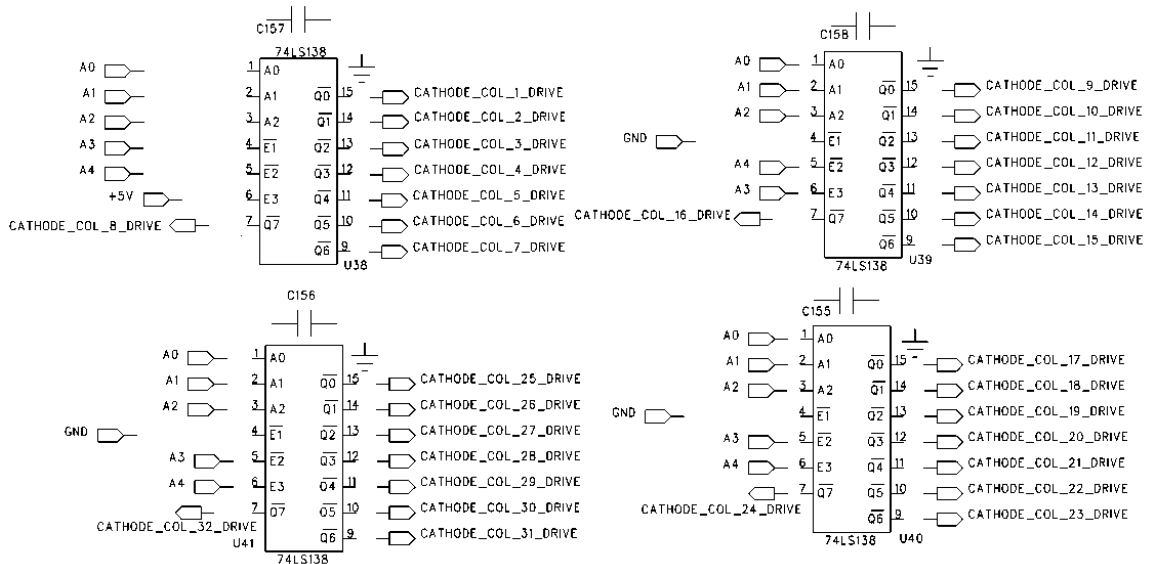
Figure 31   Demultiplexer circuit schematic (Courtesy of Jack Touart)
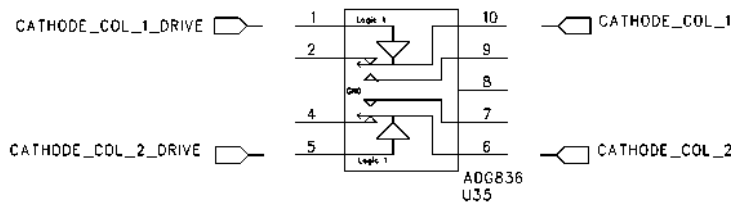
Figure 32   SPDT switch at column base (Courtesy of Jack Touart)

Signal Conditioning

Although not as complicated as the column switching circuit, the signal conditioning circuit is at least as important, if not more so. As discussed previously, at room temperature, the forward voltage drop across a diode is nominally 700 mV, decreasing by about 2 mV with each 1 °C increase in temperature. Because the intention is to measure the temperature distribution over the surface, the signal of interest will be a fluctuation on the order of a few mV, on a DC carrier signal of approximately 700 mV; reading this signal directly is not practical. The signal conditioning circuit simplifies this problem by first subtracting the diode voltage from a known DC component and then amplifying the resulting difference. Using an amplification factor of 100, the diodes' -2 mV / °C sensitivity becomes +200 mV/°C.

The accomplish this, a simple circuit was designed using an instrumentation amplifier. The AD620 is an instrumentation amplifier with an inverting and a non-inverting input, and the gain is easily set using a single resistor. For the signal conditioning circuit, the diode voltage is applied to the inverting input, and an arbitrary DC offset voltage is applied to the non-inverting input. The gain is related to the selection resistance according to Eq. 11:

$$R_g = \frac{49.4\,k\Omega}{G-1} \tag{11}$$

For this application, the desired gain $G = 100$, so the associated resistance $R_g = 499\ \Omega$. The measured voltage, then, is given by Eq. 12:

$$V_m = G\left(V_{DC} - V_D\right) \tag{12}$$

Each row has a separate signal conditioning circuit.

Over the course of this project, several techniques were used to supply the DC offset. The earliest of these used a separate voltage divider and screw potentiometer for each row. This proved impractical; changing each row individually was time consuming, and it was difficult to adjust the screw pot with sufficient accuracy and repeatability. Additionally, the setting had a tendency to drift with time. The second approach used the analog output from one of the data acquisition cards to set the voltage. The screw pots were removed, and the DC offsets for all 32 rows were connected in parallel to the analog output. Because this value could be easily and repeatably adjusted via software, this was an extremely effective system.

There were two primary drawbacks to this approach, both of which related to the accuracy of the delivered voltage. The first concerned the uncertainty in the voltage setting. At the smallest D/A output range, $0 - 10$ V, the uncertainty in the output was still approximately ± 3.5 mV; because this corresponds to nearly 2 °C, it posed a significant issue. However, this issue was resolved with the realization that what was important was the actual value of the voltage, rather than how closely it corresponded with the set point. Further, it turns out that the actual value needs to be known quite accurately for a different reason. The uncertainty associated with the data acquisition system will be in the neighborhood of ± 2 mV, but because this uncertainty is applied to the amplified difference between the diode voltage and the DC offset, it reflects an actual uncertainty of only about ± 10 μV. Consequently, the DC offset must be known to a comparable accuracy. This was accomplished by measuring the offset independently using an HP

69

34401A 6 ½ digit Multimeter; the uncertainty associated with the 1 V range is approximately ±20 μV, certainly within the target range.

The second drawback to using the analog output did not present itself until very late in the project and related to the interaction between the output voltage and the AD620 when driven outside its normal operational range. Like other op amp devices, during normal operation, the 620 has a large input impedance and draws no current at its inputs. If it is driven into saturation, however, this is no longer the case, and it can begin to affect its inputs. This is exactly what happened when the diode array was operated with non-functional column. All 32 of the 620s were simultaneously saturated, and because the non-inverting input of each was connected to the analog output on the data acquisition board, the aggregate effect perturbed the output beyond its ability to maintain a stable voltage. During the time the non-functional column was active, the voltage delivered by the D/A temporarily increased from its set point of 800 mV to as much as 1.400 V — a 600 mV difference and difficult to neglect.

The effect of this perturbation on the diode array measurements themselves was fairly minor. Once the non-functional column became inactive, the 620 would recover from saturation in a few hundred μs, the analog output would quickly stabilize after that, and while the measurements of the next column – and perhaps even the following column as well – might be invalid, the diodes in the remaining 30 columns could be taken normally. Unfortunately, the effect on the diode measurements themselves was not the only effect to consider.

The secondary effect of this voltage pulse affected the 34401A as well. The meter employs a time-averaging approach for noise reduction, and the averaging circuits within the meter simply averaged the pulse in as part of the DC signal. This artificially inflated the measured voltage slightly and changed the uncertainty from a few μV to several mV – clearly an unacceptable level. The obvious solution to this problem was to use a more robust power supply. The HP 3631A power supply was better able to tolerate the temporary loading while the 620s were saturated – the voltage pulse was generally less than 5 mV, but it was not as well regulated as the D/A had been. The voltage signal from the 3631 supply had considerably more noise at the mV level and below than did the D/A; this was not going to satisfy the necessary accuracy requirements.

The solution here was to simply extend the same principles already being applied. The ability to accurately control the offset voltage was less important than the ability to measure its instantaneous value, and the use of the AD620 circuit to measure sub-mV voltage fluctuations. A second AD620 circuit was constructed, this time taking the DC offset at the non-inverting input and some reference DC level, supplied by the D/A and monitored using the 34401 multimeter. For this circuit, the basic relationship would be expressed by Eq. 13:

$$\Delta V_{DC} = G_{offset}\left(V_{DC} - V_{D/A}\right) \qquad \textbf{(13)}$$

This equation is easily rearranged into the more useful form of Eq. 14:

$$V_{DC} = V_{D/A} + \frac{\Delta V_{DC}}{G_{offset}} \qquad \textbf{(14)}$$

which will be revisited in Chapter 6 during the full-array calibration discussion.

Data Acquisition

The final function performed by the interface board is the interface to the data acquisition system. As originally designed, this function was by far the simplest of six functions. Even later, after several revisions, the final version of the data acquisition interface is no more complicated than the heater control circuit.

The output from each row's signal conditioning circuit is carried to the appropriate data acquisition channel. Initially, the two boards were connected using a 100-pin connector to two 50-pin flat, unshielded ribbon cables, 2 m long. This allowed tremendous flexibility in the experimental setup, but the ribbon cables were vulnerable to cross-talk and other EMI noise. Rather than redesign the interface board, two short (20 cm) lengths of flat cable, with ferrite chokes, were used to connect the interface board to a shielded breakout box, which were connected to the data acquisition board via a 1 m shielded cable.

Additional Interface Boards

There were three additional interface boards produced during the course of this project. The first functioned as an extension cord, allowing the diode array to be separated from the interface board. The second allowed specific individual diode to be selected individually, and was used for the individual diode calibration and parasitic resistance tests. The third allowed two diodes in the same row to be selected.

Data Acquisition Hardware

The data collection was handled by two Measurement Computing PCI cards — a PCI-DAS6071 and a PCI-DAS6070. Both were 12-bit A/D boards capable of collecting

data at a maximum rate of 1.25 MS/s. The 6071 had 64 single-ended channels (or 32 differential channels) that measured the row voltages; because it measured the diode array, the 6071 was referred to as the main board. The 6070 had 16 single-ended channels (or eight differential channels) that measured the DC offset fluctuations and various other support sensors such as the thermocouple reader and flow meter; the 6070 was referred to as the auxiliary board.

These boards also had several additional features that were used in the present work. These included two channels of 12 bit D/A, eight digital I/O ports, and two on-board 8254 counters. They were also capable of being controlled and synchronized by an external timer. The cards were installed in a Dell Optiplex GX280 desktop PC, with 2 GB of RAM and a 3.4 GHz Pentium IV processor, running Windows XP Professional, SP2.

A schematic of the overall data acquisition setup is shown in Figure 33.
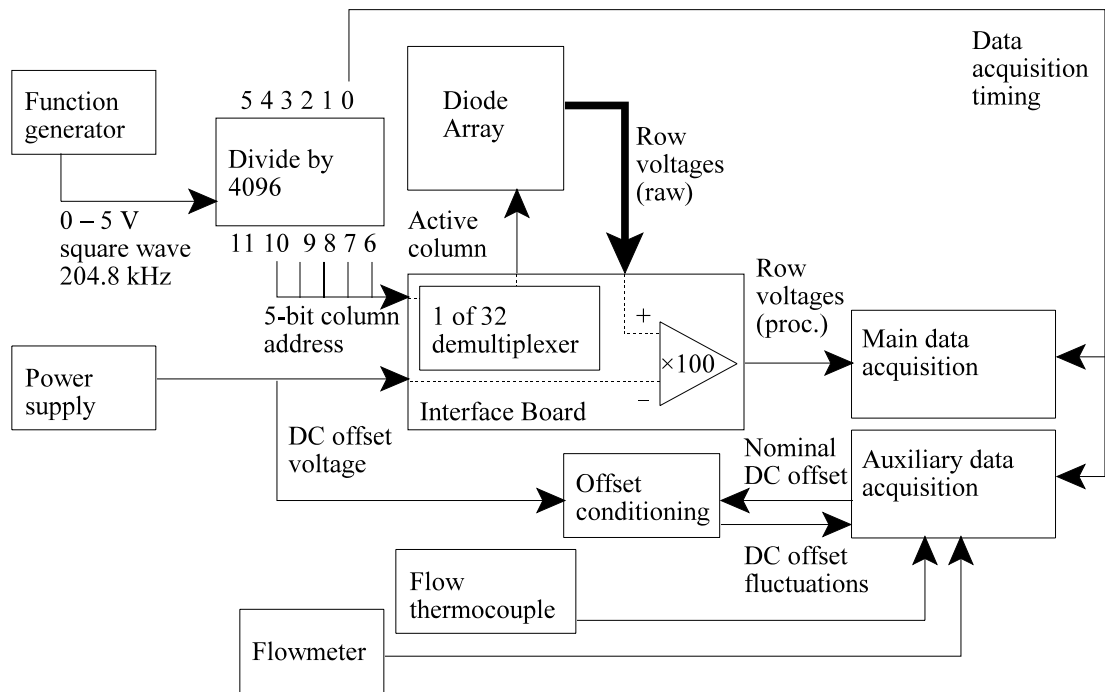
Figure 33   Overall data acquisition hardware schematic

Diode Array Failure modes

One potential issue with the diode array is the relative fragility of the packaging. Although the multiplexing scheme greatly reduces the number of leads required for a given number of sensors, it also greatly intensifies the impact on the system should one of the shared leads fail. There are two categories of lead failure — open circuits and short circuits.

Open circuit failure

An open circuit failure can result from the loss of one of wirebonds or from damage to the chip itself that severs one of the row or column connection paths. Although the loss of one or more of the wirebonds was by far the most common type of

74

failure, the effect would be very much the same for a failure in the leads on the chip itself. Also, the diode that was omitted from the design (at location (17,16) in the Model I design and (13,13) in the Model II design) introduces this sort of failure by design. Without the diode, no connection exists between the anode and cathode connection — effectively replicating this type of damage.

The specific consequences of an open-circuit failure depends on whether the failure was in a row or column connection.

If a row connection fails open, then none of the diodes downstream of the break will experience any current flow (for a wirebond failure, the entire row is affected). Because no current flows, the voltage all along the row will remain at the 5 V level. This will severely affect the signal conditioning circuit; at the instrumentation amplifier, the inverting input will be at +5 V, while the non-inverting input will be at the DC offset voltage — about 0.7 V. Applying the gain of 100 to the resulting -4.3 V differential produces an output of -430 V, in theory. In reality, the output is limited to the ± 18 V supply. The result is a condition known as "saturation" in which the usual assumptions of op-amp behavior are violated. While saturated, the amplifier output will be equal to the supply voltage — in this case, -18 V, regardless of the voltage at the inputs. The assumption of infinite input impedance is also violated, and the amplifier may begin to load the circuit, or may even begin acting as a source at the inputs.

The -18 V output also has a similar bad effect on the A/D converter used by the 6071. The maximum working voltage for the converter is ± 11 V, so the -18 V level will push it to saturation as well. Finally, both the amplifier and the A/D converter require

some time to recover after the input return to its normal range; thus the effects may persist long enough to affect subsequent measurements.

If a column connection fails open, the effect is very much the same, but on a larger scale. In the event of a column failure, current flow is prevented for all of the rows "upstream" of the failure flow (if the wirebond fails, this includes the entire column). As in the row failure, without any current flow, the entire row stays at the +5 V level, and the instrumentation amplifier saturates. For the column failure, this means that many amplifiers are affected, and the aggregate load imposed by so many saturated amplifiers may affect the DC offset voltage supply. This will be discussed further in a subsequent chapter.

Short Circuit Failure

The second type of major failure observed was a short circuit between the row and column leads on the chip itself. In the Model I design, the small width of the on-chip column and row leads made such a failure unlikely. With the increased width of the Model II design, this type of failure became possible and was observed in two chips.

While a shorted column is active, the effect of the short circuit is minor. This is the situation depicted in Figure 34, in which row B and column 1 are shorted together, and column 1 is active. The diode at B1 is bypassed by the short circuit, so that the voltage at B is simply 0 V (corresponding to the direct connection to ground). The net voltage differential to the amplifier will be the raw DC offset, which will drive the amplifier and A/D to saturation — this time at the positive +18 V rail; for this situation, the impact is no greater than for an open circuit.

76

When the shorted column is inactive, however, the effect is much worse. This is the situation in Figure 35. With the diode at B2 operating normally, the voltage at the short circuit is nominally 0.7 V; less than the voltage applied at the base of the column, so current flows to the short. This current can only return to the ground through the diode at B2. Because there is no current limiting resistor in on the column, the diode will continue to draw more and more current.
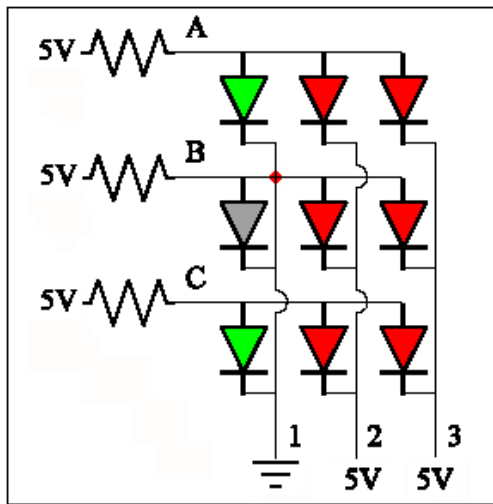
Figure 34   Short circuit failure, active   Figure 35   Short circuit failure, inactive
                 column   column
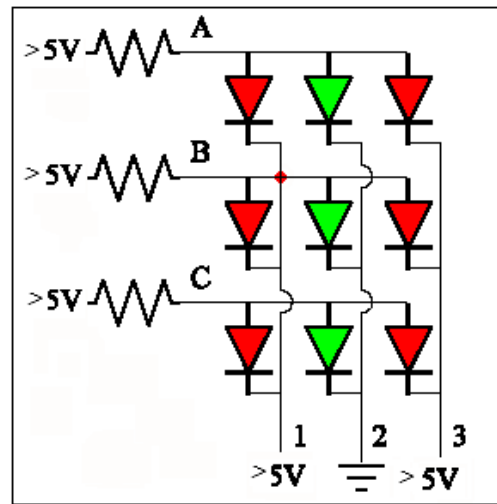
The current draw will become so large that the parasitic resistance will actually serve as the current limiting resistance. This will not happen until the current is on the order of several amperes. The power supply circuit is unable to supply this much current, resulting in a kind of brown-out, so that neither the rows nor columns are actually at the +5 V level. There is also a danger of components burning out as a result of the heat generated by such a large current.

Fortunately, this sort of failure can be remedied. An open-circuit failure can be introduced at the affected column by clipping the pin at the package level and isolating

the column. While this is only trading one kind of failure for another, with a open-circuit

column failure the chip can still be used, albeit in a limited capacity. By comparison,

with a short circuit failure, the chip is completely non-functional and the chip and

interface board are both at risk of further damage.

Data Acquisition

The data acquisition software was custom written in C++, using the Microsoft

Foundation Classes (MFC) to facilitate developing the GUI, and Measurement

Computing's Universal Library (UL) to handle the data acquisition itself. The DAQ

application itself is dialog driven, and allows the user to control the 6070 and 6071

boards.

Chapter 5: Numerical Analysis

Measuring the surface temperature is only part of the problem. Although the applied heat flux is known, not all of that power is delivered to the fluid. Because the chip is not well insulated within the package, a fraction of the power delivered will be lost by conduction into the substrate, through the packaging materials, and ultimately to the environment. Determining the heat flux lost to the substrate requires solving a 3-D conduction problem with the measured temperature distribution as a boundary condition.

3-D Conduction Solver

A custom 3-D, transient conduction solver was written using C++. Although in the end, the diode array was only used to make measurements of steady state phenomena, the initial goal had been to make measurements of transient phenomena. As such, the code was written to solve the transient problem, rather than the steady state problem. In practice this poses no problems; the code simply uses a large time step and proceeds until a steady state solution is achieved. While there is a penalty in computation time using this approach, this penalty is small and does not significantly affect the analysis.

The solver was implemented fairly simply. The domain is limited to only the silicon die itself, which simplifies the governing equation set, because only a single material need be considered, and the geometry, because only a rectangular parallelepiped need be considered. The geometry is further simplified by assuming a constant step size for the grid. Because the diode array measurements were intended to supply the boundary conditions at the top surface, it was important that the grid elements match the diode

array dimensions. This placed a constraint on the allowable step size. The diode

dimension — 0.1 mm — should be an integer multiple of the x and y step sizes. Thus a

value of 0.1 mm or 0.05 mm for Δx and Δy would be acceptable, while a value of 0.08

mm would be awkward for subsequent calculations. This constraint, in turn, limits the

number of elements in each direction, because the chip was measured to be 5.1 x 5.3

mm^2. The smallest allowable mesh in the x-y plane, therefore, was 52 x 54,

corresponding to $\Delta x = \Delta y = 0.1$ mm. However, because this restriction is the result of

having to match the locations of the mesh nodes with the locations of the diode array

measurements on the top surface, the z-direction was free of this sort of constraint; in this

direction an 11 node grid was used, corresponding to $\Delta z = 0.025$. A summary of the

spatial discretization is given in Table 11, and a depiction of the overall mesh is shown in

Figure 36, with a zoomed-in view provided in Figure 37. In these figures, the red dot

indicates the node location, and the lines indicate the element boundaries, so that the

nodes are located in the center of each element.

Table 11   Summary of spatial discretization

Spatial coordinate axis	Nodal coordinate axis	Spatial dimension	Number of discretized steps	Step size
x	n	L = 5.1 mm	N = 52	$\Delta x = 0.1$ mm
y	m	H = 5.3 mm	M = 54	$\Delta y = 0.1$ mm
z	p	D = 0.25 mm	P = 11	$\Delta z = 0.025$ mm
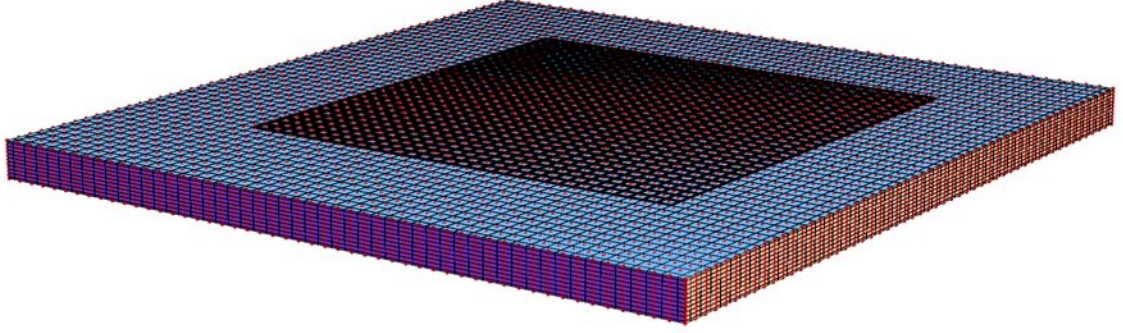
Figure 36   3-D conduction solver mesh

With the domain suitably discretized, the next step was formulating the system of equations. The partial differential form of the heat equation is given in Eq. 15:
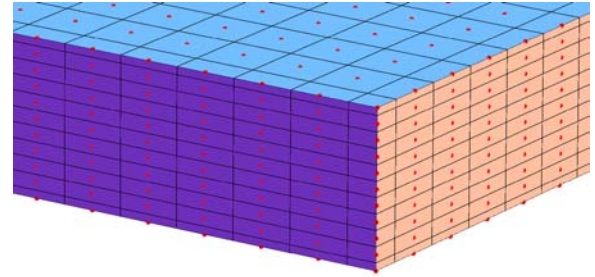
Figure 37   Chip corner (zoomed)

$$\frac{\partial T}{\partial t} = \frac{k}{\rho c} \nabla^2 T \tag{15}$$

Applying this equation to a single element produces the discretized form of the heat equation, Eq. 16:

$$\frac{1}{\alpha} \frac{T_{m,n,p}^{k+1} - T_{m,n,p}^{k}}{\Delta t} = \frac{1}{2} \left(\frac{T_{m+1,n,p}^{k+1} - 2 T_{m,n,p}^{k+1} + T_{m-1,n,p}^{k+1}}{\Delta y^2} \right) + \frac{1}{2} \left(\frac{T_{m+1,n,p}^{k} - 2 T_{m,n,p}^{k} + T_{m-1,n,p}^{k}}{\Delta y^2} \right)$$

$$+ \frac{1}{2} \left(\frac{T_{m,n+1,p}^{k+1} - 2 T_{m,n,p}^{k+1} + T_{m,n-1,p}^{k+1}}{\Delta x^2} \right) + \frac{1}{2} \left(\frac{T_{m,n+1,p}^{k} - 2 T_{m,n,p}^{k} + T_{m,n-1,p}^{k}}{\Delta y^2} \right) \tag{16}$$

$$+ \frac{1}{2} \left(\frac{T_{m,n,p+1}^{k+1} - 2 T_{m,n,p}^{k+1} + T_{m,n,p-1}^{k+1}}{\Delta z^2} \right) + \frac{1}{2} \left(\frac{T_{m,n,p+1}^{k} - 2 T_{m,n,p}^{k} + T_{m,n,p-1}^{k}}{\Delta z^2} \right)$$

When this equation is recast in matrix form by collecting the coefficients of the unknown

temperatures $\vec{T}^{k+1}$ to form a matrix [A] and combining the known temperatures $\vec{T}^{k}$ to

form a vector $\vec{B}$ (which acts as a kind of "forcing function"), it takes the form of Eq. 17:

$$[A]\vec{T}^{k+1} = \vec{B}(\vec{T}^{k})$$ **(17)**

The solution can then be found by inverting [A]. This is a simple procedure for the 1-D

heat equation, because for one dimension, [A] takes the form of a tri-diagonal matrix, for

which the tri-diagonal matrix algorithm provides a simple and efficient method for

inversion. Unfortunately, no such algorithm is available for the higher dimensional cases.

In the present work, a technique known as "operator splitting" is used to simplify

the calculations. This is an iterative technique in which the discretized heat equation is

reorganized as a set of coupled 1-D problems; it is closely related to the Alternating

Direction Implicit (ADI) methods[84] and is similar to the Gauss-Seidel method of lines

approach . Instead of advancing by a full time step, the solution advances by several

partial time steps, considering each coordinate direction in turn as a fractional time step.

Although the original ADI method was developed for solving 2-D problems (in which

each of the two directions is considered as 1/2 of a time step), Tannehill, et al. [84]

describe an approach for extending the ADI method to solve 3-D problems in which each

of the three coordinate directions is considered as a 1/3 time step. This sort of approach

was used by Wang, et al. [85] to develop a chip-level 3-D transient thermal simulator.

The ADI approach is implemented as follows: for each coordinate direction, the

equations for the elements along one line in that direction are collected. Temperatures

that fall on this line are treated as unknown, while the temperatures at the surrounding elements are treated as known. Figure 38 illustrates this for a line in the x-direction. The red cubes represent the elements of interest, while the blue cubes represent the adjacent elements in the y-direction, and the green cubes represent the adjacent elements in the z-direction.
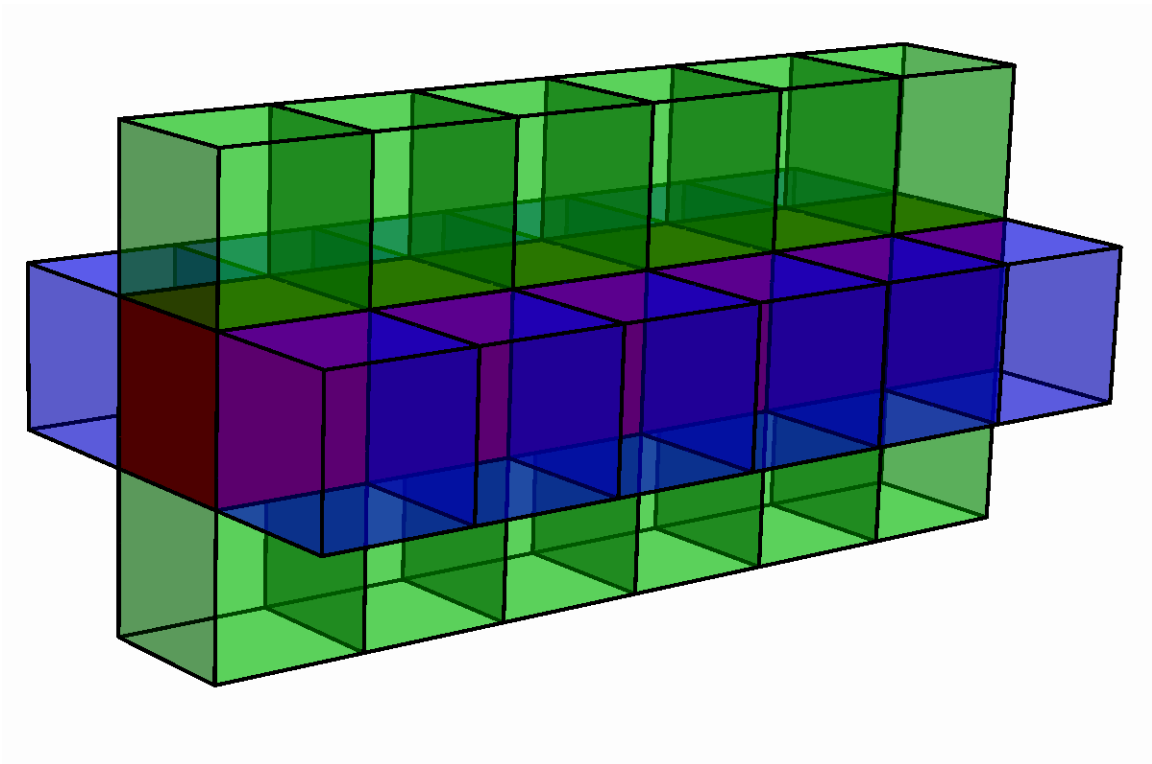
Figure 38   Sample line in the x-direction

When this procedure is followed for the x-direction, Eq. 16 is reorganized to form Eq. 18:

$$-\frac{1}{2}\frac{\alpha\,\Delta t}{\Delta x^2}T_{m,n-1,p}^{k+1/3} + \left(1 + \frac{\alpha\,\Delta t}{\Delta x^2} + \frac{\alpha\,\Delta t}{\Delta y^2} + \frac{\alpha\,\Delta t}{\Delta z^2}\right)T_{m,n,p}^{k+1/3} - \frac{1}{2}\frac{\alpha\,\Delta t}{\Delta x^2}T_{m,n-1,p}^{k+1/3} =$$

$$T_{m,n,p}^{k} + \frac{\alpha\,\Delta t}{\Delta x^2}\left(\frac{T_{m,n-1,p}^{k} - 2\,T_{m,n,p}^{k} + T_{m,n+1,p}^{k}}{2}\right)$$

$$+ \frac{\alpha\,\Delta t}{\Delta y^2}\left(\frac{\left(T_{m-1,n,p}^{k+1/3} + T_{m-1,n,p}^{k}\right) - 2T_{m,n,p}^{k} + \left(T_{m+1,n,p}^{k+1/3} + T_{m+1,n,p}^{k}\right)}{2}\right) \quad \textbf{(18)}$$

$$+ \frac{\alpha\,\Delta t}{\Delta z^2}\left(\frac{\left(T_{m,n,p-1}^{k+1/3} + T_{m,n,p-1}^{k}\right) - 2T_{m,n,p}^{k} + \left(T_{m,n,p+1}^{k+1/3} + T_{m,n,p+1}^{k}\right)}{2}\right)$$

Although the right hand side of the equation appears very complicated, is it composed entirely of known quantities (or at least, quantities that are being treated as if they were known). When this equation is recast in matrix form (Eq. 38), [A] now has the form of a tri-diagonal matrix and can be inverted easily.

Once the temperatures along this line have been determined, the process is repeated for the next line in the same direction. Figure 39 illustrates the process for lines oriented in the x-direction. Beginning with back edge on the upper face, successive x-directed lines (red) are solved until the entire top surface has been addressed. The lines in
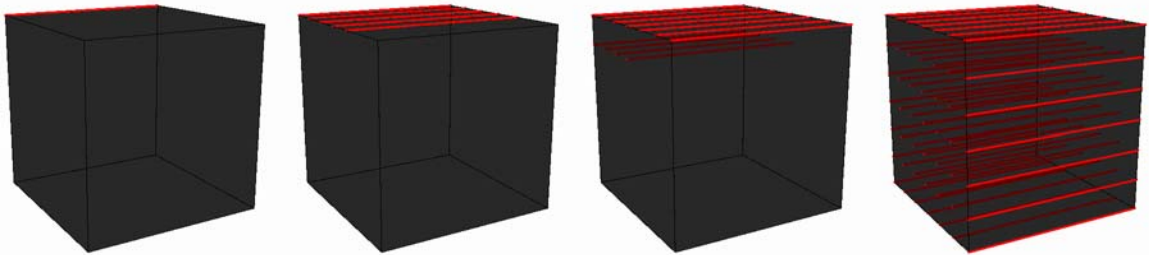
Figure 39   Sequence of solution for x-directed lines

the next plane of nodes are solved in the same way, continuing until the entire domain has been addressed. This entire process is repeated for y-directed lines (using time steps of k+2/3 and k+1/3 in place of k+1/3 and k, respectively), and then for z-directed lines (using k+1 and k+2/3 in place of k+2/3 and k+1/3, respectively). After one complete set of iterations, the pattern of lines will be have been something like what is depicted in Figure 40, in which the red lines correspond to the x-direction, the blue lines to the y-direction, and the green lines to the z-direction.
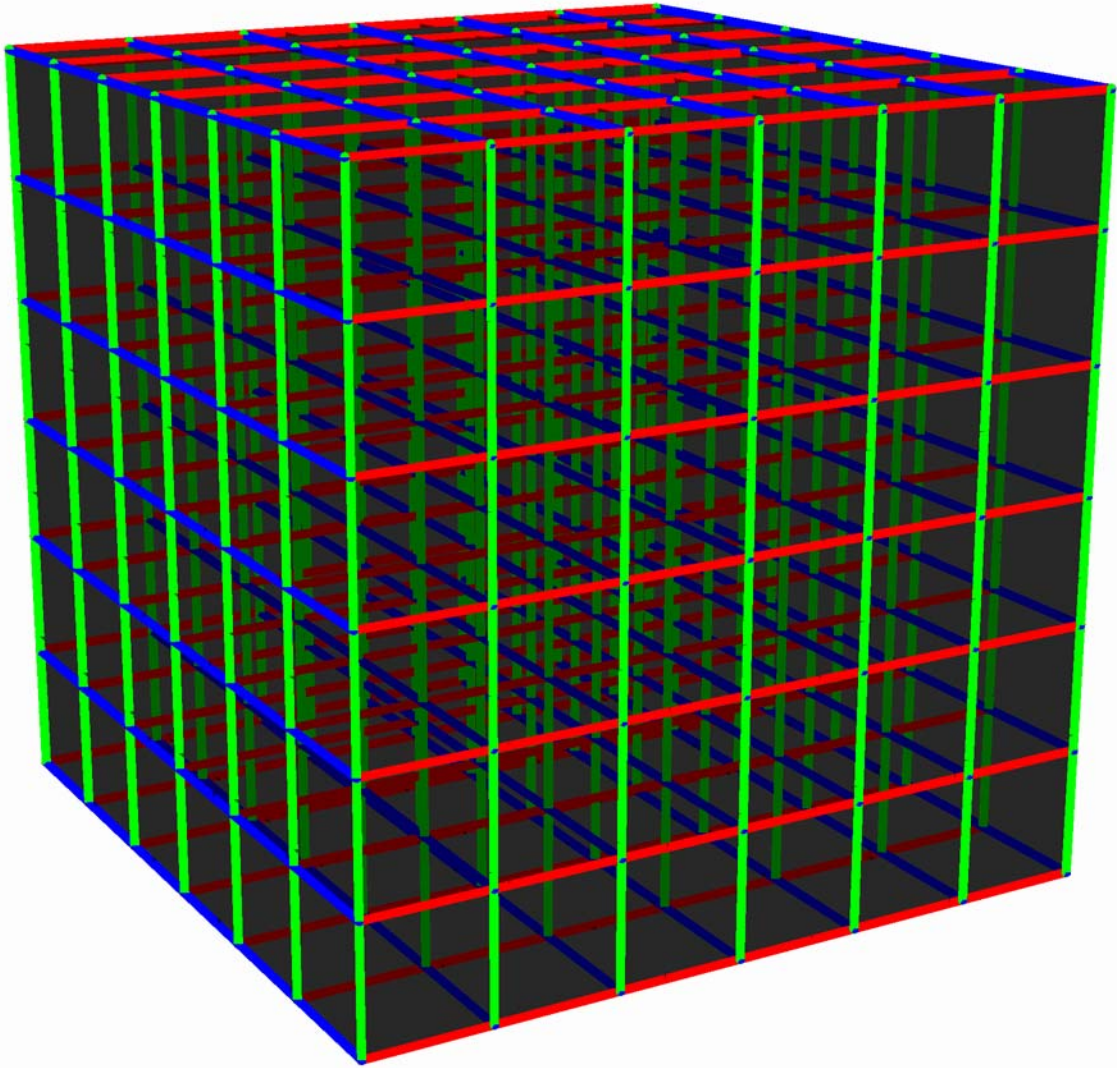
Figure 40   Pattern of lines for one complete iteration

After each sequence of lines — one iteration — is completed, the temperatures

throughout the domain before and after the iteration are compared. If the maximum

difference is greater than the convergence criterion, the solver performs another iteration

at the same time step. If the difference is less than the criterion, the solver advances to

the next time step and repeats the whole procedure. This continues until either the

86

maximum time step is reached, or until steady state is reached (determined by comparing

two successive time steps against a convergence criterion).

Although the preceding discussion focused only on the equations for a body

element (rather than a surface, edge or corner element), there are, of course, important

changes to the equations for the boundary elements; the nature of these changes depends

entirely on the nature of the boundary conditions at that element. For a specified

temperature (Dirichlet) boundary condition, the equation — to the extent that it is needed

at all — reduces to Eq. 19:

$$T_{m,n,p}^{k+1} = T_{m,n,p}^{k} \tag{19}$$

For an incident heat flux (Neumann) or specified convection coefficient (Robin), the

change in the equation depends heavily on which surface is being considered, and which

kind of boundary element (surface, edge, or corner). Generally speaking, the practical

implementation of the boundary conditions is accomplished as follows: each boundary

node is associated with three parameters — the type of boundary condition at that node,

the incident heat flux at that node, and the convection coefficient acting at that node

(these last two parameters are specified even for nodes subject to Dirichlet conditions;

they simply have no effect in that case).

The completed code was verified by taking advantage of the fact that a multi-

dimensional conduction problem can be solved using a product of several one-dimension

solutions [7]. By setting the boundary conditions for the surfaces in two coordinate

directions as insulated, the geometry approximates a one-dimensional problem. The

solver was tested using both fixed temperature boundary conditions and constant heat

flux/convection coefficient boundary conditions. Solving these problems in each coordinate direction and comparing the numerical solutions to the exact solutions provided a simple way to verify that the solver was functioning correctly. The details of this procedure, including the specific boundary conditions and graphical and statistical comparisons between the calculated values and the exact solutions, are provided in Appendix A.

COMSOL model of the array and package

While the 3-D conduction solver described above allows the user to easily specify an arbitrary surface temperature distribution, it is limited in that it treats only the silicon die itself. And while the conditions at the top surface will be known, the sides and back are in contact with the rest of the package; epoxy on the sides and kapton tape at the back. The boundary conditions imposed therefore are not as straightforward. To get a better understanding of these boundary conditions, a model of the diode array chip and associated packaging was developed using COMSOL, a commercial finite element analysis software package.

To simplify the calculations and reduce the memory requirements, the left/right and front/back symmetries were used, so only a quarter-package model was developed. Nearly the whole package was modeled; only the pins were omitted. At first, this was intended to be only a temporary omission — because the pins act as extended surfaces, it was not clear if they would need to be included in a later revision of the model. Once a constant surface temperature condition was selected, however, the effect of the pins could safely be ignored. The overall geometry is shown in Figure 41. A closer view of the

silicon die region is shown in Figure 42, better showing the relationship between the
silicon die, the kapton tape die attach, and epoxy fillet, as well as the pressure relief hole
drilled in the back of the package. Table 12 lists the material properties used in the model
(the PGA package is assumed to be made of alumina). Finally, the meshed model is
shown in Figure 43.
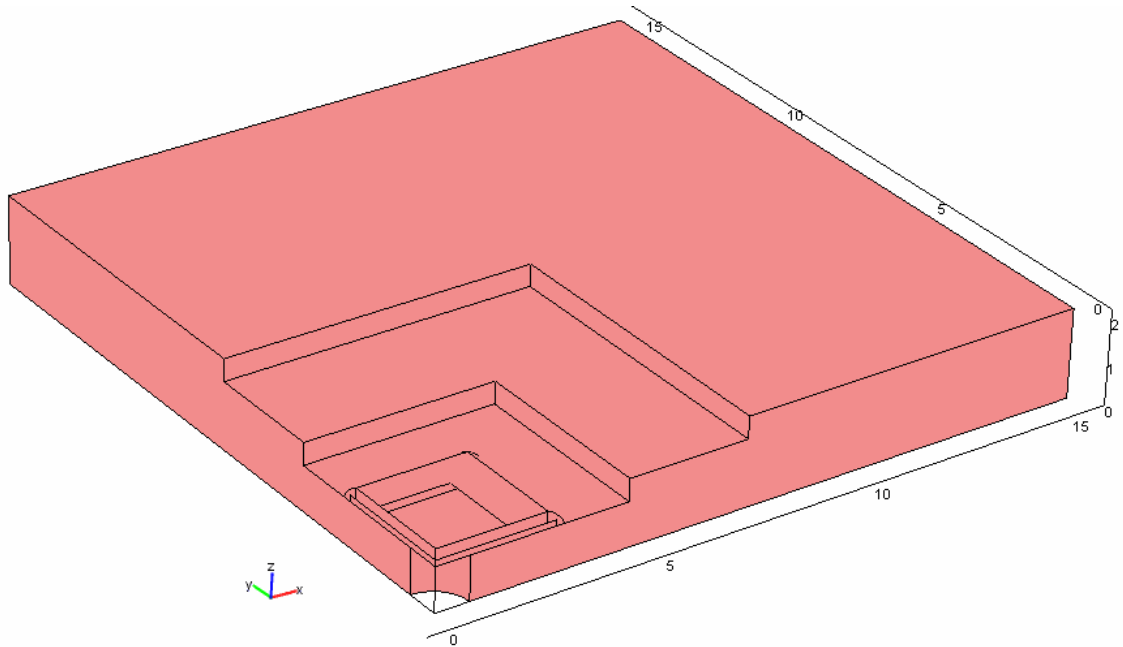
Figure 41   Quarter-package geometry in COMSOL (units in mm)
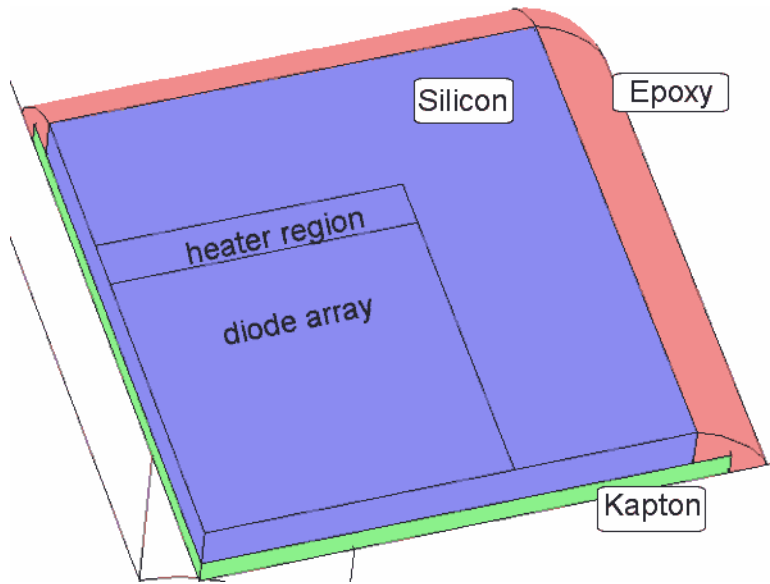
Figure 42   Close-up of diode array chip region

Table 12   Material properties for COMSOL model

	Silicon	Kapton	Epoxy	Alumina	FC-72
k (W/m² K)	153	0.191	0.8	18	0.057
ρ (kg / m³)	2330	1420	1700	3690	1680
c_p (J / kg K)	705.5	747	1300	880	1100
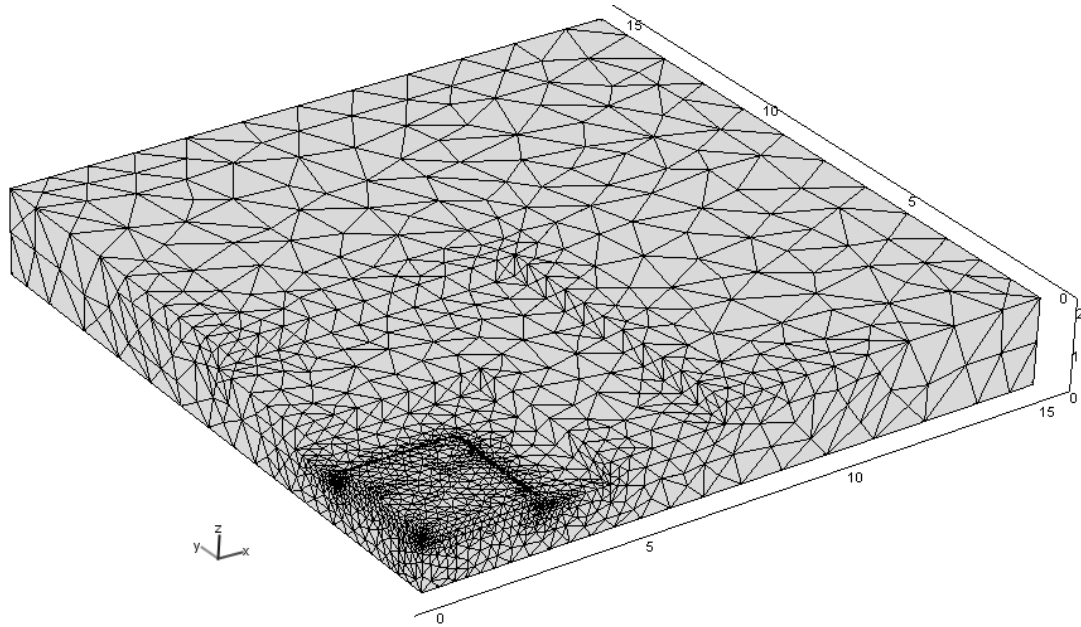
Figure 43   COMSOL model mesh (units in mm)

Note the fine mesh evident in the vicinity of the diode array; this is a consequence of the

small thicknesses of the silicon die and the kapton tape layer, and of the irregular shape of

the epoxy fillet. Because of these considerations, it was not possible to extend the

COMSOL model to consider the full-package and still adequately refine the mesh.

Once developed, the COMSOL model was used to support the 3-D conduction

solver in two ways. First, the COMSOL model was used to determine the boundary

conditions that should be used for the 3-D conduction solver. Second, the COMSOL

model was used to estimate the transient response of the package to a change in the

surface temperature of the chip. In this way, the two approaches complement each other.

The strength of the COMSOL model — the ability to easily handle multiple materials and

the irregular package geometry — compensates for the simple geometry and treatment of

a single material required by the 3-D conduction solver. At the same time, the COMSOL

91

model is limited to a quarter-package geometry by memory considerations, while the 3-D

conduction solver domain includes the entire silicon die. Also, the 3-D solver easily

accepts the measured temperature distribution as the boundary condition over the top

surface; while this would be possible with the COMSOL model, the necessary

implementation is complicated and difficult.

To determine the boundary conditions at the epoxy-silicon and kapton-silicon

interfaces, several steady state simulations were performed. In each, a constant 0 °C

temperature boundary condition was applied over the surface of the package, and a

temperature difference was applied to the top surface of the chip. Representative results

for a surface temperature of 10 °C are shown in Figures 44 – 48. Figure 44 shows the

temperatures over the surface. Notice that the silicon has a very uniform temperature, in

contrast to the sharp temperature gradients across the kapton tape and epoxy fillet.
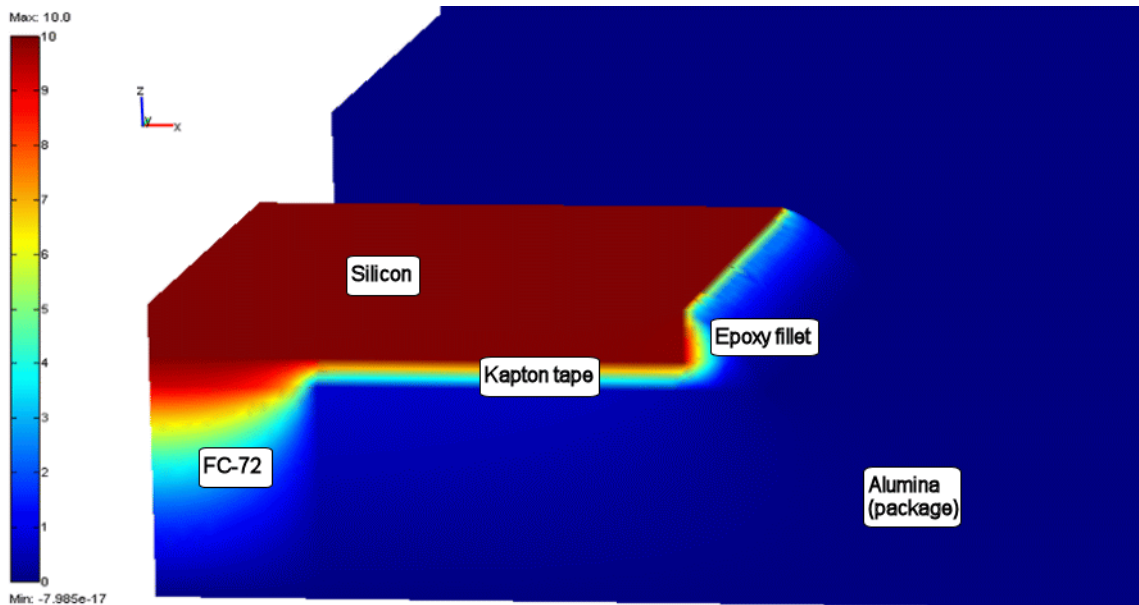
Figure 44   COMSOL temperature results (°C increase over ambient)

Figure 44 only shows the outer surface boundary; the true regions of interest are the back and side surfaces of the silicon itself, in contact with the kapton or epoxy. The side surface temperature and heat flux distributions are shown in Figures 45 and 46, and the back surface temperature and heat flux distributions are shown in Figures 47 and 48. These figures show the uniformity of these distributions, so an average value can be used to represent the overall distribution.
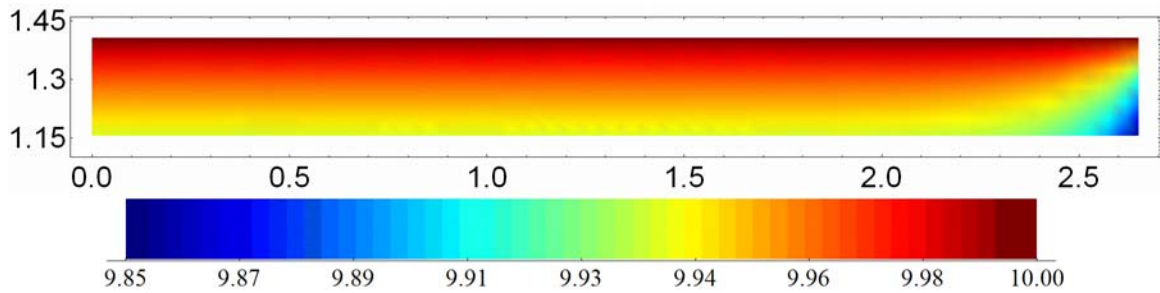
Figure 45   Si/epoxy fillet interface temperature results (°C rise over ambient)
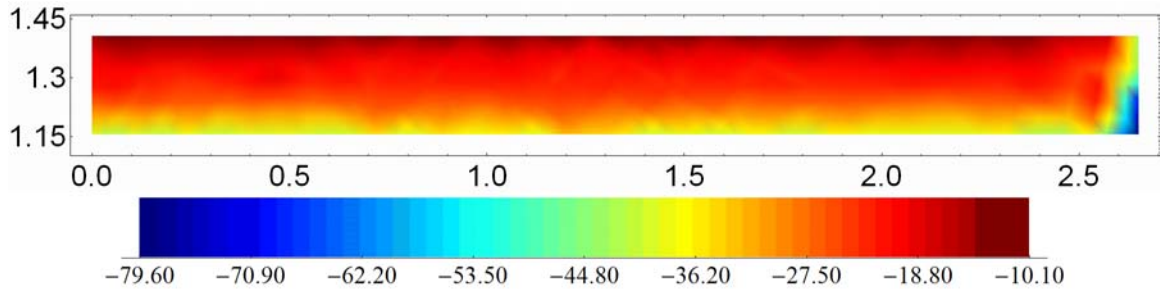
Figure 46   Si/epoxy fillet heat flux distribution (mW/mm^2)
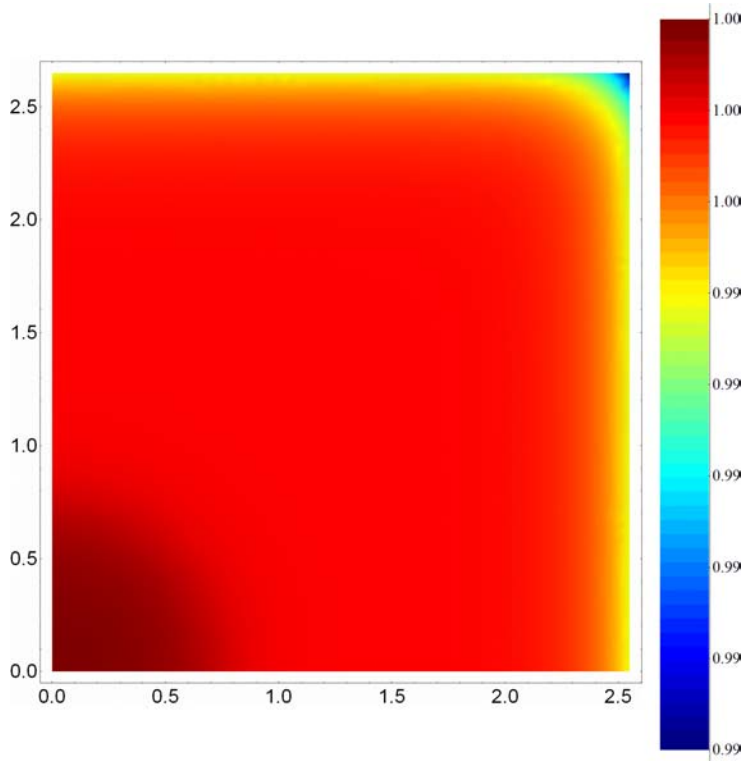
Figure 47   Si/kapton tape interface temperature
             results (°C rise over ambient)
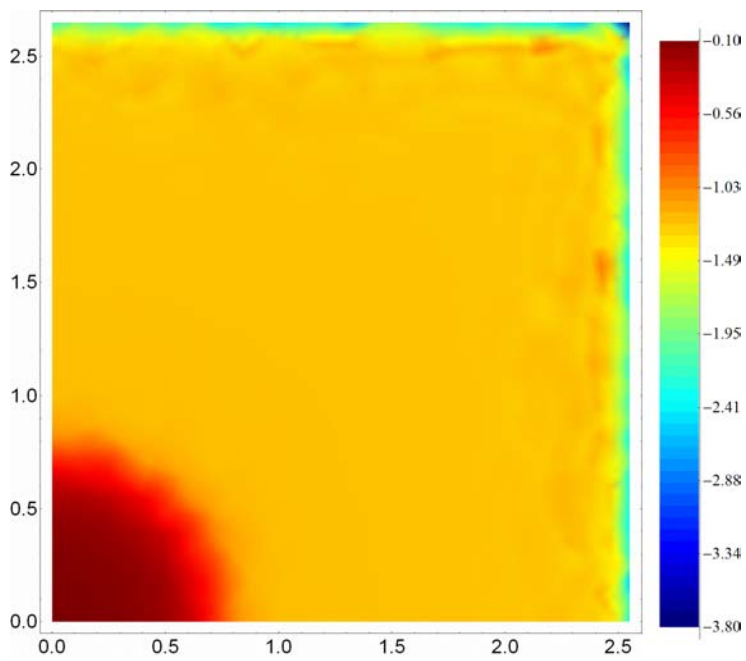
Figure 48   Si/kapton tape interface heat flux results
             (mW/mm^2)

For each simulation, the average temperature and heat flux values were determined for the back surface and both side surfaces. Figure 49 shows these values plotted against each other. The results are almost perfectly linear, with r^2 exceeding 0.9999 for all three cases. Because this is only a simulation, however, this is not completely unexpected.
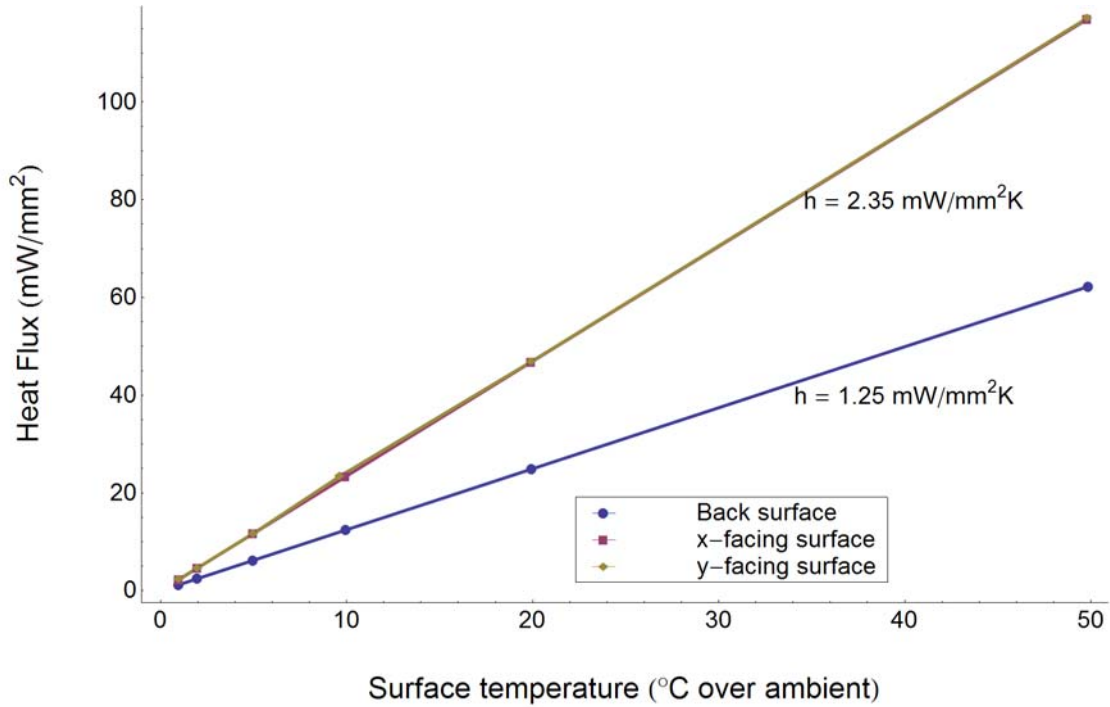
Figure 49   Results for side-back conduction losses

The second question addressed by the COMSOL was the time required to reach steady state. Because of the small size of the package, this time is expected to be rather short, but a concrete, quantitative value is difficult to estimate analytically. Fortunately, using the COMSOL model, such an estimate is easy to produce. First, the steady state solution is computed and the resulting temperature distribution is integrated over the silicon, caption, and PGA package domains. The value of this integral will be

proportional to the thermal storage in each region. Then a transient solution is computed, and the temperature distribution at various intermediate times is integrated in the same way. These values are compared against their steady state values. When the transient values reach, 99 % (or any other suitable, arbitrary threshold) of the steady values, steady state can be associated with that time. As can be seen in Figure 50, the chip reaches steady state almost immediately (about 5 ms). This is hardly surprising considering the high thermal diffusivity and small thickness — 93 mm^2/s and 0.25 mm, respectively. The kapton tape and package take longer, but both have reached steady state by about 0.5 s.
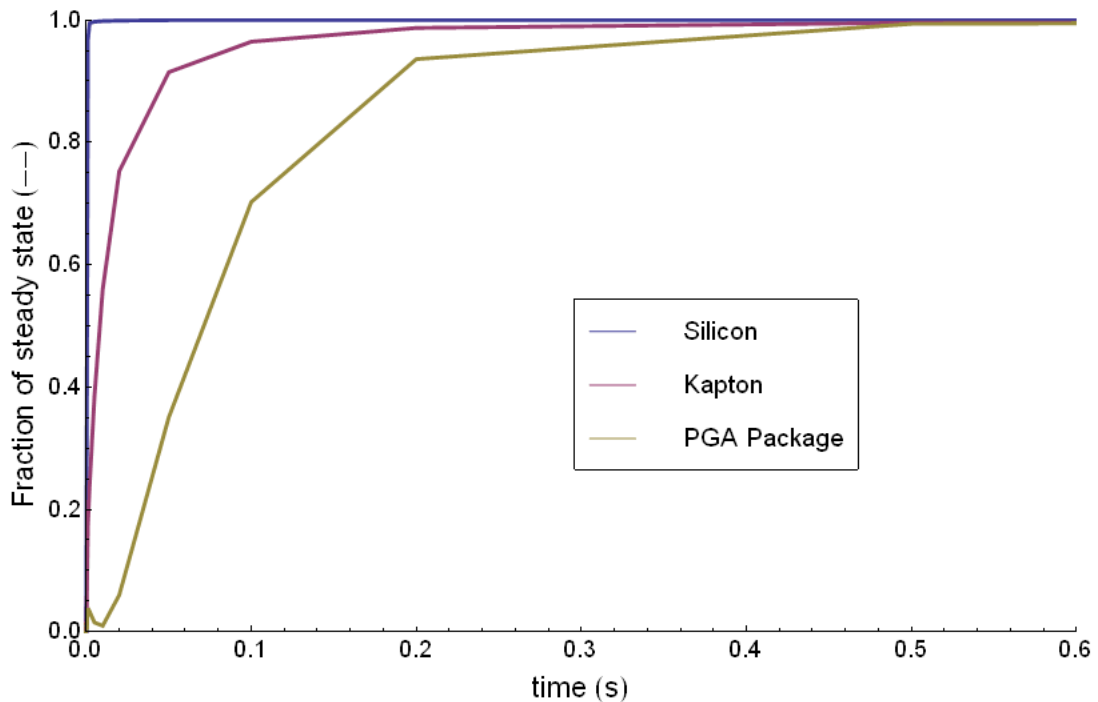
Figure 50   COMSOL transient results

Based on these results the equivalent time constant τ can be estimated for each region. This time constant can be determined by fitting the above results to an expression of the form given in Eq. 20:

96

$$E_{stored}(t) = E_{stored,ss}\left(1 - \exp(- t / \tau)\right) \tag{20}$$

Table 13 reports the results from these calculations.

Table 13   Time constants for package elements

Region	Time constant, τ (ms)	Regression coefficient, r^2
Chip	0.291	0.999
Kapton tape	11.7	0.997
Package	99.1	0.993

Summary

This chapter described the development of the 3-D conduction solver that will be used to determine the substrate conduction losses. The solver uses an operator-splitting algorithm implemented in C++, and considers a rectangular parallelepiped domain composed of a single material, which corresponds to the silicon die on which the diode array is fabricated. Because the bottom and side faces of the silicon are not exposed to the environment but are in contact with the kapton tape and epoxy fillet, respectively, it is not clear what boundary conditions are appropriate for these surfaces. To answer this question, a second numerical model was developed using COMSOL finite element software. Because the package is symmetric in the left/right and front/back directions, only a quarter-package was modeled, and the silicon die, epoxy fillet, kapton tape, and ceramic (alumina) package regions were included in the model. Using the COMSOL model, it was determined that the predicted heat losses at each surface could be modeled as convective losses, with convection coefficients of 2.35 and 1.25 mW/mm^2 K for the bottom and side faces, respectively. The COMSOL model was also used to estimate the

time required for the package to reach steady state after a change in the surface heat flux was applied. The package was found to reach steady state after only 0.5 s.

Chapter 6: Diode Characterization

Before the diode array was used, five tests were performed to characterize its behavior. The first test determined the effect of sensing current on the temperature sensitivity. Since sensing current supplied by the interface board cannot easily changed, several diodes were tested individually. These tests are referred to as the "Single-diode calibrations." Once the preferred sensing current was identified, the next step was to set the interface board to use that current and determine the temperature sensitivity for each diode in the array. This test is referred to as the "Full-array calibration."

The next two tests investigated deviations of the diodes from the ideal models discussed in Chapter 3. The third test used a simplified interface board that simulated activating two diodes from the same row in turn and measured the time required for the diodes to turn on or off. This test is referred to as the "transient test." The fourth test determined the ohmic resistance associated with each diode; this once again required varying the current, so several diodes were tested individually. This test is referred to as the "parasitic resistance" test.

The final test operated the heater in a quiescent FC-72 bath so that heat transfer from the surface would be dominated by natural convection. This addressed two concerns. First, it offered a way to identify diodes that were not responding properly, so that they could be eliminated from future consideration. Second, the natural convection measurements allowed a verification of the substrate conduction boundary conditions determined in Chapter 5. This test is referred to as the "natural convection" test.

Single-Diode Calibration

The first set of tests determined the temperature response for diodes operating individually. In these tests, the primary assumption is that the diodes obey a simple, linear response, expressed by Eq. 21:

$$V_D = mT + b_2 \qquad\qquad (21)$$

The single-diode calibration test were performed on one of the Model I chips and were intended to both verify the expected diode response and explore the effect of the sensing current on the diode sensitivity.
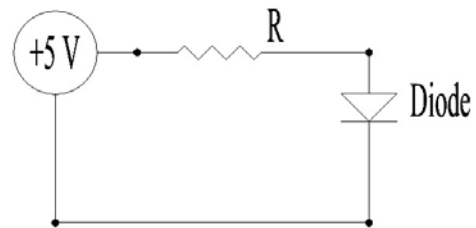
Figure 51   Single-diode test circuit

The test circuit shown in Figure 51 was used, and the current was adjusted by changing the resistor R. Three values of R were used: 400 kΩ, 40 kΩ, and 4 kΩ, corresponding to 11 μA, 110 μA, and 1100 μA, respectively. Two such tests were performed. In each, the test procedure began by making a measurement at room temperature, then increasing the oven setting.
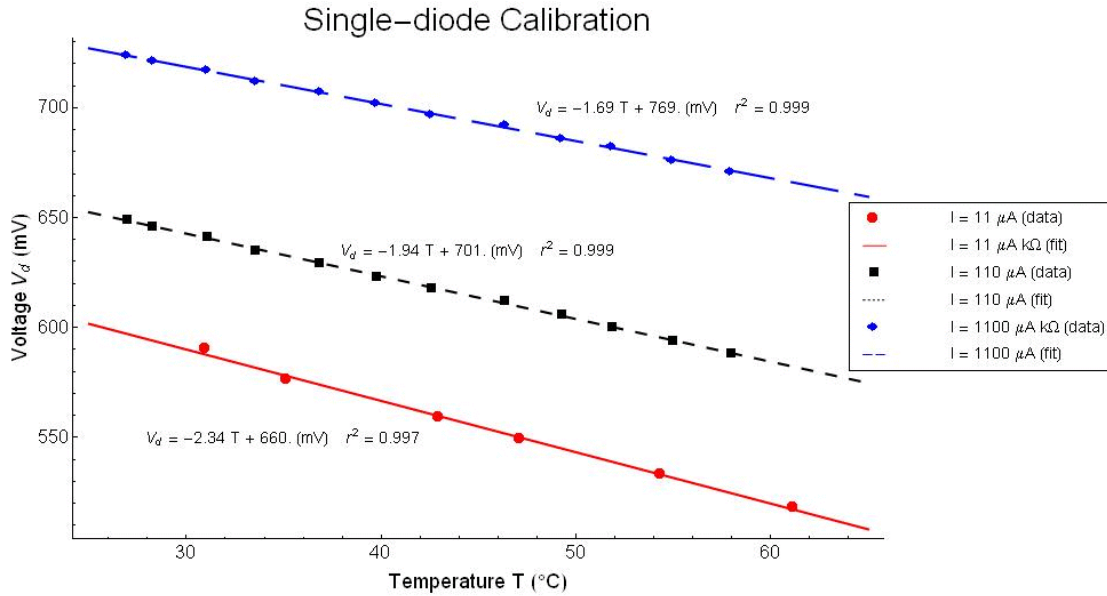
Figure 52   Single-diode calibration results for Model I design

The results are shown in Figure 52. First, the diode behavior is described very well by the linear model, with r^2 coefficients exceeding 0.99. Second, the sensitivity is in the neighborhood of -2 mV/°C for each case, as was expected. Finally, the sensitivity increases as the sensing current decreases. This is fortunate, because the lower sensing currents are associated with lower values of self-heating. Selecting a lower sensing current not only reduces the impact of the test on the temperature but also improves the quality of the measurement itself.

Full-array Calibration

Although the single-diode tests successfully demonstrated their goals – verifying that the diodes functioned as expected and identifying the effect of sensing current on temperature sensitivity – it would not be prudent to rely on the single-diode calibrations to determine the local temperature distribution. The obvious approach would be to use

the interface board to obtain a "raw" sensitivity for each diode by simply setting the gain to unity and the offset to 0 V, then collecting data for the whole array over a range of temperatures. This approach fails to consider the signal conditioning that transforms the -2 mV/°C sensitivity to 200 mV/°C.

Once the signal conditioning is taken into consideration, the simplistic linear relationship considered thus far is no longer sufficient. The voltage reported to the data acquisition system is described by Eq. 22:

$$V_m = G\left(V_{DC} - V_D\right) \tag{22}$$

One could presumably combine Eqs. 21 and 22 to produce an "extended" linear relationship, as shown in Eq. 23:

$$V_m = \left(-mG\right)T + \left(G(V_{DC} - b_2)\right) \tag{23}$$

Thus the calibration expression could be tuned to match the offset being applied for a given test, which seems reasonable considering that the offset will not be changed during any given test run. Mathematically, this approach is sound, but it makes the critical assumption that the gain will be known exactly and will be the same for every diode. This is not a reasonable assumption. At the very least, the gain will vary from row to row, because each row has its own amplifier with its own gain resistor. In addition, because each diode has its own circuit path, which could differ substantially from its neighbors, the voltage measurement for each will be attenuated differently, and so each will experience a different apparent gain.

A better approach extends the calibration as a 3-D process. The process described above can be considered as a 2-D, linear calibration with the DC offset considered as a constant parameter. A better approach treats the DC offset as a separate, independent variable. Again, combining Eqs. 21 and 22, but separating the offset term yields Eq. 24:

$$V_m = \left(-mG\right)T + GV_{DC} + \left(-Gb_2\right) = aT + b_3V_{DC} + c \qquad \textbf{(24)}$$

Just as Eqs. 21 and 23 describe a line – a linear relationship in two dimensions – Eq. 24 describes a plane – a linear relationship in three dimensions. In addition, because each diode will be characterized by its own set of three coefficients (a, b, and c) variations specific to each diode will be accounted automatically. Finally, because of the way the offset voltage V_{DC} is measured, this 3-D approach is extended still further. As discussed in the data acquisition section, the offset voltage is determined from measurements of a nominal offset voltage and fluctuations relative to this value, according to Eq. 14; combining Eqs. 14 and 24 yields Eq. 25:

$$V_m = aT + b_3\left(V_{DCbaseline} + \frac{\Delta V_{DC}}{G_{offset}}\right) + c \qquad \textbf{(25)}$$

This is the equation used for the analysis of the calibration data.

The physical setup for calibrating the array as a whole does not differ much from the setup described for the single-diode calibration for the Model III design. The same thermocouple attachment technique, thermocouple reader and oven were used. The only significant difference was that the male end of the extension board was plugged into the interface board rather than the single-diode test board. Figure 53 shows the physical setup.
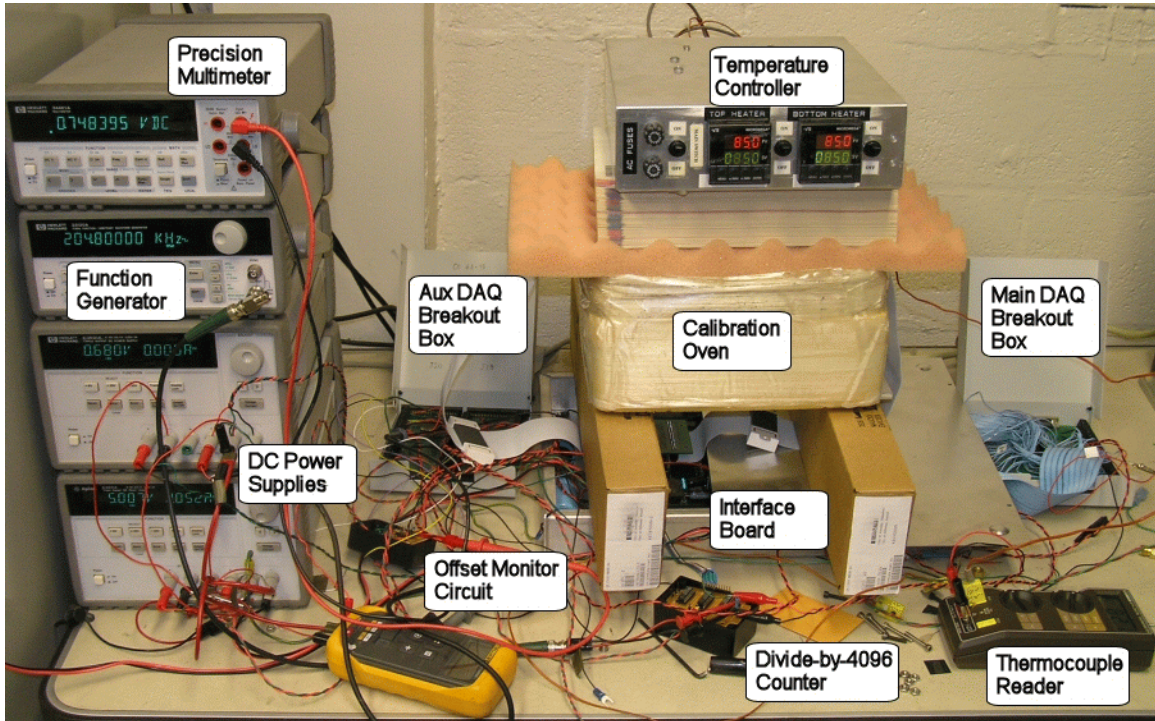
Figure 53   Array calibration test setup

The calibration test was performed according to the following procedure :

1. Attach the thermocouple to the package, insert the diode array assembly into the extension board, and place it in the oven as shown in Figure 54.
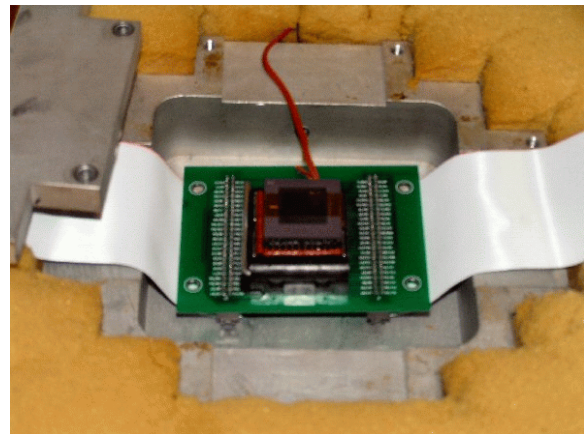
Figure 54   Diode array in calibration oven

2. Turn on the power supplies, function generator, and precision multimeter. Set the function generator for 204.8 kHz.

3. Begin the data acquisition software, select the External Clock, Dual Acquisition module, and begin monitoring and logging the thermocouple reader.

4. Collect the first set of calibration runs at room temperature, using the nine DC

    offsets reported in Table 14.

5. Set the oven to the next temperature, again per Table 14.

6. When the diode array temperature remains constant for two consecutive 10 minute

    periods, collect the next set of calibration runs, again using the nine DC offsets

    listed in Table 14.

7. Set the oven to the next temperature and repeat.

Table 14   Array calibration temperatures and DC offsets

Temp (°C)	DC Offset (mV)								
	1	2	3	4	5	6	7	8	9
25.4	758	763	768	773	780	785	787	792	800
43.6	734	739	743	751	753	758	763	768	775
62.9	709	714	719	724	729	734	739	743	748
82.8	680	685	690	695	700	704	709	714	719

Because there are over 1000 diodes, the results for each diode will not be shown.

Instead, the results for one representative diode, located at position (10,10) are shown in

Figure 56. For this particular diode, Eq. 26 represents the calibration relationship:

$$V_m = 149\,T + 100.1\left(V_{DCbaseline} + \frac{\Delta V_{DC}}{100}\right) - 81423 \qquad (26)$$

where all voltages are in mV.

105
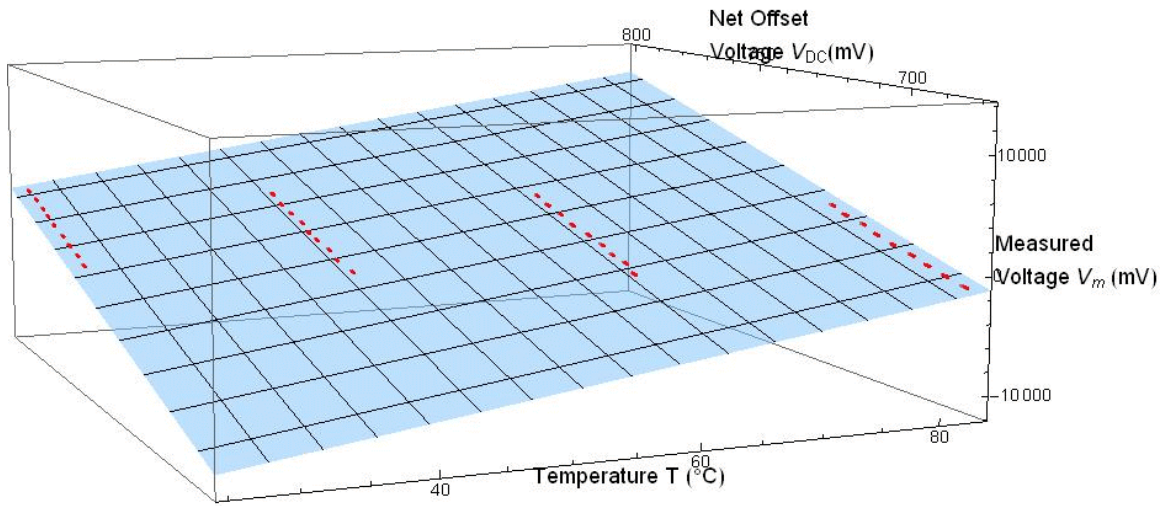
Figure 55   Array calibration test results for one diode

Given the scale of the overall figure and the number of points that comprise each temperature–DC offset pair, it is difficult to see the relationship of the plane to the raw data. Figure 56, therefore, presents a closer view of the calibration relationship in the vicinity of the T = 62.9 °C, V_{DC} = 729 mV calibration run.

The overall behavior is well described by the extended plane equation (Eq. 25). Of the 1024 regression analyses performed, 894 show an r^2 coefficient between 0.995 and 0.9997, 32 show an r^2
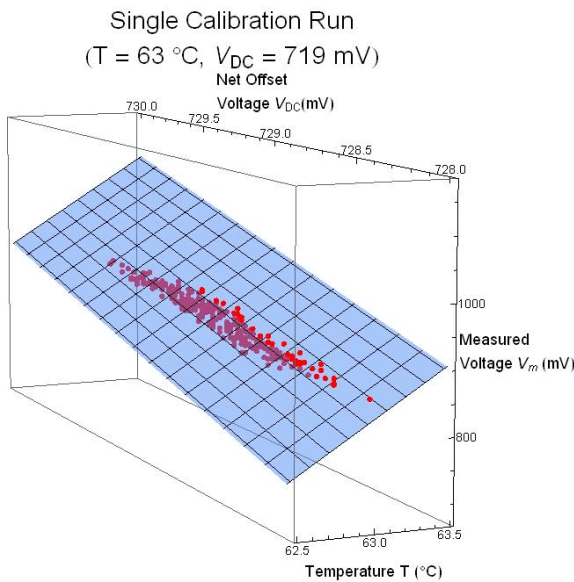
Figure 56   Single temperature-DC Offset combination
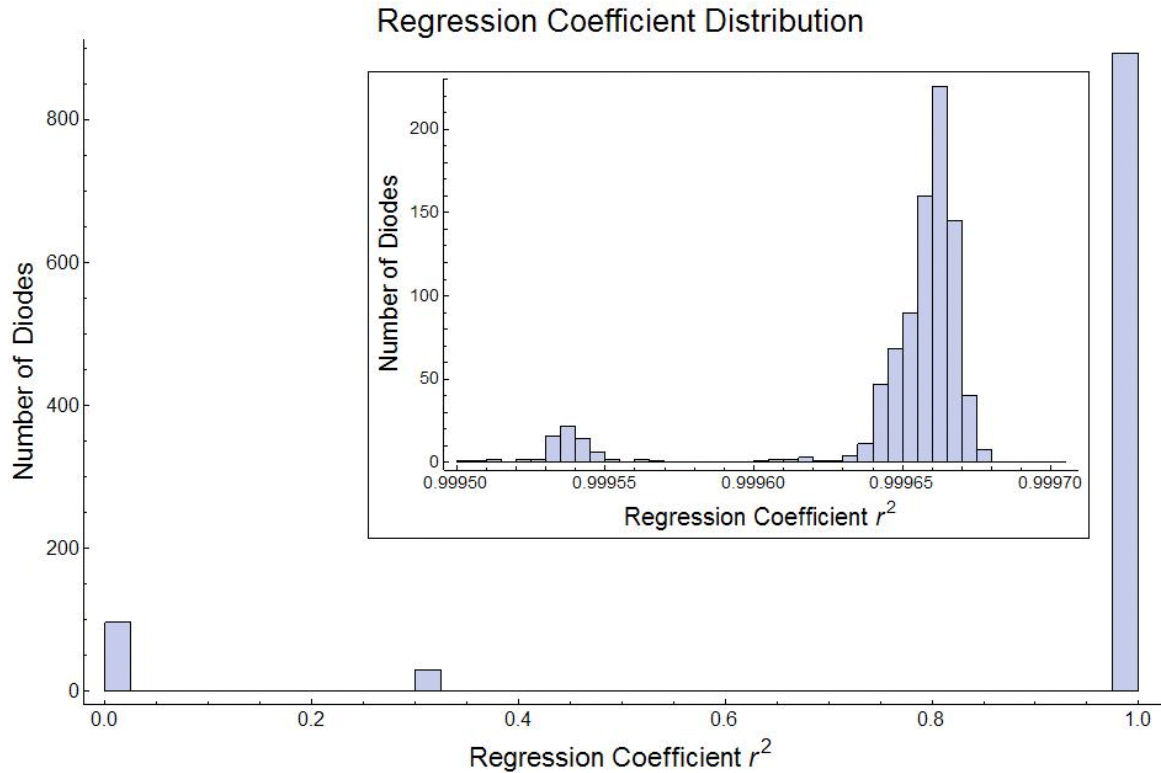
Figure 57   Distribution of regression coefficients

between 0.30 and 0.45, and 98 show no correlation whatsoever. Figure 57 shows a

histogram of the regression coefficients, inset with a more detailed view of the rightmost

histogram bar.

Further investigation reveals a pattern to how these bad diodes are distributed, as shown in Figure 58. The poorly correlated diodes are concentrated in column 18, and rows 11–13. These positions correspond to damage suffered by either the diode array itself or the interface board, as noted previously; therefore their poor correlation
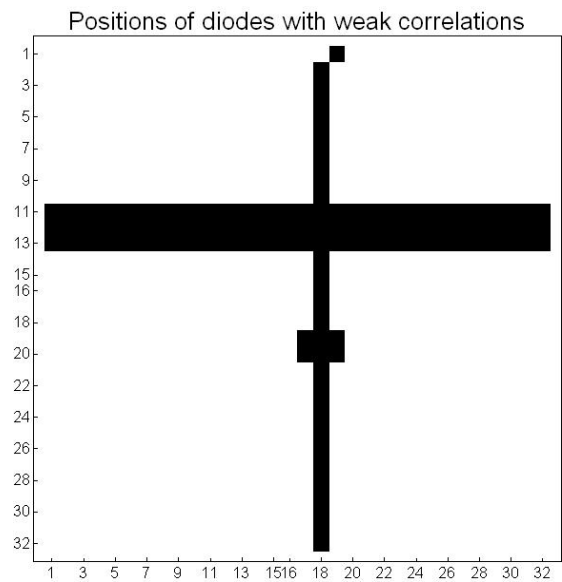
Figure 58   Positions of weakly correlated diode positions

should not be considered to reflect on the suitability of the model for the rest of the diode positions.

One additional point worth mentioning is the loss in sensitivity associated with the measurement in the array rather than singly. In the single-diode calibration section, the sensitivity for individual diodes was found to be close to -2 mV/°C; after signal conditioning, this should correspond to a coefficient of approximately 200 in Eq. 26, but that coefficient is only 149, or -1.49 mV/°C. As shown in the histogram of diode
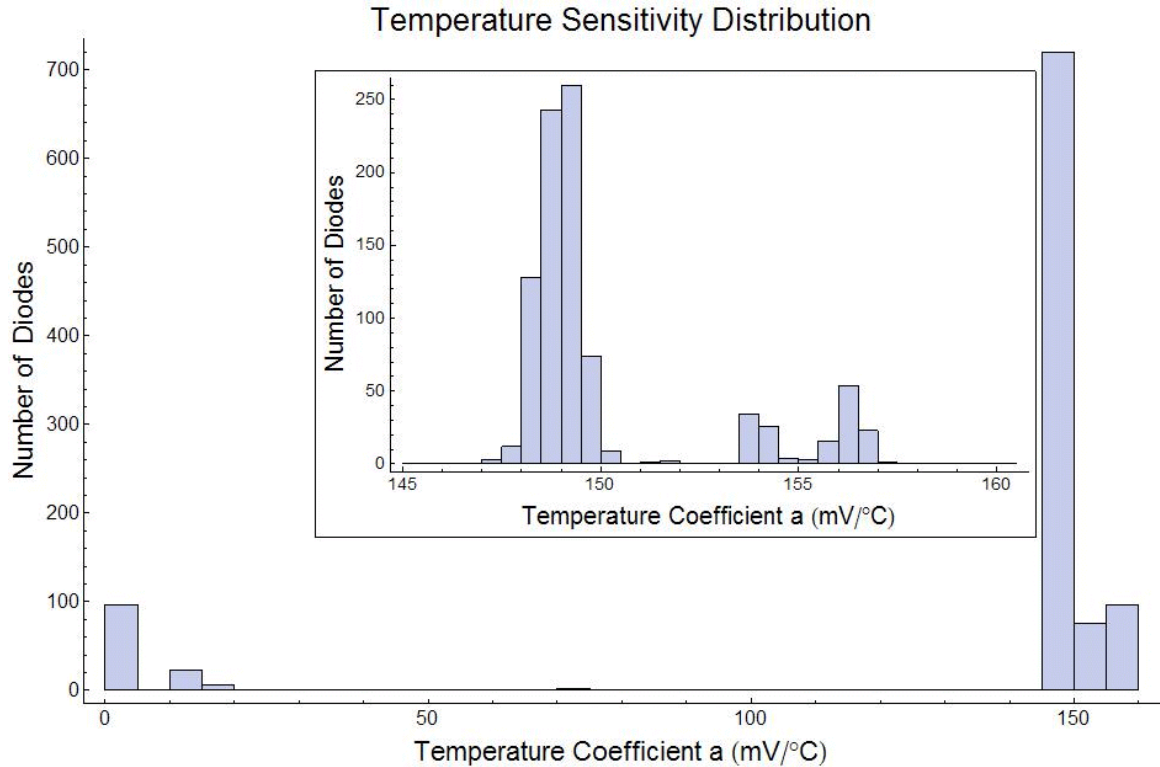
Figure 59   Diode sensitivity for the array calibration.

sensitivity for the array calibration, Figure 59, this is true for all of the diodes in the array. This figure includes all 1024 calibration calculations, and no diode has a sensitivity greater than about 158 mV/°C. The reason for this is not clear, but may be related to

temperature effects on parasitic resistances, whose effects manifest themselves only when the full array is operating. Because the parasitic resistance increases as the temperature increases, the voltage drop caused by the parasitic resistance also increases; this increase would offset the diodes' decrease with temperature, decreasing the apparent sensitivity.

Because the sensitivity is consistently in the neighborhood of 150 mV/°C over several such full-array calibrations, the loss of sensitivity was simply accepted and not investigated further.

Transient Test

Although an ideal diode would respond instantaneously when subjected to a forward or reverse bias voltage – conducting or blocking current, respectively – real diodes do not. In reality, there is a small but finite time lag in the diode response as the charge carriers within the p-n junction are redistributed in response to the change in the electric field. This phenomenon is known as "reverse recovery," and the time required for the diode to turn on or off imposes a direct limit on the maximum scanning frequency achievable by the diode array.

As discussed in Chapter 3, the diode array design is predicated on having only one

diode per row active at a time. Consider again the column-wise scanning process,

previously described in Chapter 3. Just before the column-switching event, the diodes in

column 1 are forward biased and active, while the diodes in column 2 are reverse biased

and inactive, as shown in Figure 60. The voltage at points A, B, and C is approximately

0.7 V Figure 61 depicts the conditions immediately following the event. The diodes in
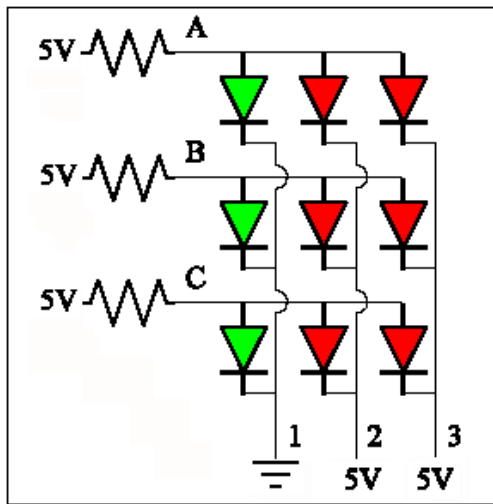
Figure 60   Diode array just prior to
             column switching event
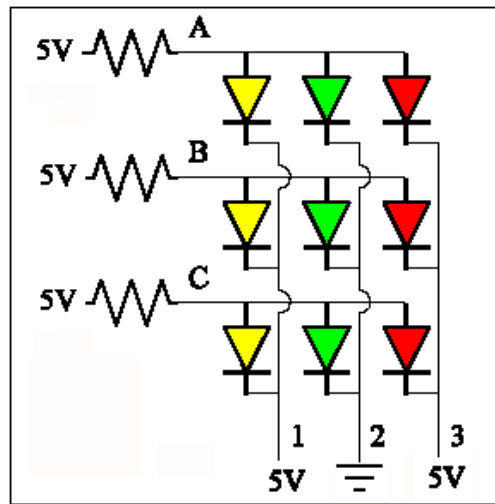
Figure 61   Diode array just following
             column switching event

column 2 are forward biased by approximately 0.7 V, while the diodes in column 1 and 3

are now reverse biased by approximately 4.3 V. Because of reverse recovery, however,

the diodes in column 1 do not immediately prevent current from flowing, but instead

allow some to flow. This current must still flow towards a lower potential, and so it

flows to ground through the (now active) diodes in column 2, temporarily adding to the

sensing current. The higher sensing current, in turn, artificially increases the voltage

measured at A, B, and C. As the charge distribution in the column 1 diodes reaches its new equilibrium, the extraneous current decays to zero and normal operation begins.

Because the measurements taken during the reverse recovery transient do not accurately reflect the temperature-induced changes in voltage drop, it is important to know how long this transient lasts. This was tested using the transient test board described in Chapter 4. An HP 3631A power supply provided the +5 V source, while an HP 33120A function generator provided the 0–5 V. A 16 kHz square wave was used, because this would produce step transitions at 32 kHz, corresponding to the expected column switching frequency. The voltage measurements were made using a Fluke 123 Scopemeter oscilloscope and recorded using Fluke View software. Channel 1 on the oscilloscope monitored the voltage at point A in the circuit, corresponding to the voltage drop across the active diode, while channel 2 monitored the function generator voltage. The voltage scales were 0.5 V/div and 5 V/div, respectively, while the time scale was set to 10 μs/div. The Fluke View software captured the oscilloscope trace data and exported it as a comma separated text data file.

The results of one such test are shown in Figure 62. The apparent noise in the source voltage should be attributed to the coarseness of the voltage scale, rather than to noise present in the signal. At each high/low transition, the diode voltage shows a short disturbance before settling to its steady state value. Figure 63 shows a zoomed view of the region with the circle. This view shows the duration of the transient as between approximately 4 and 6 μs.
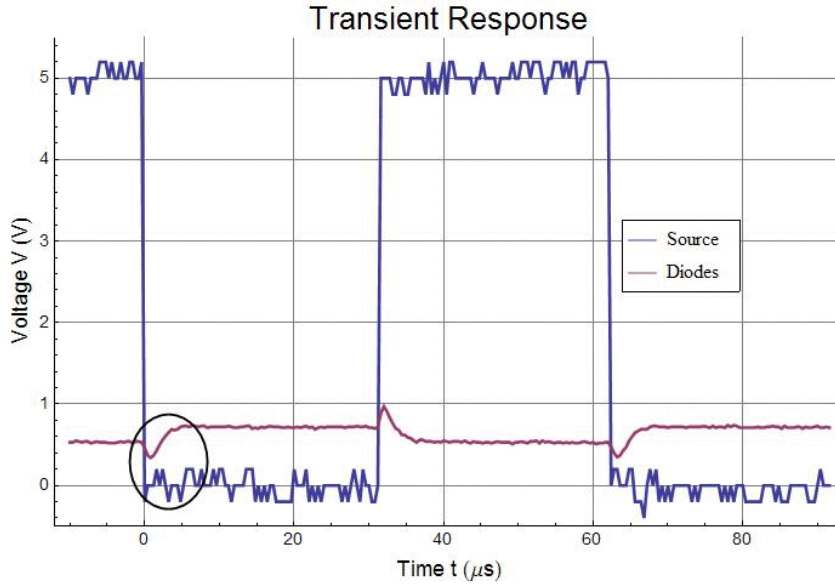
Figure 62   Transient test results
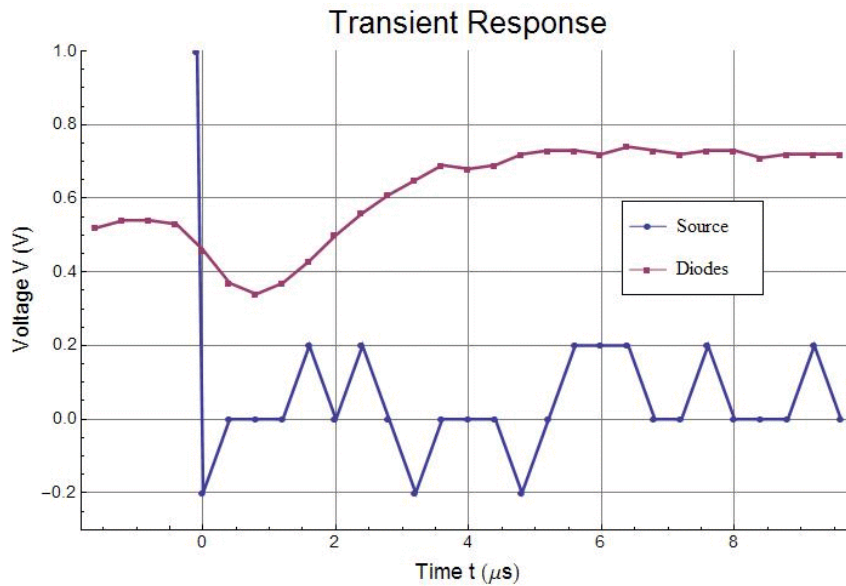
Figure 63   Transient results (zoomed)

Two conclusions can be drawn from this information: one pertaining to the

theoretical maximum surface scanning rate and one pertaining directly to data collection

in the present work. For the first, assume that a data acquisition system were available

112

with an infinite bandwidth. Even such a system would have to wait to collect data until the 6 μs interval had passed, therefore the maximum achievable column switching frequency would be 167 kHz. This would correspond to a surface scanning rate of 5.21 kHz. For the implications of the present work, consider that operating at the target column switching rate of 32 kHz requires an overall sampling rate of at least 1024 kHz, because each of 32 rows must be sampled at least once before advancing to the next column. This allows 0.977 μs per measurement; if reverse recovery requires 6 μs, then the first seven row measurements will be corrupted as a result of reverse recovery. Decreasing the column scanning rate to 3.2 kHz, the overall sampling rate falls to 102.4 kHz, allowing 9.77 μs per sample. This means only the first row would be corrupted as a result of reverse recovery.

Parasitic Resistance

The finite turn-on / turn-off time is not the only deviation from ideal behavior displayed by the diode. The ideal diode model assumes that only the p-n junction behavior contributes to the voltage drop across the diode. In reality, ohmic losses through the silicon also contribute to the voltage drop, as do the integrated circuit's metal layers and contact structures. Combining all of these losses into a single parasitic resistance, R_p, the effect is described by Eq. 27

$$V_D = V_{pn} + I_D R_p \qquad (27)$$

Combining Eqs. 27 and 4, the behavior of a real diode is given by Eq. 27:

$$I_D = I_S \left(\exp\left(\frac{V_D - I_D R_p}{k T / q} \right) - 1 \right) \qquad (28)$$

113

A test was performed to identify both the parasitic resistance and the saturation current. Using the single-diode test board, the voltage drop was measured each diode at each of 12 sensing currents (achieved by replacing the current limiting resistor, according to Table 15). The test was performed for both the Model I and Model II designs.

Table 15   Current limiting resistors used for parasitic resistance test

Test resistor no.	1	2	3	4	5	6	7
Resistance (Ω)	51.2	100.2	200	400	803	1496	3000

Test resistor no.	8	9	10	11	12	13
Resistance (kΩ)	6.05	12.73	22.15	48.8	100.3	200.6

The Model I design results are shown in Figures 64 and 65, while the Model II design results are shown in Figures 66 and 67. In each pair of figures, the first plot shows the data in linear coordinates, while the second shows the data in semilog coordinates. Considering the data in the linear axes, the linear behavior associated with Ohm's law is evident for high values of voltage and current; the wide spread of the data indicates a span of parasitic resistances. Because the individual diodes are all of identical design and share connection points, this suggests that the metal traces dominate the parasitic resistance. Next, considering the data in the semilog axes, the exponential relationship between voltage and current is clearly evident for low values of current and voltage. The close clustering of the data in this region suggests that all diodes have the same saturation current. Again, because the individual diodes are all of identical design, this is consistent with expectations.

114
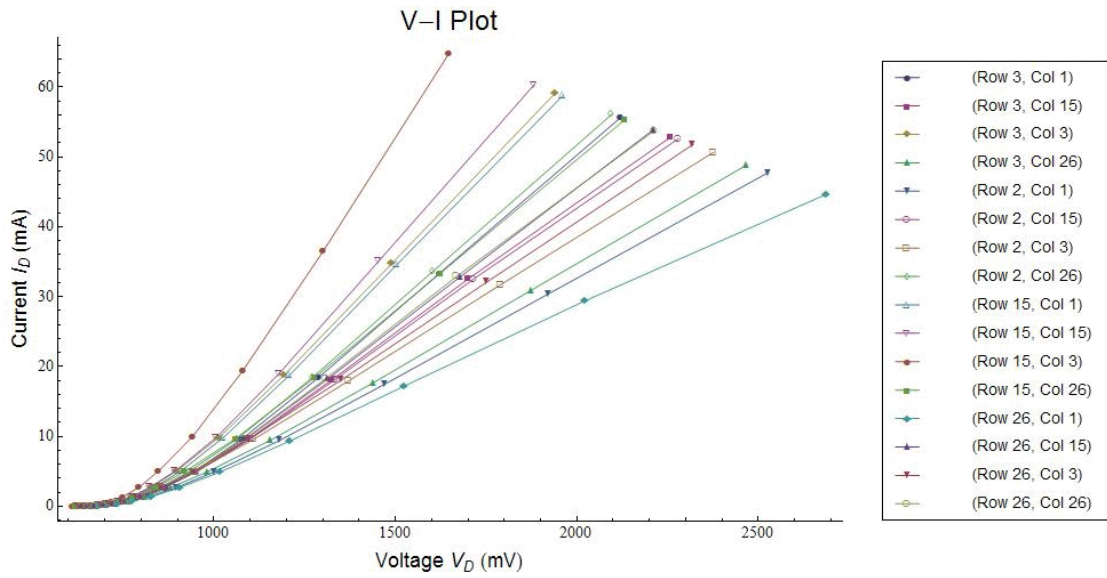
Figure 64   Parasitic resistance test results for Model I array (linear)
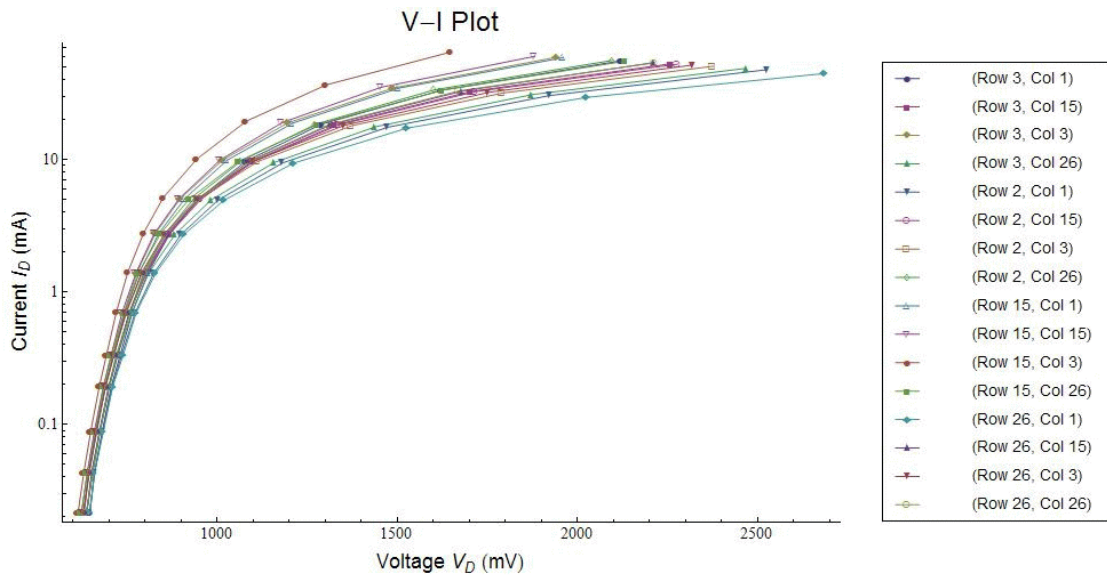
Figure 65   Parasitic resistance test results for Model I array (semilog)
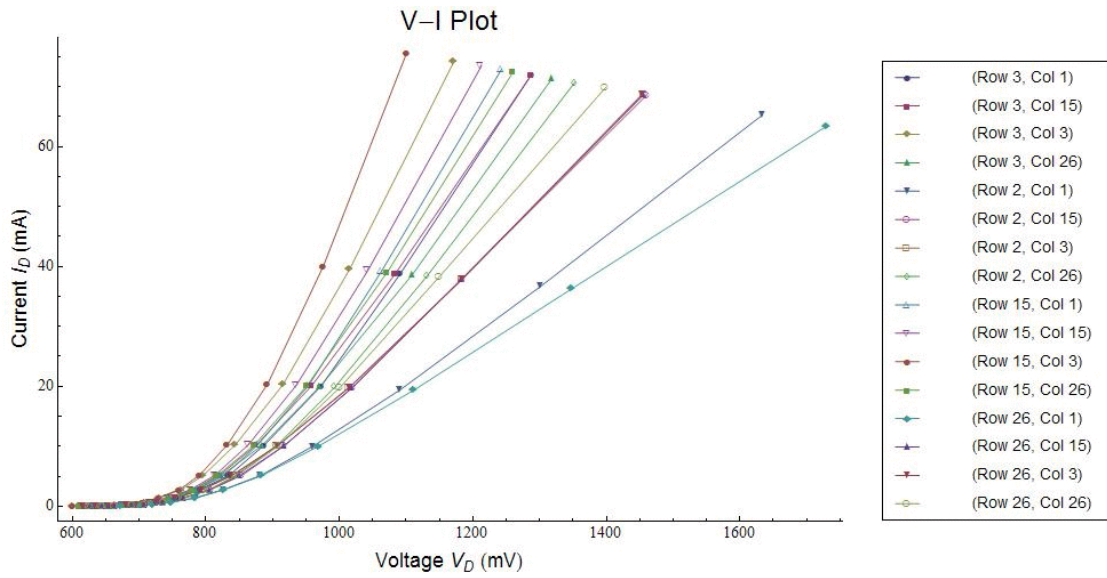
Figure 66   Parasitic resistance test results for Model II array (linear)
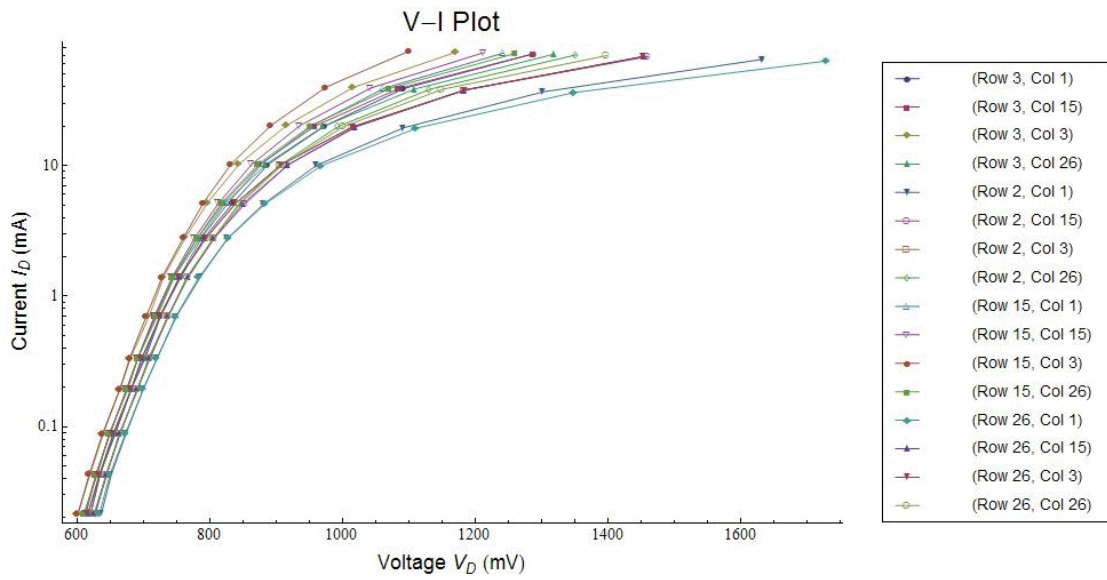
Figure 67   Parasitic resistance test results for Model II array (semilog)

Because the data seem to agree qualitatively with the model of Eq. 28, a non-

linear regression can be performed to test this agreement quantitatively. In order to do so,

however, Eq. 28 must be transformed slightly. First, because the diode current appears on both sides of the equation, solve for V_{pn} to produce Eq. 29:

$$V_D = I_D R_p + \frac{kT}{q} \ln\left(\frac{I_D}{I_S} + 1\right)$$ (29)

Second, because the saturation current is so small ($O[10^{-15}]$), $I_D / I_S \gg 1$, which allows the following simplification:

$$V_D = \alpha_{Is} + I_D R_p + \frac{kT}{q} \ln(I_D) \qquad where \ \alpha_{Is} = -\frac{kT}{q} \ln(I_s)$$ (30)

In Eq 30, α_{Is} is introduced for numerical reasons; because I_S is so small, the non-linear regression routines were unable to determine a satisfactory fit to the data. Using this variable transformation, values for α_{Is} and R_p were determined, and from α_{Is}, the saturation current was then determined. The results of one such regression are shown in Figures 68 and 69. Although 32 of these regressions were performed, only one will be shown graphically to illustrate how closely Eq. 28 fits the data. For the others, the regression coefficients are provided in Tables 70 and 70, after which Tables 18 and 19 report the parasitic resistance and saturation current for the Model I design, while Tables 20 and 21 report these quantities for the Model II design. Note that in Figures 68 and 69, the graphs reflect the diode at position (15,3) in the Model II design. The regression coefficient for this particular diode is the lowest of the 32 tested, at 0.992. Thus all other diodes would show an even closer agreement between regression and raw data. As before, the linear axes show the agreement for high values of current and voltage, while the semilog axes show the agreement for low values.

V–I Plot

Diode at (Row 15, Col 3)
$R_p = 3.83\,\Omega$
$I_0 = 1.17\times10^{-12}$ mA
$r^2 = 0.992$
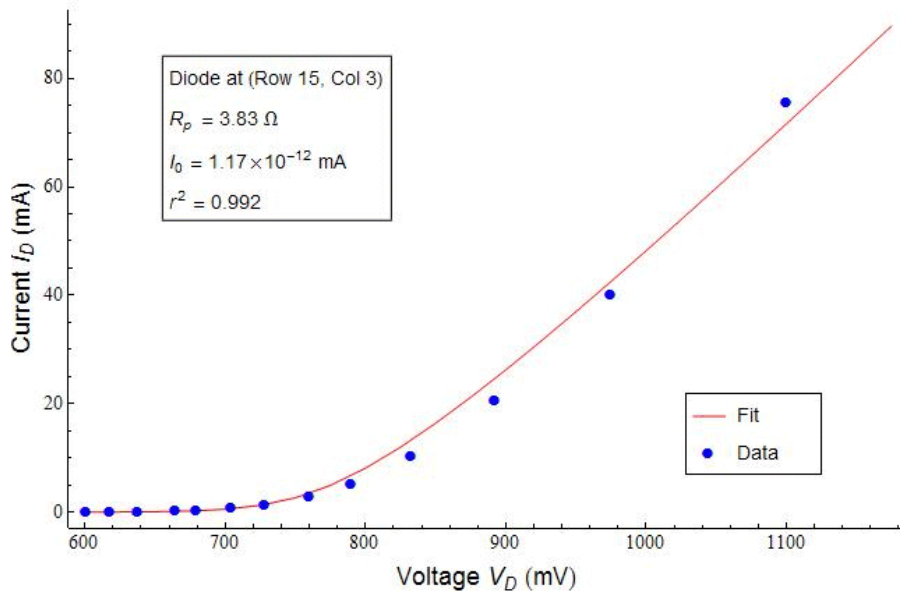
Figure 68   Comparison of parasitic resistance data to regression (linear)

V–I Plot

Diode at (Row 15, Col 3)
$R_p = 3.83\,\Omega$
$I_0 = 1.17\times10^{-12}$ mA
$r^2 = 0.992$
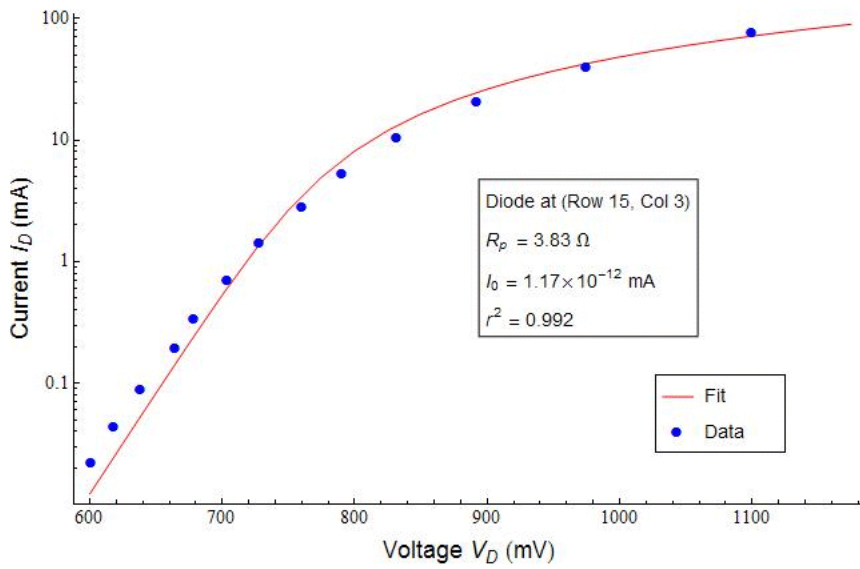
Figure 69   Comparison of parasitic resistance data to regression (semilog)

Table 16   Regression coefficient (r^2) for Model I array

		Columns			
		1	3	15	26
	2	0.999	0.998	0.999	0.998
Rows	3	0.998	1.000	0.999	0.999
	15	0.998	0.997	0.997	0.998
	26	1.000	0.999	0.999	0.999

Table 17   Regression coefficient (r^2) for Model II array

		Columns			
		1	3	15	26
	2	0.996	0.996	0.996	0.993
Rows	3	0.992	0.993	0.994	0.994
	15	0.992	0.992	0.993	0.993
	26	0.998	0.996	0.996	0.995

Table 18   Parasitic resistance R_p (Ω) for Model I array

		Columns			
		1	3	15	26
	2	35.2	30.5	27.2	22.4
Rows	3	22.9	18.8	26.7	33.4
	15	19.2	12.9	17.5	23.7
	26	40.8	28.8	25.4	25.4

Table 19   Saturation current I_S (10^{-15} A) for Model I array

		Columns			
		1	3	15	26
	2	197	479	287	255
	3	182	423	287	276
Rows	15	354	756	445	462
	26	250	466	274	285

Table 20   Parasitic resistance R_p (Ω) for Model II array

		Columns			
		1	3	15	26
	2	12.1	9.20	9.05	7.30
	3	6.39	4.86	6.49	7.01
Rows	15	5.68	3.83	5.33	6.07
	26	13.9	9.15	8.98	8.01

Table 21   Saturation current I_S (10^{-15} A) for Model II array

		Columns			
		1	3	15	26
	2	253	600	392	362
	3	491	1130	730	691
Rows	15	521	1170	729	714
	26	301	590	388	384

Considering the data in Tables 18 and 20, several conclusions can be drawn. First, note the significant decrease in parasitic resistance from the Model I design to the Model II design, indicating that the steps taken to reduce the on-chip resistances successfully achieved their goal. Also, note the relatively broad range of resistances for both designs; $12.9 - 40.8 \ \Omega$ for the Model I array and $3.83 - 13.9 \ \Omega$ for the Model II array. These broad ranges are consistent with the preliminary conclusions drawn from Figures 64 and 66 that there would be a span of parasitic resistances. It is also worth noting that the positions of the diodes at each end of the range is the same as well; diode (15,3) shows the lowest resistance, while diode (1,26) shows the highest. Because the same pattern on row and column leads was used for both designs, this reinforces the conclusion that the metal traces dominate the parasitic resistance.

Next, consider the data in Tables 19 and 21. The two array designs used different designs for the p-n junction itself, so it is not surprising that the saturation current should be different between the two designs. The degree to which they vary within the same design, however, is somewhat more surprising. In the Model I array, the saturation current varies from 189 to 756 fA, while in the Model II array, it varies from 491 to 1170 fA. This is a substantial variation, but it may be explained as a numerical artifact. Because of the variable transformation, small differences in the regression parameter $\alpha_{Is,}$ are magnified exponentially when determining I_S. Considered in this light, the fact that the values vary by only a factor or 3 or 4 is actually quite impressive.

The success of Eq. 28 in representing the test data has another important consequence. If the parasitic resistance test were repeated over the entire array to identify

121

the resistance associated with each diode, it would be possible to separate the portion of the voltage drop associated with the p-n junction from the portion associated with the ohmic resistance. Such a test could not be performed using the present interface board; each diode must be tested individually at a range of temperatures and sensing currents.

Natural Convection Tests

The final set of diode characterization tests were the natural convection tests. The purpose of these tests were two-fold: to identify "bad" diodes and to verify the substrate conduction losses predicted by the COMSOL modeling.

The test itself was fairly simple. The test chamber was filled with FC-72 such that the chamber thermocouple was completely immersed at a depth of approximately 1 cm. The chamber was covered to reduce evaporative losses and then mounted in the test rig. The power supply was turned on, and the system was allowed to heat up. After several minutes, the DC offset was tuned to ensure an appropriate data collection range. Each test run collected data for 3 s at 100 Hz, after which the heater was immediately turned off. The process was repeated for each of the power dissipations listed in Table 22. As can be seen, seven tests were planned, however during test 7, at a heater dissipation of 32 W/cm^2, the surface superheat was sufficient to initiate boiling, so this test is excluded from the following analysis.

Table 22   Natural convection test matrix

Test number	1	2	3	4	5	6	7
Heat Flux (W/cm^2)	1	2	4	8	16	24	32
Heater Voltage (V)	4.49	6.35	8.97	8.69	17.94	21.98	

Because the first objective of these tests was to identify so-called "bad" diodes, the first task is to define what makes a diode "bad." In practice, this identification is as much an art as it is a science. The object is to strike a balance between the positive action of eliminating "obviously malfunctioning" sensors and the negative action of arbitrarily discarding operational
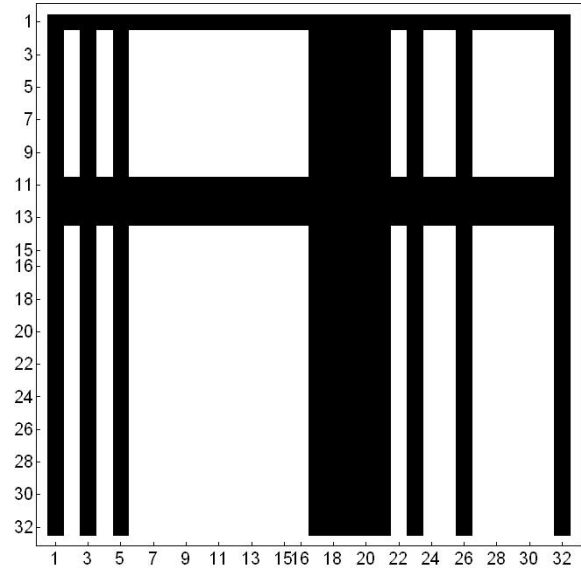
Figure 70   Overall set of excluded diodes

sensors that report an unexpected value due to ordinary random fluctuations in the measured value or misunderstanding what results ought to be expected. A two-stage process was developed to ensure that suspicious diode measurements were duly considered before being discarded. The black regions in Figure 70 indicate diodes that were discarded — a total of 520 diodes were discarded, leaving 504 viable diodes. Figure 71 shows the resulting natural convection results test for the 24 W/cm^2 heat flux.

123
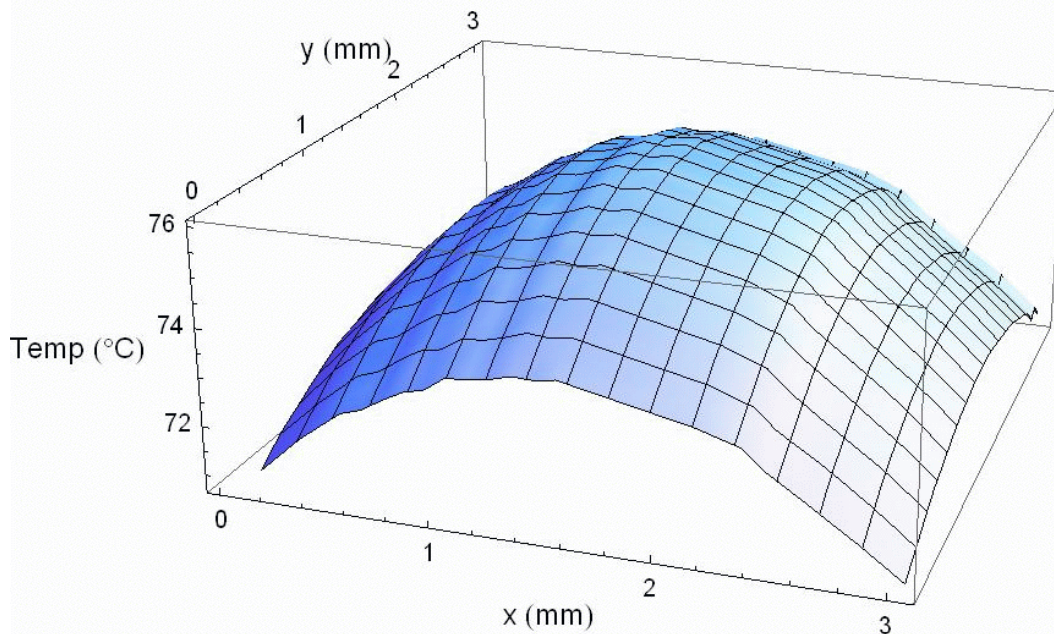
Figure 71   Final temperature distribution, 24 W/cm^2

The second objective of the natural convection tests was to validate the substrate

conduction losses in the 3-D conduction solver. Figures 72 – 74 show the comparison

between the measurements and the results of the 3-D conduction solver calculations for

several test cases. In each case, the shapes of the profiles qualitatively agree fairly well,

especially for the middle heat fluxes. Additionally, numerical comparisons are provided

in Table 23. For most cases, the data and the calculations agree to within $1 - 2$ °C. At

the low heat fluxes in particular, this suggests an offset error of some kind. As the

surface heat flux increases, the absolute magnitude of the discrepancy remains within the

$1 - 2$ °C range, which has the effect of decreasing the relative error when compared to the

overall temperature rise over ambient — decreasing the relative error to only 3% for test

5 (16 W/cm^2). The final test shows the largest discrepancy, at 3.4 °C rms, however,

because of the large temperature difference between the surface and ambient, this still

corresponds to only about 7% error.
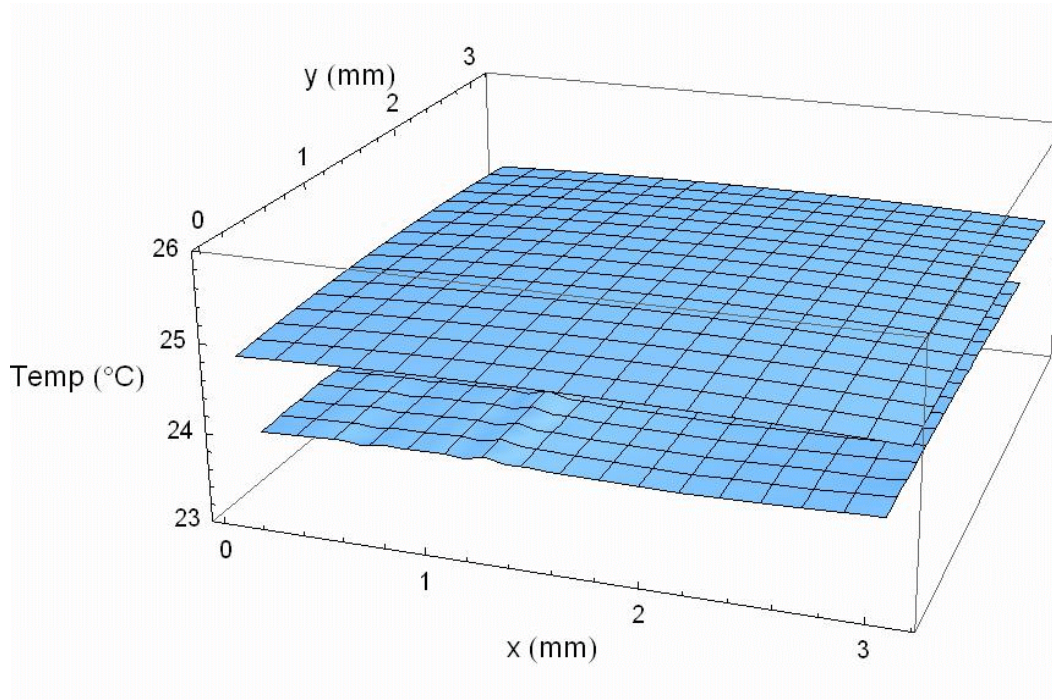
Figure 72   Comparison to calculated temperatures, 1 W/cm^2
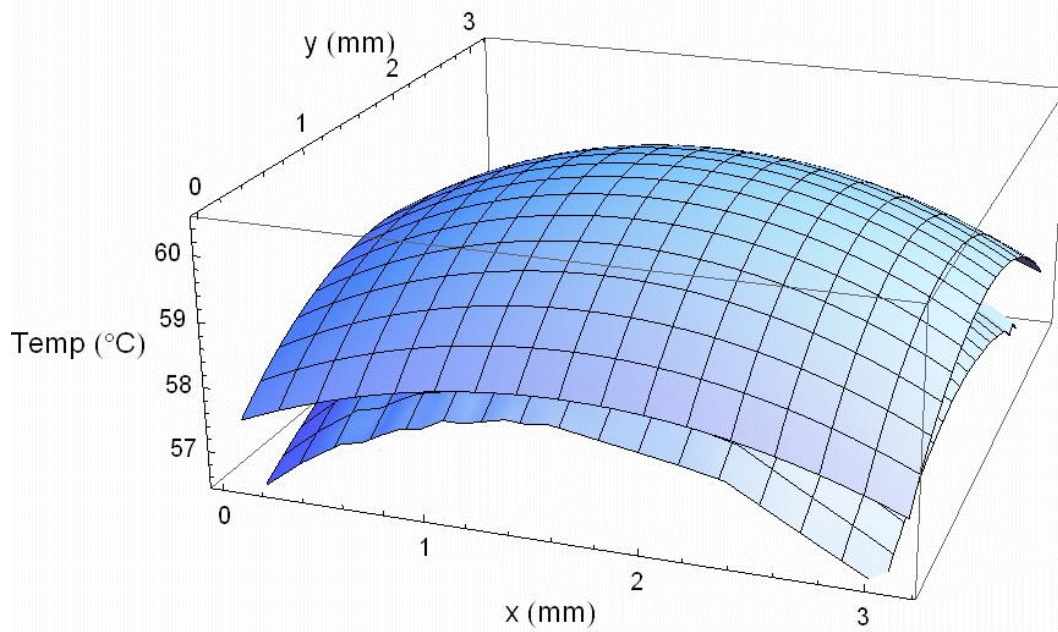
Figure 73   Comparison to calculated temperatures, 16 W/cm^2
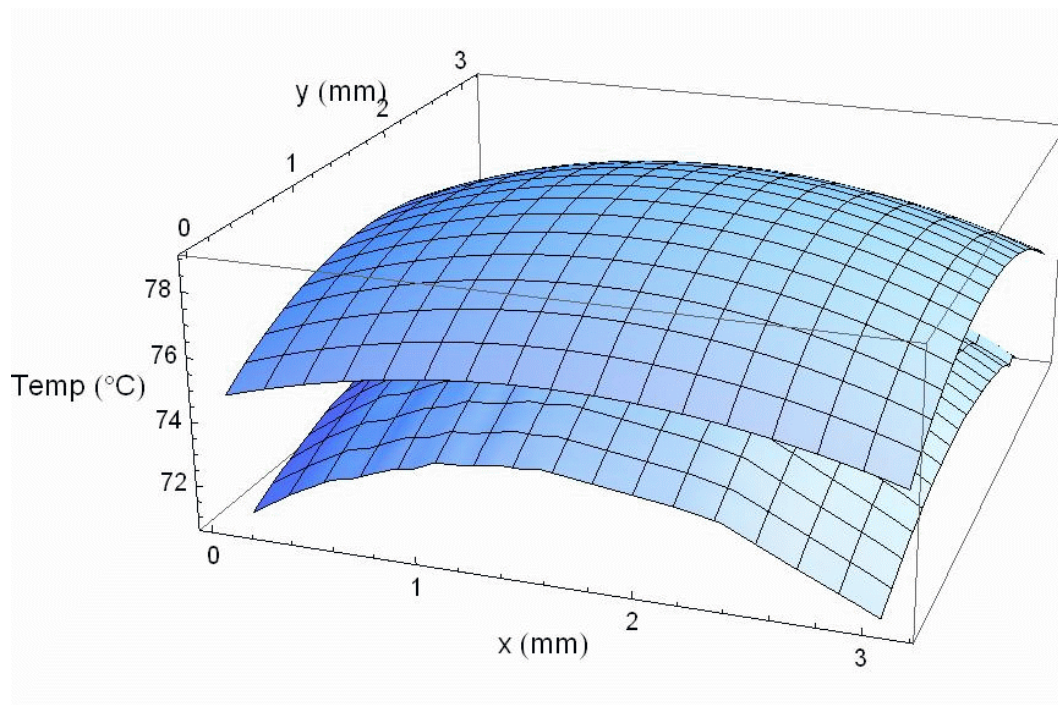
Figure 74   Comparison to calculated temperatures, 24 W/cm^2

Table 23   Comparison between numerical result and measured values for natural convection

Test	T_∞ (°C)	Avg T_{meas} (°C)	ΔT (°C)	$\text{Max}(|T_{meas} - T_{calc}|)$ (°C)	% of ΔT (%)	$\text{Mean}((T_{meas} - T_{calc})^2)^{\frac{1}{2}}$ (°C)	% of ΔT (%)
1	23.4	24.0	0.6	0.954	159	0.874	146
2	23.4	26.2	2.8	1.89	67.5	1.80	64.3
3	23.4	31.2	7.8	1.85	23.7	1.69	21.7
4	23.7	40.6	16.9	1.56	9.23	1.26	7.46
5	24.2	58.2	34.0	1.72	5.06	1.01	2.97
6	24.9	74.0	49.1	4.80	9.78	3.40	6.92

Summary

This chapter reported the results of the five sets of characterization tests. The first two tests investigated the temperature sensitivity of the diode array. The single-diode calibration confirmed the expected 2 mV/°C temperature sensitivity and also demonstrated that the sensitivity decreased slightly as the sensing current increased. The full-array calibration established the working parameters for each diode in the array; the temperature sensitivity determined by this test was lower than in the single-diode calibration. The reason for this is not clear, but may be related to temperature-induced changes in the parasitic resistance. Investigating this effect was not possible with the existing interface board, and because the effect is consistent across several calibration runs, this line of inquiry was not pursued further.

The next two tests characterized differences from ideal diode behavior. The transient response test demonstrated that reverse recovery time for the diodes is approximately 6 µs. As a result of this delay, the diode array is limited to a theoretical maximum scanning rate of 5.2 kHz. Using the data acquisition equipment described in Chapter 4, the target scanning rate of 1 kHz is achievable, but the measurements reported by the first seven rows of diodes will be compromised; alternately, the scanning rate can be decreased to 100 Hz, and only the first row's measurements will be compromised. The parasitic resistance test demonstrated that the modifications made in the Model II design significantly decreased the ohmic resistance associated with the diodes, from a typical value of about 25 Ω in Model I to only about 7 Ω in Model II. More importantly, the parasitic resistance test provides a way to isolate the voltage drop produced by the p-n junction; if the test were performed for each diode in the array, this should correct the loss in sensitivity observed in the full-array calibration.

The natural convection test identified 520 diodes that reported faulty results, leaving 504 valid diodes in the array. The comparison between the measured surface temperatures and the 3-D conduction solver predictions was reasonably good — within 10% at the higher heat fluxes — suggesting that the substrate conduction loss coefficients predicted using the COMSOL model in Chapter 5 are sufficiently accurate for the purposes of the present work.

Chapter 7: Jet Impingement Experiment

Experimental Setup

In order to test the capability of the diode array, it should be used to make measurements of some phenomenon that produces a varying surface temperature distribution, preferably one that does so by sharply varying the local heat transfer coefficient in a predictable manner. An excellent candidate for this phenomenon is jet impingement, because it produces a high heat transfer coefficient near the point of impingement, and the coefficient decreases markedly away from this point. The heat transfer coefficient can vary by a factor of 5 or more between the point of impingement and the wall jet, which was expected to be sufficient to demonstrate the array capability.

The array's small size posed significant problems for the experimental design, however. Assuming that the jet strikes the center of the array, the maximum range at which a measurement can be taken is only about 1.6 mm. Because the heat transfer coefficient experiences almost its full range of variation over a distance $r/D \approx 5 - 8$, the largest desirable nozzle is in the range $0.2 - 0.3$ mm. At the same time, a smaller nozzle requires a higher exit velocity to achieve the same Reynolds number, which then increases the pumping power requirement. In the end, a 26-gauge (0.241 mm ID), blunt end hypodermic needle was selected for the nozzle.

Positioning the nozzle accurately was another problem exacerbated by the small scale. For a relatively large heater (several cm across), a positional error of 0.5 mm can

be tolerated; when the heater surface is only 3.2 mm across, such an error is catastrophic. This was resolved by using a 3-Axis Linear Translation stage (Line Tool, Co.; Model A RH) to position the nozzle; each of the three axes is controlled by a micrometer actuator, providing positional accuracy of 0.0254 mm. This assembly is shown in Figure 75.
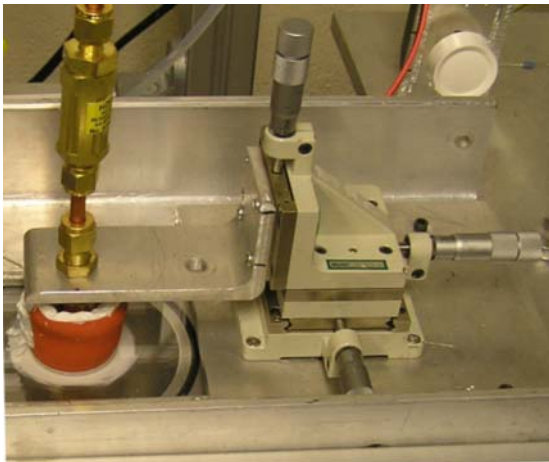
Figure 75   3-axis positioning assembly

As can be seen in Figure 76, there were no markings on the chip visible from outside the chamber that could be used as accurate reference marks for positioning the needle (at the time the diode array and packaging were being specified, this problem was not considered, and adding the marks
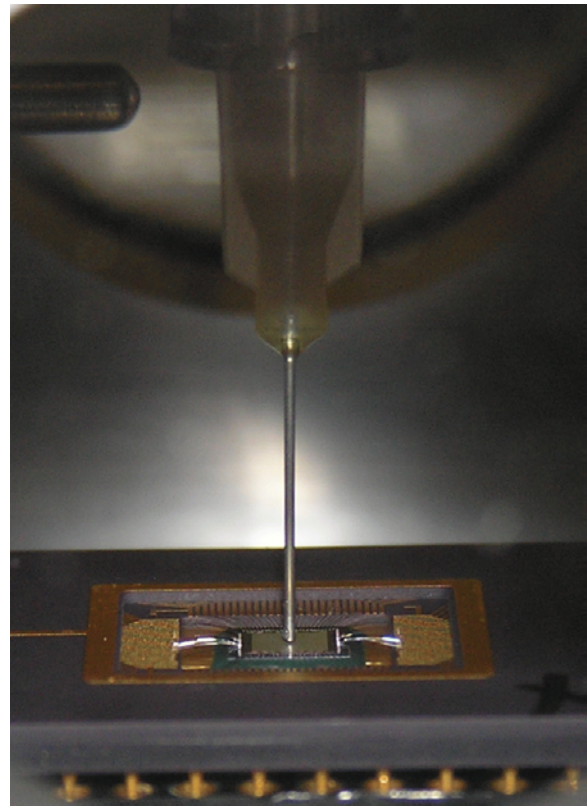
Figure 76   Positioning the needle over the surface

after the fact was not practical because of the high precision and risk of damage to the chip). Therefore, although the positional uncertainty was only $\pm$ 12.7 μm with respect to the commanded location, the positional uncertainty in the commanded location with respect to the center of the array is more difficult to quantify.
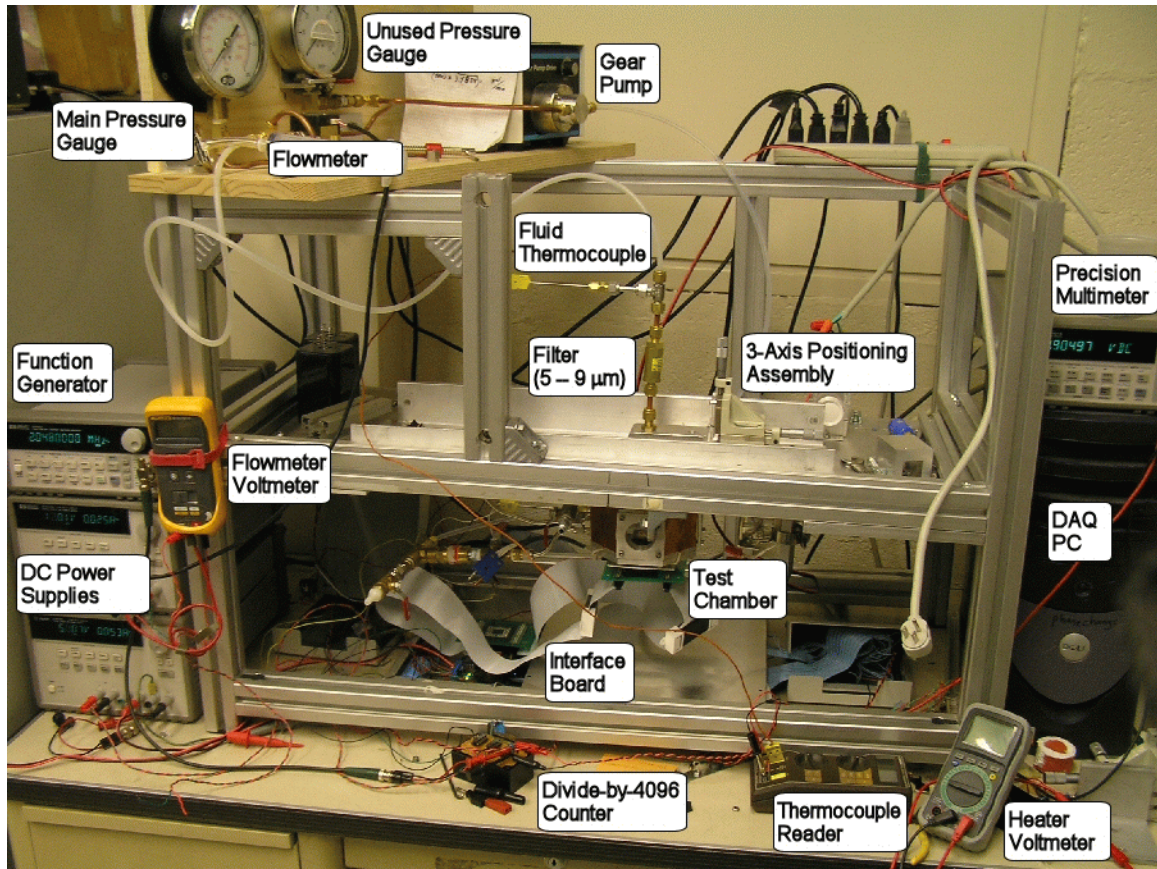
Figure 77   Jet impingement test setup

The overall jet impingement test setup is shown in Figure 77. In addition to the

nozzle and positioning stage already discussed, the set up includes:

- A 5-9 μm filter.

- An Omega FLR-1000-BR; this meter is rated for liquid flow rates up to 500

  ml/min. This was monitored by the data acquisition system, as well as by a Fluke

  12 Multimeter

- A Cole-Parmer 75211-10 Gear Pump, with pump head 07002-14. The

  pump/pump head combination is rated to deliver 4.6 – 460 ml/min, at a maximum

  pressure of 300 psi (2070 kPa).

- Two bourdon-type pressure gauges, one rated for 0-300 psi, and the other rated for a smaller range; this gauge was isolated from the rest of the system to keep from being damaged.

- A standard type K thermocouple, inserted into the flow just upstream of the filter, and read using an Omega 871A Digital Thermometer

A schematic of the test setup is shown in Figure 78.
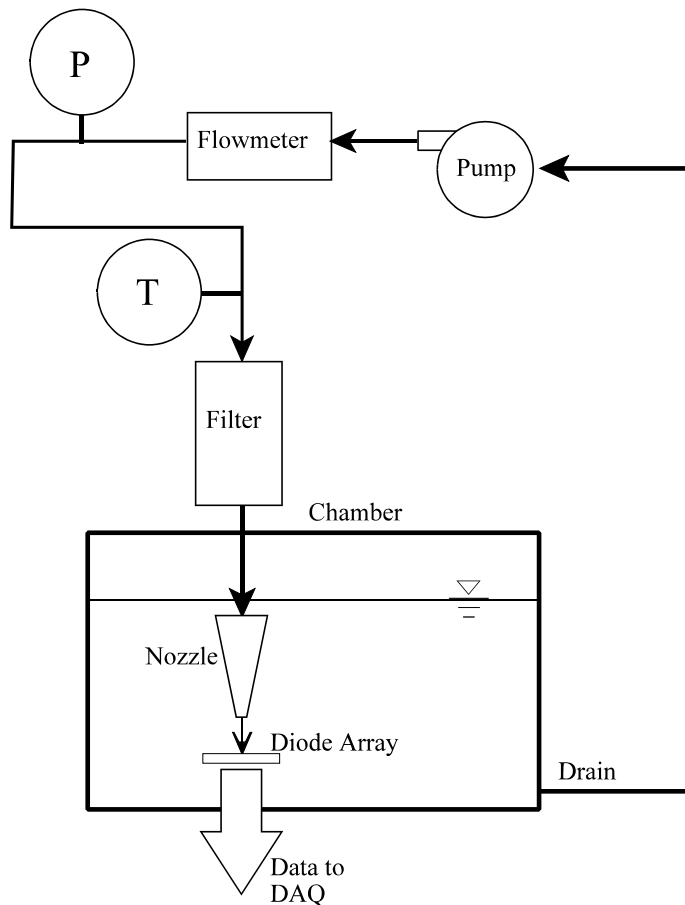
Figure 78   Schematic of jet impingement test setup

Test Conditions

There were three independent variables: heater voltage, nozzle stand-off distance, and nozzle velocity. Taking two values for each produced eight permutations, enumerated in Table 24; this table also reports several relevant derived quantities – the heat flux produced by the heaters and the jet Reynolds number, as well as the measured jet temperature.

Table 24   Jet impingement test matrix

Test	V_{heater} (V)	z/D_n	v_{jet} (m/s)	q_{test} (W/cm²)	Re_{Dn}	T_{fluid} (°C)	Test Notation
1	20.00	6	11.5	19.89	7320	24.5	q- v- z-
2	35.00	6	11.7	60.97	7400	24.6	q+ v- z-
3	20.00	6	26.9	19.91	17,500	24.3	q- v+ z-
4	35.00	6	27.9	60.93	17,700	24.9	q+ v+ z-
5	20.00	10	12.6	19.87	7970	25.0	q- v- z+
6	35.00	10	12.4	60.96	7880	25.2	q+ v- z+
7	20.00	10	28.1	19.95	17,800	25.7	q- v+ z+
8	35.00	10	29.5	60.89	18,800	25.9	q+ v+ z+

The measured surface temperature distributions for each test (excluding the bad diodes identified in Chapter 7) are shown in Figures 79 – 86.
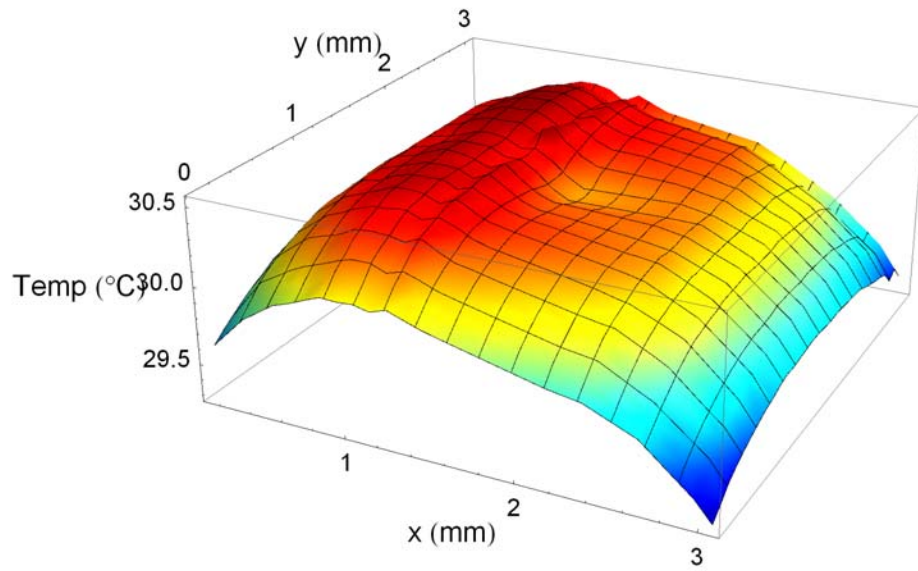
Figure 79   Jet impingement test results, case 1
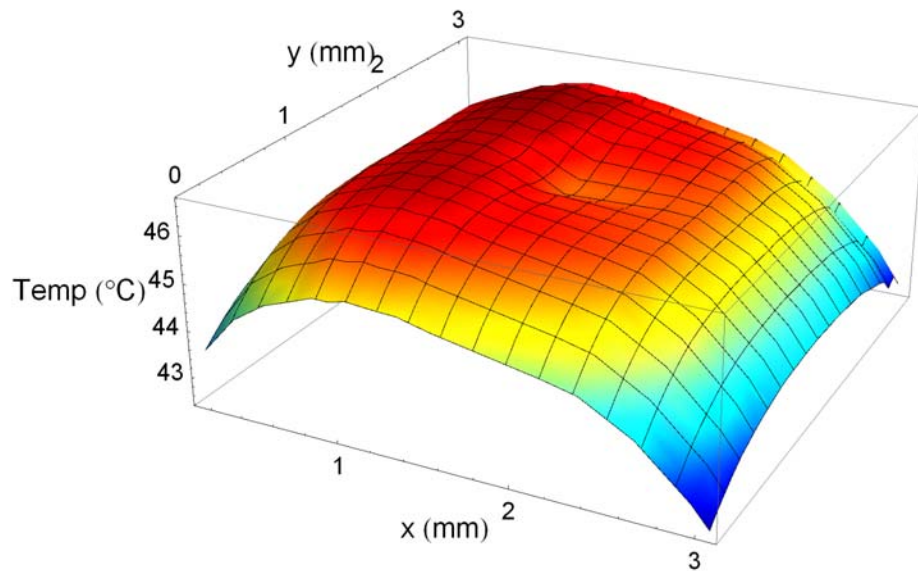
Figure 80   Jet impingement test results, case 2
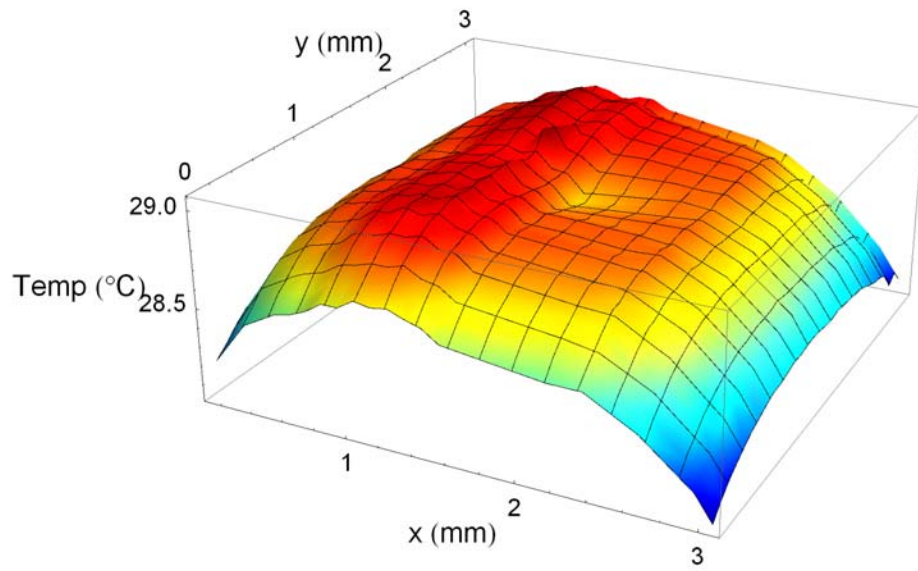
Figure 81   Jet impingement test results, case 3
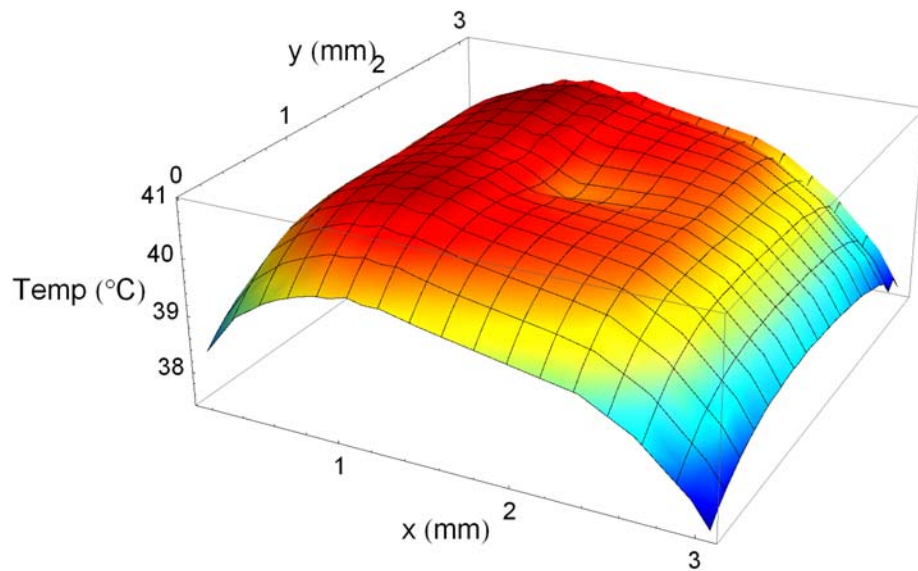
Figure 82   Jet impingement test results, case 4
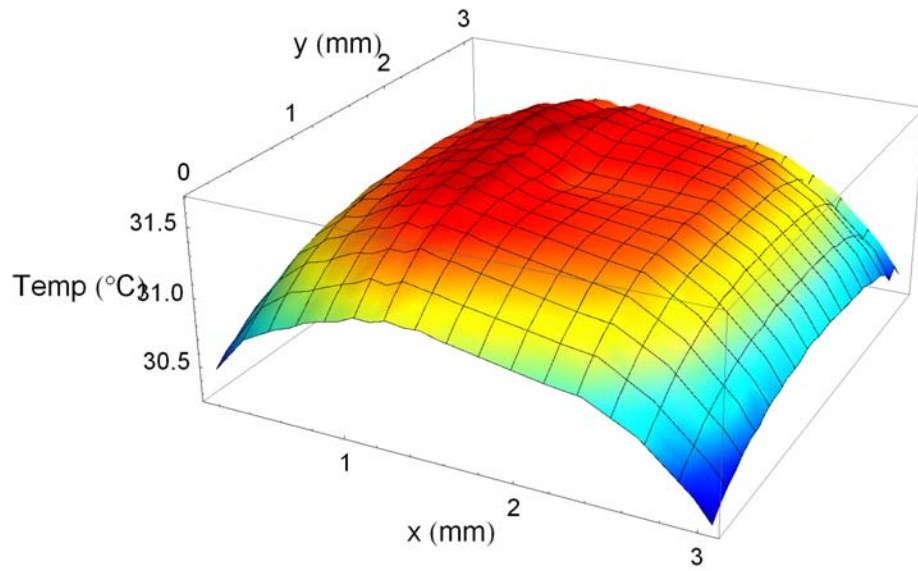
Figure 83   Jet impingement test results, case 5
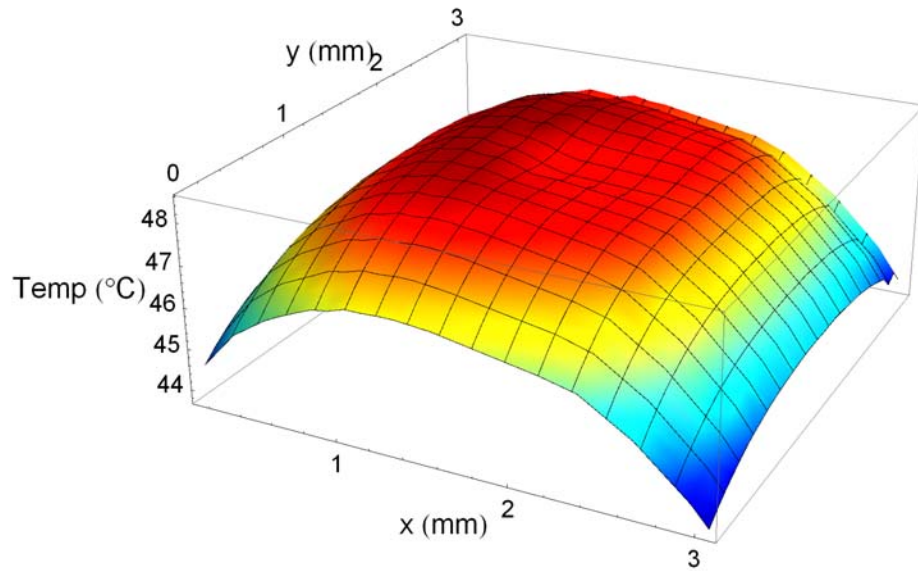
Figure 84   Jet impingement test results, case 6
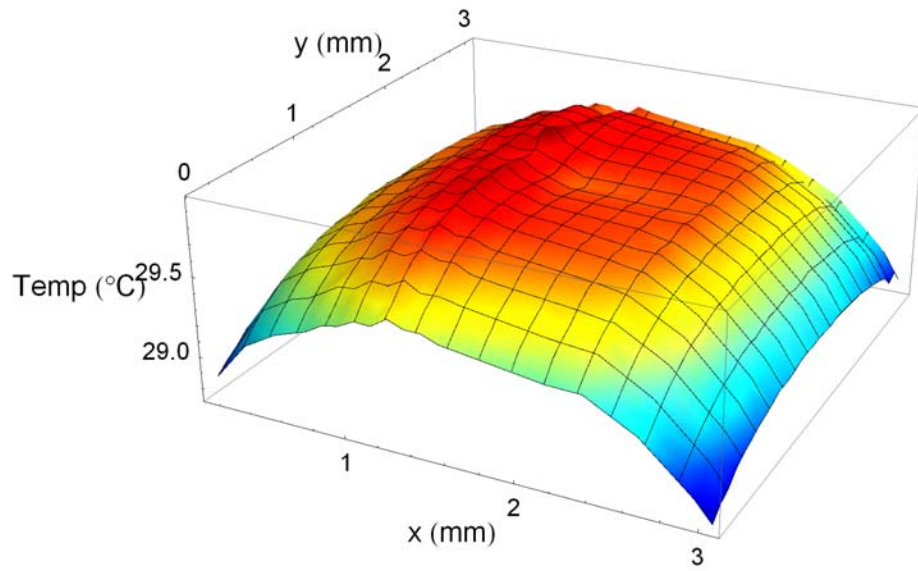
Figure 85   Jet impingement test results, case 7
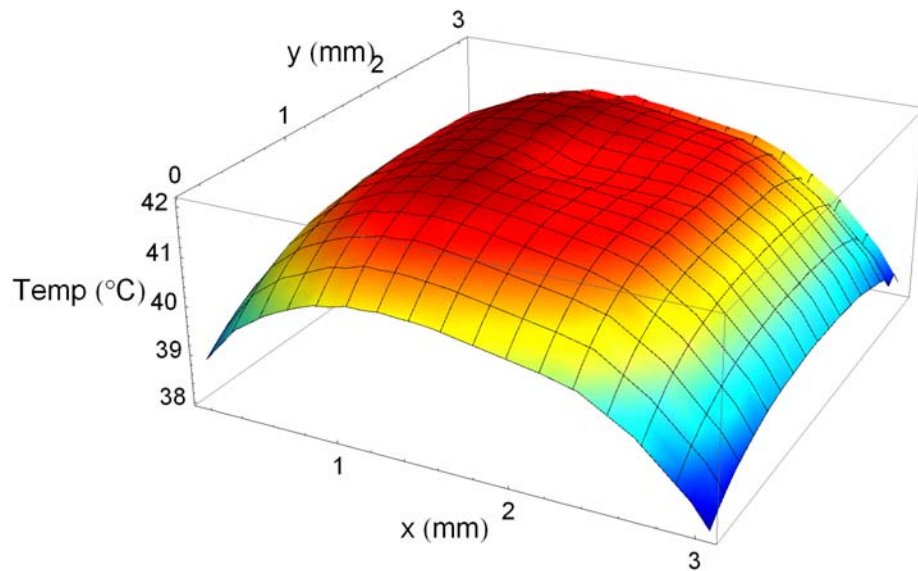
Figure 86   Jet impingement test results, case 8

137

Jet Impingement Test Results – Discussion

Qualitatively, these results correspond well to their expected behavior. Each distribution has the same basic domed shape, similar to what was observed in the natural convection tests. This suggests that the heat transfer coefficient remains fairly constant over much of the surface; this is consistent with the expected behavior in the wall jet region. Unlike the natural convection profiles, however, each of the jet impingement profiles has a dimple near the apex of the dome (or if not a dimple, the peak of the dome is at least somewhat flattened); this is a consequence of the very high local heat transfer coefficients in and around the stagnation region.

The observed changes in the temperature distribution throughout each of the tests also match expectations. First, consider the pairs of tests in which the heat flux is increased, while the nozzle stand-off and the jet velocity remain constant (tests 1 and 2, 3 and 4, 5 and 6, and 7 and 8). In each such case, the higher heat flux is associated with a significantly higher surface temperature. Also, in each such pair of tests, the shape of the temperature distribution does not change significantly – the dimple in the center closely maintains its diameter and shape; this is to be expected as well, because the shape of the distribution is determined by the jet characteristics, which have not changed. Next, consider those tests in which the nozzle velocity is increased, while maintaining the same heat flux and nozzle spacing (tests 1 and 3, 2 and 4, 5 and 7, and 6 and 8). The increase in velocity causes an increase in the heat transfer coefficient, which should produce a decrease in the surface temperature; this too matches the observations. Finally, consider

138

the tests in which the nozzle spacing is increased, while holding the heat flux and nozzle velocity constant (tests 1 and 5, 2 and 6, 3 and 7, and 4 and 8). The increase in spacing decreases the heat transfer coefficient, which should produce an increase in the surface temperature; again, the observations follow this trend. For these tests, also notice that the shape of the distribution changes slightly; the dimple increases in diameter and also becomes somewhat shallower. This is also consistent with the increased stand-off distance; the larger spacing allows the submerged jet to entrain additional fluid before striking the surface, so the jet will be broader and slower at the impingement point.

As a final qualitative comparison, consider the test cases at the two extremes of jet behavior. One would expect the highest overall surface temperatures to be associated with the test case with the largest heat flux, smallest jet velocity, and largest stand-off distance. These are the conditions in test 6, which does show the highest surface temperatures. Conversely, the lowest surface temperatures should be associated with the smallest heat flux, largest jet velocity, and smallest stand-off distance. These are the conditions in test 3, which does show the smallest temperature surface temperatures.

Jet Impingement Test Results – Analysis

Although these observations are encouraging, the question of the diode array's quantitative accuracy still remains. To answer this question, the temperature measurements were used to determine the local heat transfer coefficients for each test case, and these values were compared to the values predicted using three correlations available in the literature.

Nozzle Location

139

Before any quantitative analysis can begin, there is still one experimental parameter that has not been determined: the nozzle position. As discussed previously, because there are no distinct markings denoting the boundaries of the diode array, it is difficult to determine the nozzle position relative to the temperature distribution a priori. Because the correlations are presented in terms of an axisymmetric distribution about the point of impingement, its location is a matter of some interest. Fortunately, the temperature distribution provides the necessary clue to determining its location a posteriori. Because the dimple should correspond to the location with the highest heat transfer rate, the center of the should correspond to the nozzle location. This conclusion is reinforced by the fact that the dimple location remains the same for each test. This technique places the location of the nozzle at the (x,y) coordinates (1.7,1.6) mm; very close to the center of the array, after all.

Correlation Selection

For comparison purposes, three correlations were selected from the literature. Five criteria were considered while reviewing the literature:

1. The correlation must be for a single, round nozzle.

2. The correlation must be for a submerged jet.

3. The correlation must be for single phase jet impingement.

4. The correlation must incorporate a radial dependence.

5. The correlation must be closed form.

The reasons for the first three criteria are obvious; the correlations should approximate the test conditions as closely as possible. The fourth criterion follows from the goal of

the test: because the objective is to demonstrate the diode array's ability to determine the heat transfer coefficient distribution, the correlation should provide a spatial variation for comparison. Finally, the fifth criterion simplifies the comparisons by excluding papers that report only raw data or that report a graphical correlation. Of the papers reviewed, only two satisfied all five criteria.

Sun, et al.

The first paper, by Sun, et al. [37], offers two correlations for the local Nusselt number. In their experiments, they studied a deionized water jet from a 0.987 mm nozzle. They reported their results in three parts, describing separately the stagnation point heat transfer, the effect of stand-off distance, and the radial distribution. In fact, they provide two expressions each for the stagnation point heat transfer and the radial distribution. Combining their expressions yields Eqs. 31 and 32:

$$Nu = 1.02\,\mathrm{Pr}^{0.368}\,\mathrm{Re}^{0.5}\sqrt{\frac{5}{z/D}}\left(1 + 0.46\left(\frac{r}{D}\right)^{1.94}\right)^{-0.51} \tag{31}$$

$$Nu = 0.9553\,\mathrm{Pr}^{0.4}\,\mathrm{Re}^{0.5}\sqrt{\frac{5}{z/D}}\times$$
$$\left(\left(\left(\frac{Tan^{-1}\left(0.88\,r/D\right)}{r/D}\right)^{0.5}\right)^{-17} + \left(1.69\left(\frac{r}{D}\right)^{-1.07}\right)^{-17}\right)^{-1/17} \tag{32}$$

The data presented this paper (on which these correlations are based) cover the following ranges:

141

$5000 < Re < 36,000$

$1 < z/D < 20$

$0 < r/D < 14$

Hofmann, et al.

The second paper, by Hofmann, et al. [18], provides a third correlation. In their experiments, they studied an air jet from a 25 mm nozzle. Their correlation is given in Eq. 33:

$$Nu_{local} = 0.055 \left[Re^3 + 10\,Re^2 \right]^{0.25} Pr^{0.42} \exp\left(-0.025(r/D)^2 \right) \qquad \textbf{(33)}$$

They state that this correlation is valid for:

$14,000 < Re < 230,000$

$0.5 < z/D < 10$

$0 < r/D < 8$

Because the working fluid in their experiments was air, there is a possibility that compressibility effects may be present; these effects would certainly be absent from the jets studied in the present work. The Mach number, defined in Eq. 34, can be used to gauge the significance of compressibility effects.

$$M = \frac{v_{jet}}{c} \qquad \textbf{(34)}$$

In air at 30 °C (as specified in paper), the acoustic velocity, $c = 343$ m/s. Because compressibility effects begin to become relevant at a Mach number $M = 0.3$, this places an upper limit on the jet velocities of $v_{jet,max} = 103$ m/s if compressibility effects are to be

neglected. Knowing the nozzle diameter and fluid temperature, the range of jet velocities in their experiments can be determined; the range of Reynolds numbers reported in the paper corresponds to a range of jet velocities 8.84 m/s < v_{jet} < 145 m/s. Thus, at the upper limits of the Reynolds number, compressibility effects may indeed be present in their data. Using the value of $v_{jet,max}$ determined above, the limiting Reynolds number is approximately 163,000. In the present work however, the Reynolds numbers are far below this limit, and it is not likely that compressibility effects are relevant.

A second concern with this correlation pertains to the absence of an explicit dependence on nozzle stand-off distance. Although the authors acknowledge the effect of nozzle stand-off distance on heat transfer, they conclude that the effect is too complex to be included in a simple correlation and they neglect it. Comparing their expression to the data they report in the paper, it seems that for the lower range of Reynolds numbers their correlation produces estimates for the Nusselt number that tend to correspond to their data for large nozzle stand-off distances. As the Reynolds number increases, the estimates tend to correspond to shorter stand-off distances. Note that these observations are not explicitly reinforced by statements from the paper's authors; these are conclusions drawn from comparisons between their figures and their correlation.

Martin

Because the earlier work by Martin [8] provides only an average heat transfer coefficient, it does not, strictly speaking, meet the fourth criterion. However, his correlation is well established and considered standard within the heat transfer

community, so it will also be used for comparison. Martin's average Nusselt number correlation is given by Eq. 35:

$$\overline{Nu} = 2\left(\mathrm{Re}\left(1 + \frac{\mathrm{Re}^{0.55}}{200}\right)\right)^{0.5} \mathrm{Pr}^{0.42} \frac{D}{r} \frac{1 - 1.1(D/r)}{1 + 0.1(z/D - 6)(D/r)} \quad (35)$$

Martin states that this correlation is valid for:

$2000 \le \mathrm{Re} \le 400{,}000$

$2 \le z/D \le 12$

$2.5 \le r/D \le 7.5$

Interestingly, Hofmann, et al. [18] describe a technique for differentiating Eq. 35 with respect to r and thereby recovering the radial dependence. Following their procedure yields Eq. 36:

$$Nu = 10\left(\mathrm{Re}\left(1 + \frac{\mathrm{Re}^{0.55}}{200}\right)\right)^{0.5} \mathrm{Pr}^{0.42} \frac{10(r/D) + 2(z/D) - 12 - 1.1(z/D - 6)}{\left(10(r/D) + (z/D) - 6\right)^2} \quad (36)$$

This expression differs slightly from the one reported in [18] — the last term in the numerator is $1.1(z/D + 6)$ in the paper — however, this form better reproduces the corresponding figure in the paper and is believed to be correct. Because Eq. 35 is restricted to $r/D \ge 2.5$, Eq. 36 is also limited to $r/D \ge 2.5$. Martin [8] provides a graphical correlation applicable for $r/D < 2.5$, which could conceivably be used to extend Eq. 36 for lower r/D, however given the availability of Eqs. 31, 32, and 33, each of which is valid all the way to $r/D = 0$, this does not seem necessary.

Additional Working Fluid Concerns

As noted above, only the two papers — Sun, et al. [37] and Hofmann, et al. [18] — satisfied all five criteria used in selecting a correlation to compare the experimental data collected in the present work. Neither of these papers (nor the earlier work by Martin [8]) used FC-72 as the working fluid; Sun, et al. used deionized water, while Hofmann, et al. and Martin both used air. Despite the different working fluids, the correlations reported in these papers can still be used to make predictions for the present work because each of these correlations incorporates an explicit Prandtl number dependence. The Prandtl number is a similarity parameter which allows the generalization of results from one experiment to other, geometrically similar experiments conducted under other conditions [7]. Therefore, despite the difference in fluid properties between air, water, and FC-72, correlations obtained using one fluid can still be applied to other fluids, provided the appropriate Prandtl number value is used. It is worth noting that none of the papers reviewed used FC-72 as the working fluid. The majority of the papers used air as the working fluid, followed by water as the next most common working fluid. Two papers, Womac, et al. [35] and Li and Garimella [39] used FC-77, while Zhou and Ma [86] used R-113. Table 25 reports the Prandtl number values for these various fluids.

Table 25   Prandtl number for various fluids

	Air	Water	FC-72	FC-77	R-113
Prandtl Number	0.707	5.83	12.8	25	8.53

Local Heat Transfer Coefficients

145

The following analysis procedure was used to determine the heat transfer coefficients. First, the boundary conditions for the 3-D conduction solver were determined from the experimental parameters and data. Next the local heat transfer coefficients over the surface were determined from the 3-D conduction solver results. Finally, the radial distribution of these local coefficients was determined, and the results compared against the correlations.

The first task was to determine the boundary conditions. For the top surface, there were three regions to consider, as indicated by Figure 87. Dirichlet conditions were assumed for the diode array region itself; this required a specified temperature distribution. Ideally, of course, the temperature measurements would be used directly over the entire region; because many of the measurements had to be discarded, this was not possible. Instead, the temperatures at the discarded locations were determined by interpolation, producing a 32 x 32 temperature array.

Figure 87   Regions on top surface

Additionally, the ambient fluid temperature was subtracted from each value to determine the local temperature rise, and these values were specified over the diode array. Over the remaining two regions — the heaters and the outer surface — Neumann conditions were assumed, which required a specified heat flux and/or a specified heat transfer coefficient.

146

In these regions an average heat transfer coefficient was assumed, determined by averaging the three correlations according to Eq. 37.

$$\bar{h}_{surf} = \frac{1}{A_{top} - A_{array}} \left(\int_{A_{top}} \frac{k}{D} Nu_{local} dA - \int_{A_{array}} \frac{k}{D} Nu_{local} dA \right) \tag{37}$$

The three correlations did not each produce the same average coefficient, of course, but the results of the calculations were used to select a value that would approximate the local conditions. This value was applied over both the heater regions and the outer surface region; because the heaters themselves extended past the top and bottom boundaries of the diode array, these regions also required that a surface heat flux be specified. This was simply taken to be the heater dissipation. For the sides and back surfaces, the substrate conduction coefficients were used, as discussed in Chapter 5. One final note concerns the ambient temperature; because the temperatures in the diode array region were specified as the increase over ambient, the ambient temperature was referenced to 0 °C.
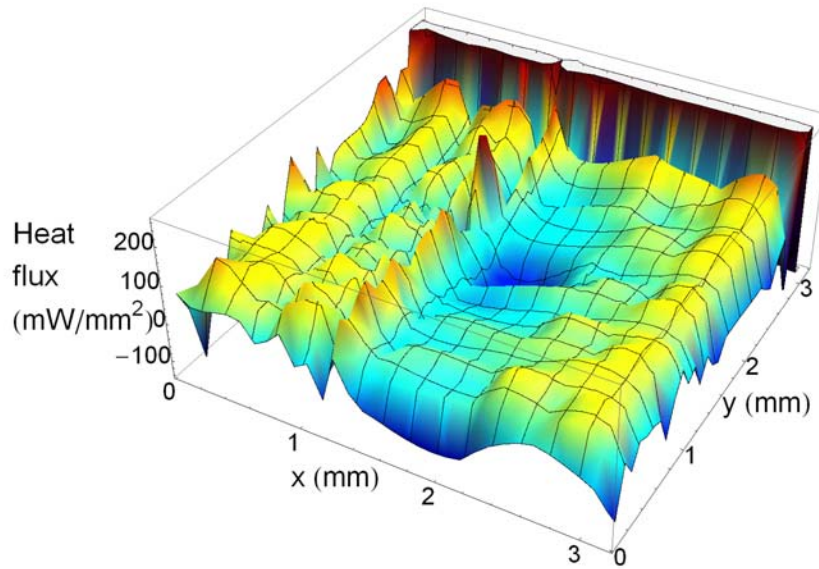
Figure 89   3-D conduction solver results for the substrate conduction

With the boundary conditions determined, the next step was to execute the 3-D

conduction solver. Figure 88 shows the top surface temperature distribution, as computed

by the solver for the conditions of Test #1; note the close correspondence to Figure 79, in

particular the small ridge running in the y-direction just to the left of the dimple. Next,

consider Figure 89, which shows the substrate conduction necessary to maintain this

temperature distribution over the diode array region. There are several features which are

particularly relevant. First, because the heat flux is based upon the derivative of the

temperature, and differentiation inherently exacerbates any noise present in the base

signal, this surface is a great deal less smooth than the temperature was. Notice that the

small ridge pointed out above becomes a sharp peak surrounded by deep furrows. A

similar pattern is similarly evident running in the x-direction near the top of the array;

148

this, too, corresponds to a small irregularity, running row-wise this time. Second, notice that the dimple corresponds to a sharp decrease in the substrate conduction; the heat transfer in this region is actually negative, indicating that the heat transfer is out of the substrate, rather than into it. Finally, notice that around the edges, there is a sharp decrease in substrate conduction. Unlike in the vicinity of the dimple, where the decrease was associated with enhanced heat transfer to the fluid in the stagnation region, the decrease here is a numerical artifact produced by the discontinuity in the boundary conditions and is not of any physical significance. This will be even more apparent in the discussion of the local heat transfer coefficient that follows.

At this point, everything necessary to determine the local heat transfer coefficients is known. Eq. 38 sets the relationship out mathematically:

$$h_{local}(x,y) = \frac{q''_{heater} - q''(x,y)}{\Delta T(x,y)} \tag{38}$$

Evaluating this equation over the surface produces the result shown in Figure 90. The sharp peak corresponding to the stagnation region is easily seen, and the false increase around the perimeter is also clearly evident.
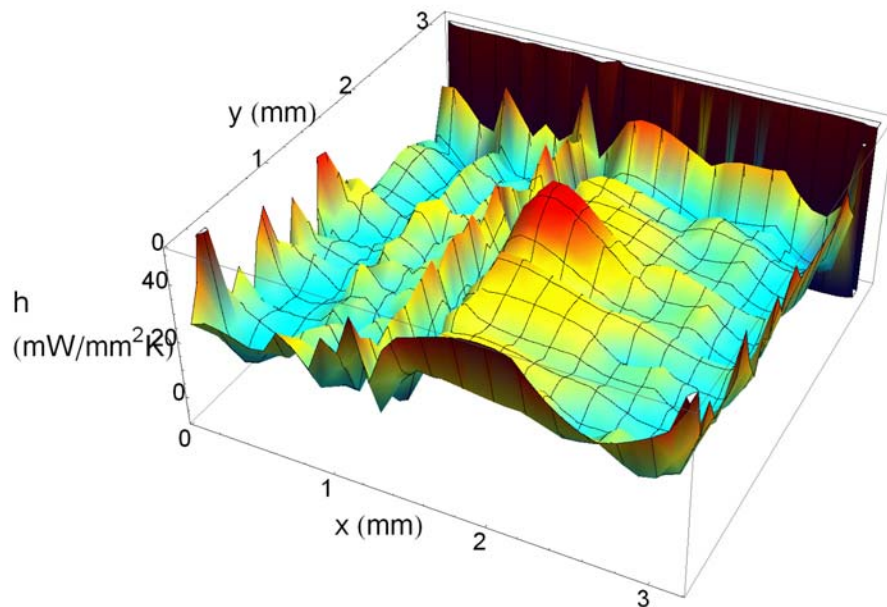
Figure 90   Local heat transfer coefficients

To more easily compare the experimentally determined heat transfer coefficients

to the correlations, these values were radially averaged. Starting from the nozzle location,

all of the known good diodes at a given radius were selected, and the mean and standard

deviation of the heat transfer coefficients at those locations were calculated; this process

was repeated up to a radius of 1.4 mm, covering the linear extent of the diode array.

Although the procedure could have been extended further — the most distant diodes, the

corners, are 2.1 mm away from the nozzle location — once the selection begins to include

the perimeter diodes, the erroneous values due to edge effects dominate the average.

After performing the radial averaging, the experimental results can be compared to the

correlations. Figures 91 – 98 show the measured heat transfer coefficients compared to

the predictions based on the four correlations discussed above. In the plots that follow,

the error bars denote the standard deviation of the measurements at that radius..
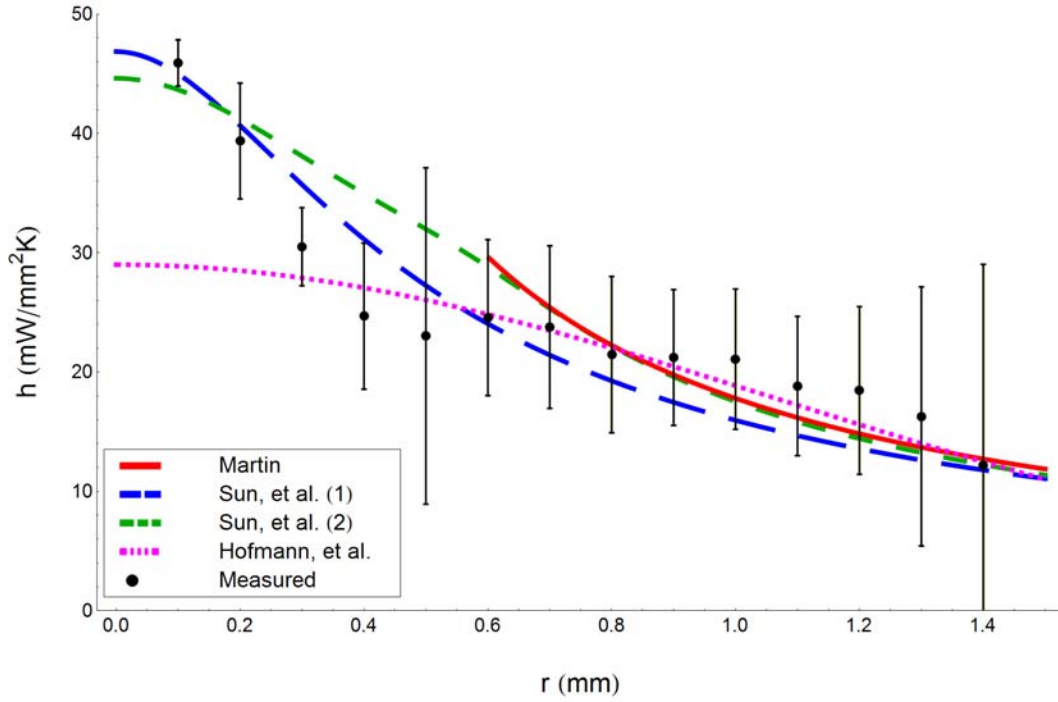
Figure 91   Heat transfer coefficient comparison for q_{heater} = 19.9 W/cm², v_{jet} =11.5 m/s, z/D = 6
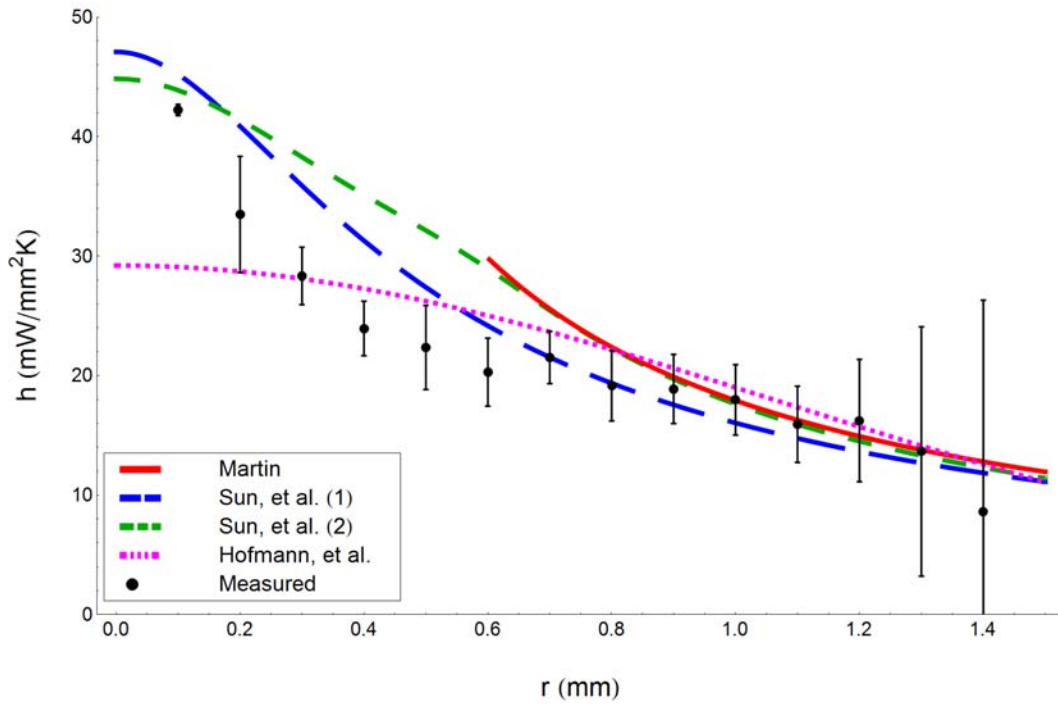
Figure 92   Heat transfer coefficient comparison for q_{heater} = 60.9 W/cm², v_{jet} =11.7 m/s, z/D = 6
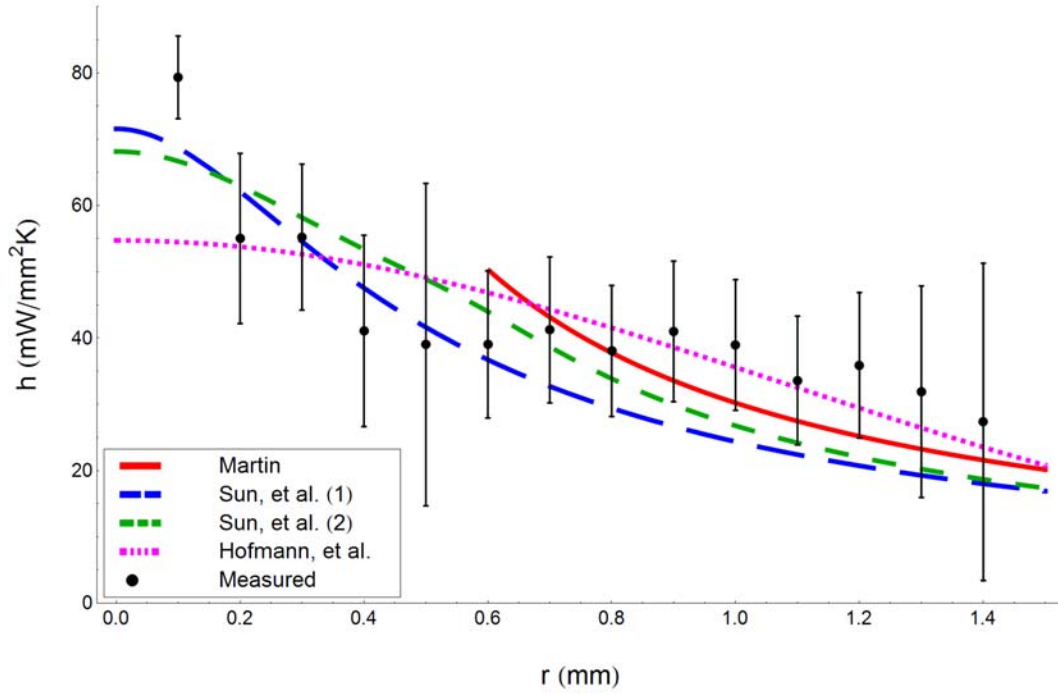
Figure 93   Heat transfer coefficient comparison for q_{heater} = 19.9 W/cm^2, v_{jet} =26.9 m/s, z/D = 6
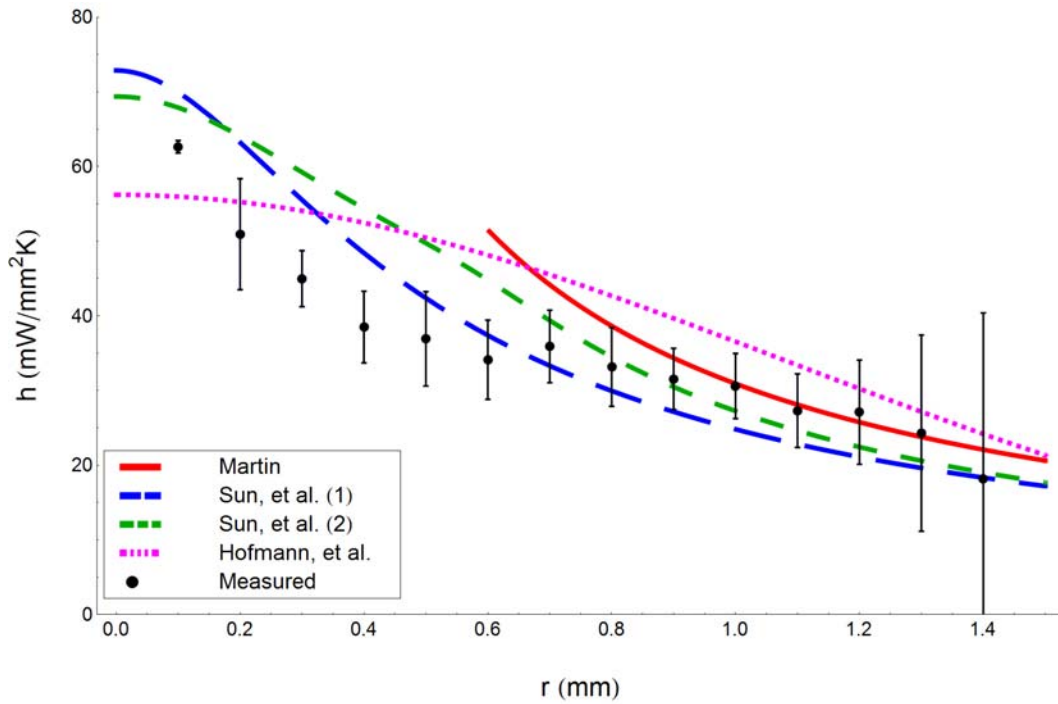
Figure 94   Heat transfer coefficient comparison for q_{heater} = 60.9 W/cm^2, v_{jet} =27.9 m/s, z/D = 6
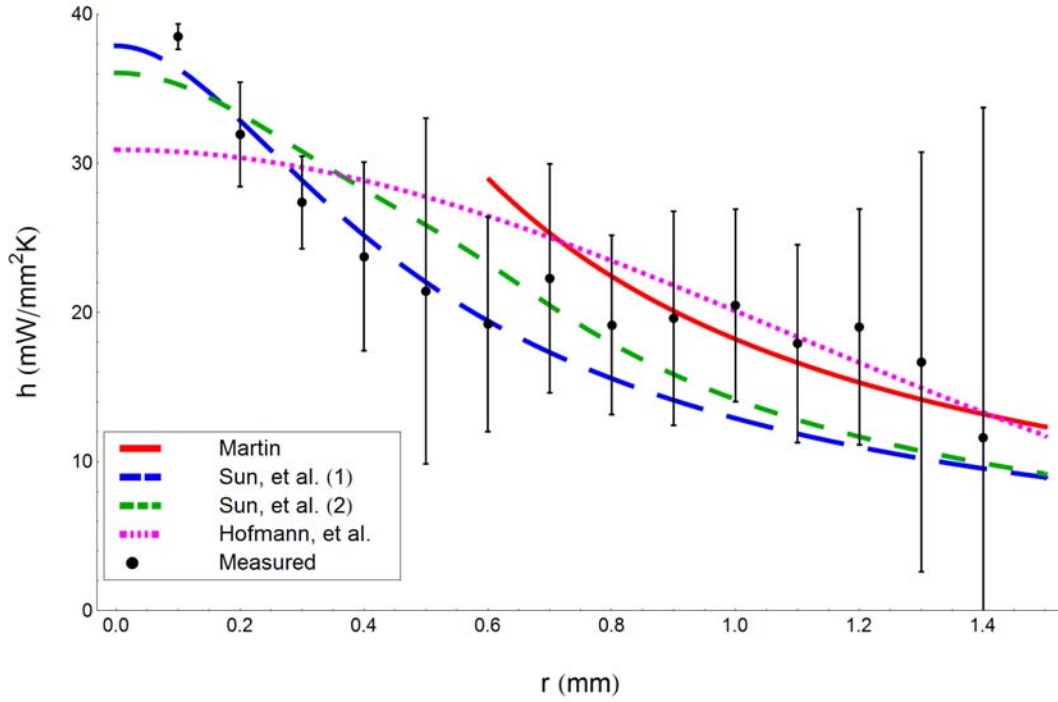
Figure 95   Heat transfer coefficient comparison for q_{heater} = 19.9 W/cm^2,
               v_{jet} =12.6 m/s, z/D = 10
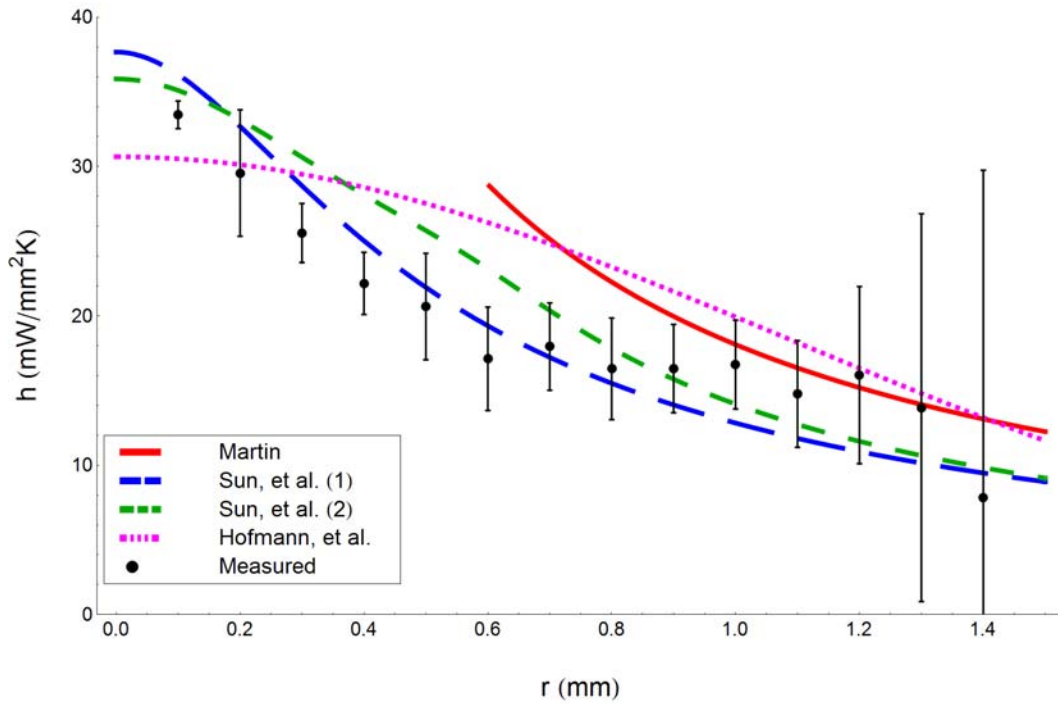
Figure 96   Heat transfer coefficient comparison for q_{heater} = 60.9 W/cm^2,
               v_{jet} =12.4 m/s, z/D = 10
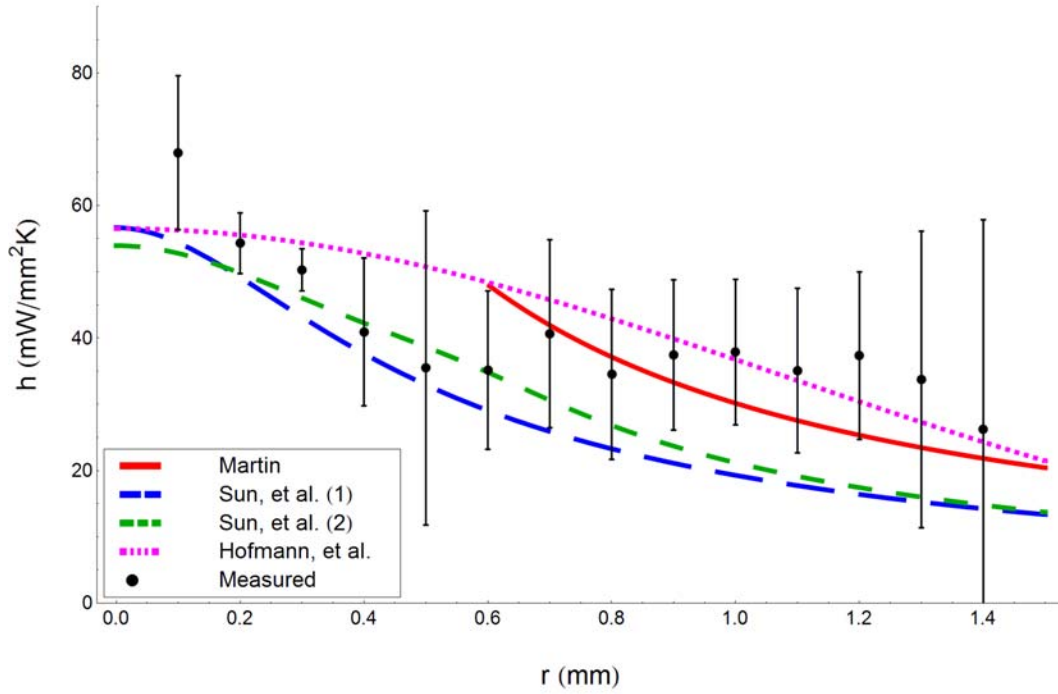
Figure 97   Heat transfer coefficient comparison for q_{heater} = 19.9 W/cm^2, v_{jet} =28.1 m/s, z/D = 10
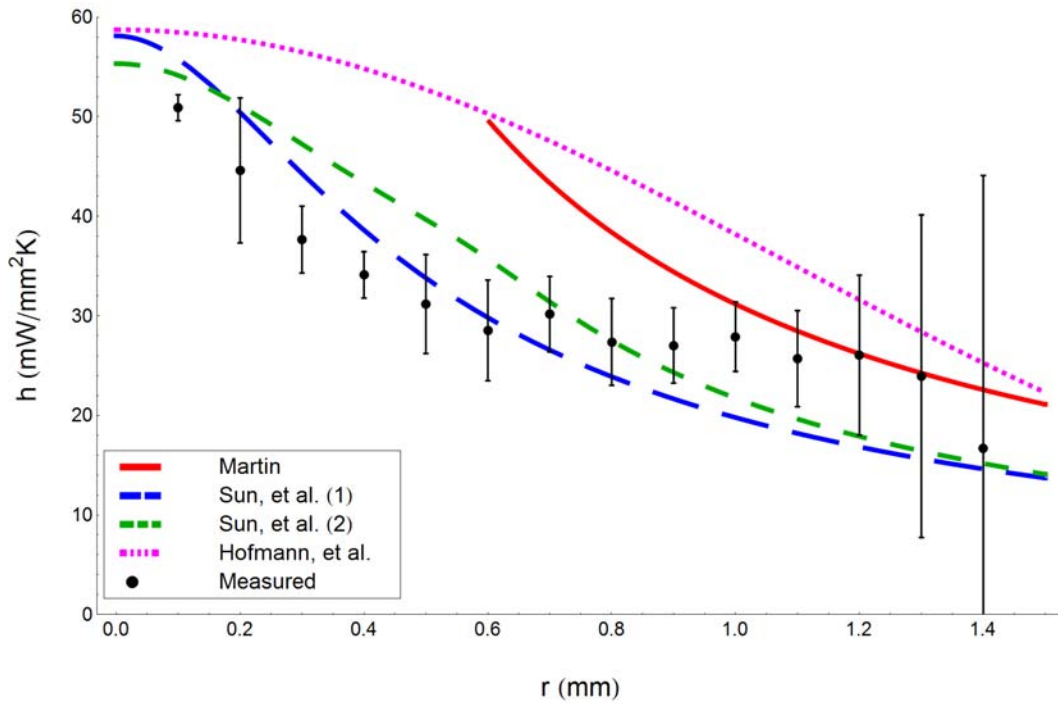
Figure 98   Heat transfer coefficient comparison for q_{heater} = 60.9 W/cm^2, v_{jet} =29.6 m/s, z/D = 10

Examining these plots, several features are evident. First are the general trends of

the data. For small radii, the heat transfer coefficient exhibits a decreasing trend, while

for large radii, the data level off and become approximately constant. In each data set, the

change in the trends occurs at the same location — $r = 0.5$ mm, corresponding to $r/D \approx 2$.

Other researchers have found that this location is significant in their experiments as well.

Sun, et al. [37] observe a "sharp knee" in their data at $r/D = 1.9$, and Li and Garimella

[39]also describe the stagnation region as extending to $r = 1.9$ D.

Next, compare the trends in the data to the correlations. In the stagnation region,

the correlations tend to over-predict the measured data. For five of the tests (1, 2, 4, 6,

and 8) the measured data fall below the predictions, while in three tests (3, 5, and 7) the

data are close to the predictions. In the wall region, the correlations tend to under-predict

the measured values. For six of the tests (1, 3, 5, 6, 7, 8) the data exceed the predicted

values, while in two tests (2 and 4) the data are close to the predictions. It is interesting

that in the stagnation region, there are no tests in which the data generally exceed the

predicted values (although in test 7, the single point at $r = 0.1$ mm lies above the

predictions, the remaining points agree with the predictions), while in the wall jet region,

there are no test in which the data fall below the predictions. Also, there are no tests in

which both the stagnation and wall jet regions show agreement between the data and

predictions.

The second feature that is readily evident is the broad scatter present at many of

the data points. In general, the scatter remains constant over much of the radial distance,

but sharply increases for the farthest radii ($r = 1.3$, 1.4 mm). This is probably because of

the irregular heat transfer coefficients calculated near the top edge of the array (in the vicinity of the y = 3 mm line in Figure 90). Also, in some plots — 79, 81, 83, and 85 — the data associated with r = 0.5 mm shows considerably larger scatter than its neighbors. The reason for this is not clear, but the fact that this location corresponds to r/D ≈2 suggests that it might be related to the transition from the stagnation region to the wall jet region. Interestingly, the cases in which this occurs are all the low heat flux tests; this effect is not present in the high heat flux tests.

Comparing the measured heat transfer coefficient distributions to the predictions, the agreement is uneven. Table ? shows the comparison between the average heat transfer coefficients as measured and as determined using each of the four correlations. The scatter in the measured values is extreme, varying from 50 – 65% of the mean value. This is not unexpected, however, based on the surface variations evident in Figure 90. Comparing the average values to the predicted values, half of the comparisons are within 10% of the predicted values. Some interesting patterns are evident: the measured values agree better with Martin's predictions for low heat fluxes than for high. Similarly, the data better match Hofmann's predictions at low heat fluxes. Conversely, the data generally agree better with the values predicted by both of Sun's correlations for the high heat flux tests. Also, note that the data do not match Hofmann's correlation appreciably better in the high velocity than in the corresponding low velocity tests; this is interesting because, strictly speaking, Hofmann's correlation is not valid for the low Reynolds numbers associated with the low velocity. It is also interesting that even in the cases where the agreement with some correlations is quite poor, the agreement with an alternate

157

correlation is quite good. In test 7, for example, the comparison with Sun's correlations

is off by almost 60%, but the corresponding comparisons with Hofmann and Martin are

off by only about 6%. This trend is also evident in test 3, while the reverse is true for

tests 4 and 6 (better agreement with Sun than Hofmann or Martin).

Table 26   Average heat transfer coefficients (mW/mm^2)

Test	Measured	Martin	Sun (1)	Sun (2)	Hofmann
1: q- v- z-	20.0 ± 10.8	20.6 (-3 %)	18.7 (6.9%)	20.7 (-3.4 %)	19.6 (2.1 %)
2: q+ v- z-	17.3 ± 9.8	20.7 (-16.8 %)	18.8 (-8.3 %)	20.8 (-17.0 %)	19.7 (-12.6 %)
3: q- v+ z-	36.8 ± 16.0	35.0 (5.1 %)	28.6 (28.7 %)	31.6 (16.4 %)	37.0 (-0.5 %)
4: q+ v+ z-	29.5 ± 12.9	35.8 (-17.6 %)	29.1 (-1.3 %)	32.2 (-8.4 %)	38.0 (-22.3 %)
5: q- v- z+	18.8 ± 12.1	20.3 (-7.4 %)	15.1 (24.3 %)	16.7 (12.4 %)	20.9 (-9.9 %)
6: q+ v- z+	15.8 ± 10.9	20.2 (-21.9 %)	15.0 (4.8 %)	16.6 (-5.2 %)	20.7 (-23.9 %)
7: q- v+ z+	35.9 ± 18.7	33.7 (6.7 %)	22.6 (58.8 %)	25.0 (43.6 %)	38.2 (-5.9 %)
8: q+ v+ z+	26.4 ± 13.8	34.8 (-24.0 %)	23.2 (13.9 %)	25.7 (3.0 %)	39.7 (-33.4 %)

In addition to the comparing the average values, the degree of agreement can be

assessed by considering the maximum and rms variations between the predictions and the

measured values. Tables 27, 28, and 29 report the results of these calculations for each of

the Sun correlations and the Hofmann correlation. These results show that the agreement

between the measured values and the predictions is poorer for the local heat transfer

coefficients than for the average coefficients. However, as Figures 79 – 86 indicate, the

local agreement between the correlations themselves is not very good, suggesting that at

the local level, the jet impingement problem is perhaps not as well understood as first

believed. The rms comparisons between the Sun (1) and Hofmann correlations (Eqs 31

and 33, respectively) are shown in Table 30; for most of the tests, the rms error between

these correlations falls between 30 – 40%. In comparison with these values, the rms

errors in the neighborhood of 20 – 30% of the average are quite good.

Table 27   Local comparison to Sun (1) (Eq. 31)

Test	h_{avg} (mW/mm^2)	Max ($\|h_{pred} - h_{meas}\|$) (mW/mm^2)	% of avg (%)	Mean$((h_{pred} - h_{meas})^2)^{\frac{1}{2}}$ (mW/mm^2)	% of avg (%)
1	18.7	6.45	34.5	3.73	19.9
2	18.8	7.55	40.2	4.14	22.0
3	28.6	15.1	52.8	9.94	34.8
4	29.1	12.3	42.3	6.56	22.5
5	15.1	8.05	53.3	4.49	29.7
6	15.0	5.12	34.1	2.87	19.1
7	22.6	20.9	92.5	13.4	59.3
8	23.2	9.2	39.7	5.76	24.8

Table 28   Local comparison to Sun (2) (Eq. 32)

Test	h_{avg} (mW/mm^2)	Max ($\|h_{pred} - h_{meas}\|$) (mW/mm^2)	% of avg	Mean$((h_{pred} - h_{meas})^2)^{\frac{1}{2}}$ (mW/mm^2)	% of avg
1	20.7	10.3	49.8	4.80	23.2
2	20.8	11.9	57.2	6.00	28.8
3	31.6	13.8	43.7	9.61	30.4
4	32.2	15.9	49.4	8.47	26.3
5	16.7	7.37	44.1	4.29	25.7
6	16.6	6.03	36.3	3.70	22.3
7	20.0	19.9	99.5	12.0	60.0
8	25.7	9.59	37.3	6.35	24.7

Table 29   Local comparison to Hofmann (Eq. 33)

Test	h_{avg} (mW/mm^2)	Max ($|h_{pred} - h_{meas}|$) (mW/mm^2)	% of avg	Mean($(h_{pred} - h_{meas})^2)^{1/2}$ (mW/mm^2)	% of avg
1	19.6	17.0	86.7	5.68	29.0
2	19.7	13.1	66.5	4.47	22.7
3	37.0	24.8	67.0	8.51	23.0
4	38.0	14.0	36.8	8.85	23.3
5	20.9	7.72	36.9	4.04	19.3
6	20.7	9.12	44.1	5.13	24.8
7	38.2	15.3	40.1	8.03	21.0
8	39.7	21.8	54.9	14.8	37.3

Table 30   RMS comparisons between Sun(1) and Hofmann

Test	RMS ($h_{Sun1}, h_{hofmann}$) (mW/mm^2)	% of $h_{avg,Sun1}$ (%)	% of $h_{avg,Hofmann}$ (%)
1	7.02	37.5	35.8
2	7.02	37.3	35.6
3	9.94	35.8	26.9
4	10.3	35.3	27.0
5	5.95	30.5	28.5
6	5.88	30.3	28.4
7	15.1	51.6	39.4
8	16.0	53.3	40.2

Finally, the analyses discussed here have all been performed using only the heat

flux and temperature associated with known good diodes. An alternative approach would

use the full complement of diode positions and use the interpolated values for the known

bad diodes. The average heat transfer coefficient calculations were repeated to examine

the difference between the two approaches, and the results are presented in Table ?. For

each test, using the interpolated values rather than limiting the scope of the calculations to

only the actual measurements increases the average heat transfer coefficient in every test

case. Because the measured values tend to fall below the predictions, this might suggest

that the accuracy could be improved by using performing the calculations using the full

complement of measurements. However, doing so also increases the amount of scatter

associated with each test, in many cases by more than the average value increased. Thus

any apparent increase in agreement between the data and the predictions is probably

illusory, and little is gained by using the interpolated values rather than only the measured

values.

Table 31   Comparison between actual and interpolated temperatures

Test	Measured values only		Interpolated values	
	h_{avg} (mW/mm^2)	σ (mW/mm^2)	h_{avg} (mW/mm^2)	σ (mW/mm^2)
1	20.0	10.8	20.9	11.0
2	17.3	9.8	17.7	10.6
3	36.8	16.0	38.5	17.3
4	29.5	12.9	30.1	13.9
5	18.8	12.1	19.4	12.9
6	15.8	10.9	16.1	11.6
7	35.9	18.7	36.7	20.3
8	26.4	13.8	26.9	15.1

Conclusions

A jet impingement test was used to verify the ability of the diode array to determine both the local and average heat transfer coefficients; the experimental values were compared to the predictions of several correlations available in the literature. Qualitatively, the experimental results exhibit the expected trends, while quantitatively, the agreement is more uneven. In any given test, one or more correlations show a comparison that is better than 10%, while other correlations might differ by as much as 60%. Considering instead the deviation between the data and the local predictions, the errors tend to be in the neighborhood of 20 – 40%; while at first these values do not seem to indicate close agreement, the local deviations between the correlations themselves tend to be in the neighborhood of 35 – 40 %. In light of this, the 20 – 40 % errors in the experimental data are more reasonable by comparison.

Chapter 8: Conclusions and Recommendations

Statement of Objectives

A novel temperature sensor has been developed and demonstrated. As stated in Chapter 1, the objectives of the new sensor were:

- Incorporate a 32 × 32 array of diodes: this objective was achieved.

- Achieve 100 μm spatial resolution: this objective was achieved.

- Incorporate resistive heaters to produce up to 100 W/cm^2: this objective was achieved.

- Achieve 1 kHz data collection rate: this objective was not fully achieved. Because of reverse recovery effects, only a subset of the array can be successfully sampled at 1 kHz. Thus, although over the course of the present work, the array was often successfully operated at the 1 kHz measurement speed, for the validation tests, the measurement frequency was only 100 Hz. Also, the phenomenon used to verify the array functionality, jet impingement, does not have a significant transient character, so the ability to distinguish variations at even 100 Hz was not tested. Thus it would not be appropriate to claim that this objective was successfully achieved.

- Demonstrate the ability to measure the local heat transfer distribution for an impinging jet: this objective was achieved.

Summary

The new sensor uses a 32 × 32 array of diodes as temperature sensors; these diodes are multiplexed in such a way that the 1024 sensors in the array require only 64 leads for their electrical connections. Each diode measures $100 \times 100 \ \mu m^2$, so that the measurements are taken within a 10.24 mm² area. Thus the resolution and spatial bandwidth achieved by the new sensor greatly exceeds what has been demonstrated by other researchers using conventional thermocouple or RTD arrays. The new sensor also incorporates eight resistive heaters capable of supplying up to 100 W/cm²; the heaters require an additional 16 electrical connections, bringing the total number of connections to 80.

In addition to the diode array itself, the necessary supporting hardware and software were also developed. The supporting hardware consisted of an interface board that supplied the sensing current (using a constant +5 V source and a current limiting resistor) to each of the rows and handled the switching operations to activate successive columns of diodes for measurement. This board also included signal conditioning circuits that transformed the native -2 mV/°C temperature sensitivity to a +200 mV/°C output sensitivity. The supporting software controlled the two data acquisition cards for data collection. A second software program was written to determine the substrate conduction losses associated with the measured surface temperature distribution. The net heat flux supplied by the heaters was determined by subtracting these losses from the known power dissipated by the heaters. The local heat transfer coefficient was then determined by dividing the net local heat flux by the local temperature rise.

The new sensor was subjected to several characterization tests designed to develop a more thorough understanding of its properties. In addition to individual and whole-array voltage–temperature calibrations, these tests included a transient test indicating that the response time for the diodes was approximately 6 μs; this places an upper limit of approximately 5 kHz on the possible surface scan rate. Another characterization test demonstrated a technique for separating the contribution to the measured voltage drop by any parasitic resistance in the circuit from the voltage drop of the p-n junction itself. The last of these characterization tests identified diodes that provided unreliable or unreasonable measurements; some of these bad diodes could be explained as a result of physical damage to the array — for others, the cause of the faulty measurement are not clear.

Finally, the new sensor's ability to measure the surface temperature distribution was demonstrated using a jet impingement heat transfer experiment. A jet of FC-72 was delivered through a 26 gauge hypodermic needle, and the resulting surface temperature distribution was measured. Eight tests were performed, varying three experimental parameters — surface heat flux, nozzle exit velocity, and nozzle standoff distance. After determining the local heat transfer coefficient as described above, the results compared favorably to correlations available in the literature.

Recommendations for Future Work

Some suggestions for follow on work include:

• Test alternate diode designs:

It should be possible to redesign the p-n junction to improve the transient response. Several alternate designs could be tested to determine the degree to which the transient response can be improved and any resulting impact on the sensitivity. Other heater resistor topologies could be considered as well.

• Redesign the diode array:

In future array designs the missing diode should be included, giving a full complement of 1024 individual sensors. The purpose for omitting it — to facilitate micro-drilling an artificial nucleation site — was never fulfilled, and having the gap in the array effectively creates an open-circuit failure at that location. Also, the heater resistors should be redesigned to correspond more closely to the diode array dimensions rather than extend past the array as is the case in the current design.

Future work might also consider the effect of using a thinner substrate to reduce heat spreading and substrate conduction. Because of silicon's high thermal conductivity, lateral conduction tends to reduce temperature variations over the surface. The lateral conduction can be reduced, however, by making the silicon die thinner and attaching it to a less conductive substrate, such as quartz. A preliminary investigation into the feasability of such an approach was conducted using the quarter-package COMSOL model discussed in Chapter 5. To avoid regenerating the geometry, the total chip

thickness is assumed to remain constant; the thickness of silicon removed is assumed to be replaced by an equal thickness of a quartz substrate (thus if 0.1 mm of silicon is removed, 0.1 mm of quartz replaces it, so that the total thickness remains 0.25 mm). The surface boundary condition was set as shown in Figure 99, with the heaters dissipating 240 mW/mm^2 and a surface heat
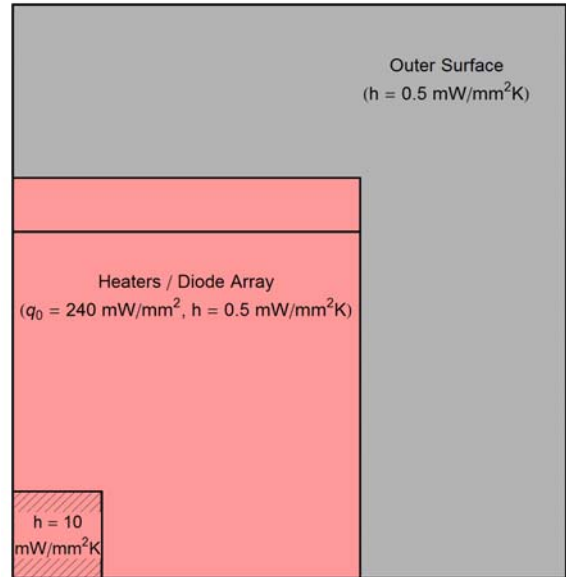
Figure 99   Surface boundary conditions for silicon thinning study

transfer coefficient of 0.5 mW/mm^2 K. A 0.4 × 0.4 mm^2 in the lower left corner of the surface (the center of the chip) is set to have a much higher heat transfer coefficient of 10 mW/mm^2 K, and the model is exercised for several silicon thicknesses.

This analysis finds that the silicon must be made very thin in order to have a noticeable effect. Table 32 shows the temperature difference between the 0.4 × 0.4 mm^2 region and the nearby surface. For the full silicon thickness, there is very little variation; the variation begins to become appreciable for a silicon thickness of about 100 μm, and becomes significant for thicknesses less than 50 μm.

Table 32   Effect of thinning the diode array silicon die

Silicon thickness (μm)	250	200	150	100	50	0
Quartz thickness (μm)	0	50	100	150	200	250
Temperature difference (°C)	0.57	0.71	0.95	1.4	3.1	83

- Redesign the interface board:

Several improvements to the interface board could be considered in future work. A constant current source, controlled by the data acquisition software, could be used to supply the sensing current, rather than the present +5 V and current limiting resistor topology. This would allow the parasitic resistance test to be automated and thus performed over the entire array. Additionally, the test could be performed over a range of temperatures; by doing so, the calibration would directly account for the effect of temperature-induced changes in the parasitic resistance. Also, to identify on-chip short circuit failures, the inactive side of the column switching should include current limiting resistors and indicator LEDs. In any redesign of the interface board, additional attention should be paid to EMI and noise issues. For example, the connection to the data acquisition system should use the compact 100-pin connector, which would allow the shielded cable to connect to the interface board directly. Also, the channels should be connected in a differential configuration, rather than single ended.

Appendix A: Numerical Routine Validation

The 3-D conduction solver described in Chapter 5 was validated by solving several 1-D and comparing the calculated results against known exact solutions for those conditions. The test domain was a $1 \times 1 \times 1$ mm^3 block. In order to distinguish each coordinate direction, the test block is discretized using different numbers of elements in each direction. As a second benefit, using different numbers of elements in each direction also provides some insight on the degree of grid dependence. This arrangement is shown in Figure 100; the step sizes are shown in Table 33.
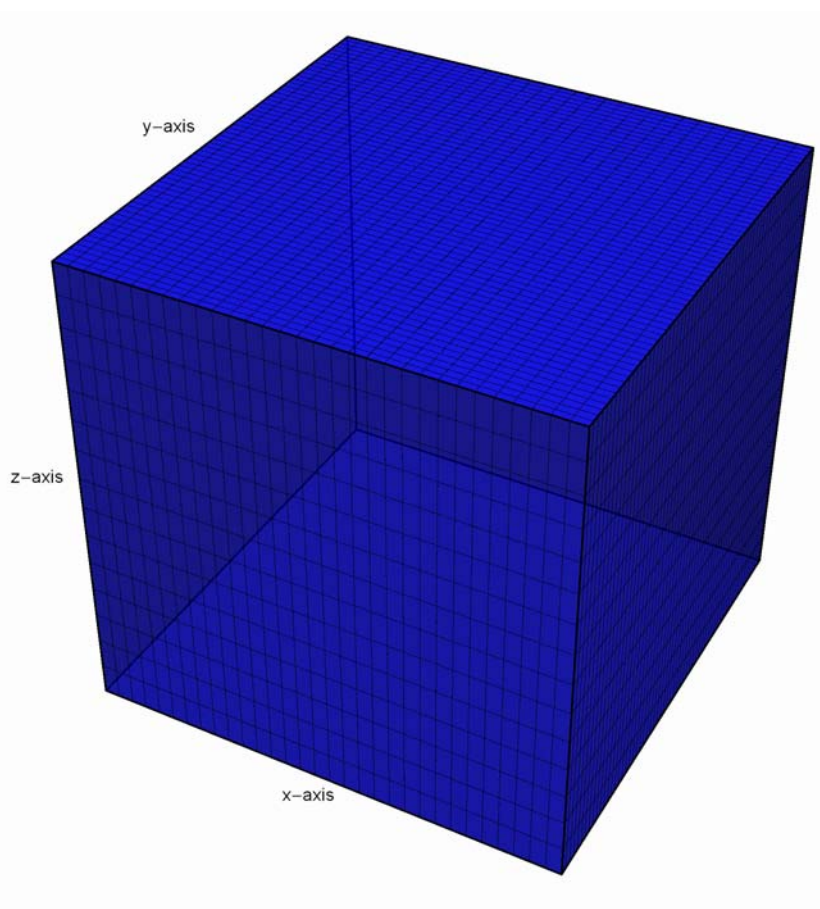
Figure 100   Validation test domain ($1 \times 1 \times 1$ mm^3)

Table 33   Test domain discretization

Coordinate Direction	x	y	z
Side length (mm)	1	1	1
Number of elements	31	61	16
Element length (mm)	0.0333	0.0167	0.0667

The 1-D cases were simulated by setting boundary conditions on the two surfaces in the coordinate direction of interest, and setting insulated conditions on the remaining four boundaries. This is illustrated in Figure ?. In each case, the two red surfaces (and their mates on the opposite sides of the domain) set as insulated, while the green face and its mate are set for the boundary conditions of interest.
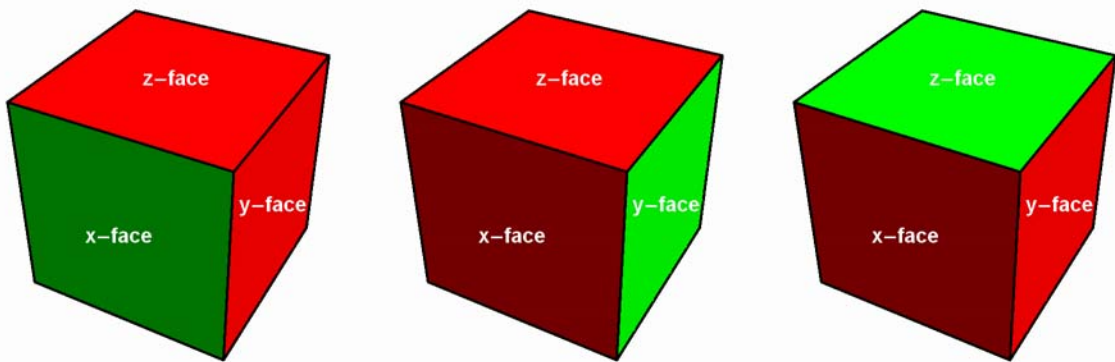
Figure 101   Validation domain 1-D approxiations

Two sets of 1-D boundary conditions were used. The first set assumes Dirichlet conditions, in which the two boundaries are set at different temperatures, as shown in Figure 102. The second set assumes Neumann and Robin conditions, with a constant heat flux imposed on one boundary and a convection coefficient assumed at the other, as shown in Figure 103.
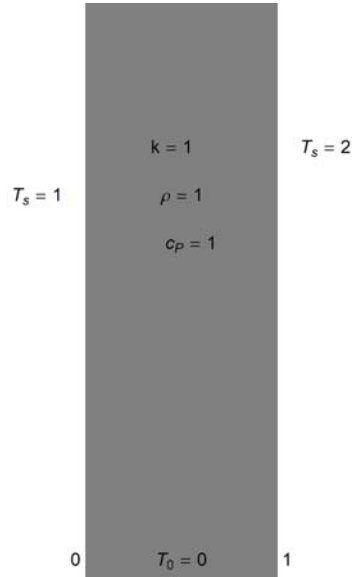
Figure 102   Dirichlet test conditions   Figure 103   Neumann test conditions
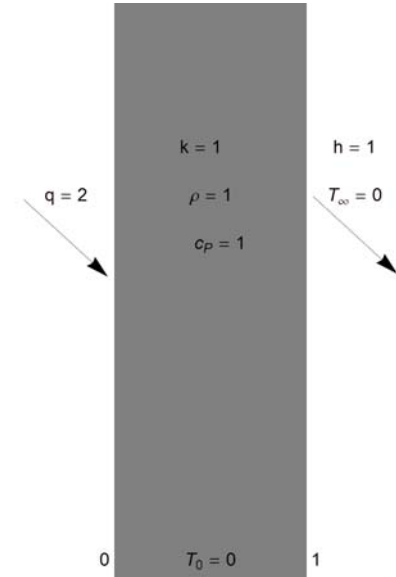
The exact solution for these two cases can be determined by solving the 1-D heat equation. For the Dirichlet conditions, the solution is given by Eq. 39:

$$T(x,t) = x + 1 + \sum_{n=1}^{\infty} A_n \exp\left(- (n\pi)^2 t \right) \sin(n \pi x)$$

$$where \quad A_n = \frac{\int_0^1 - (x+1) \sin(n \pi x) dx}{\int_0^1 \sin^2(n \pi x) dx} \tag{39}$$

For the Neumann conditions, the solution is given by Eq. 40:

$$T(x,t) = 4 - 2x + \sum_n B_n \exp\left(- \lambda_n^2 t \right) \cos(\lambda_n x)$$

$$where \quad B_n = \frac{\int_0^1 (2x - 4) \cos(\lambda_n x) dx}{\int_0^1 \cos^2(\lambda_n x) dx} \quad and \quad \lambda_n \tan \lambda_n = 1 \tag{40}$$

171

Both of these problems were solved for 1-D approximations in each of the x-, y- and z-directions for a total of six test cases; the results of these calculations follow. Two plots are presented for each test case: one plane surface used to assess the validity of the 1-D approximation and one plot comparing the results of the numerical calculation (individual points) against the appropriate exact solution (solid and dashed lines). Finally, Tables 34 and 35 summarize the results of the comparisons. Table 34 reports the comparisons for the Dirichlet conditions, and Table 35 reports the comparisons for the Neumann conditions.

Table 34   Dirichlet conditions comparisons

		t = 0.005	t = 0.05	t = 0.2	Steady state
x	$\mathrm{Max}(|T_{exact}-T_{adi}|)$	0.0573	0.00501	0.00298	0.000296
	$\mathrm{Mean}((T_{exact}-T_{adi})^2)^{1/2}$	0.0180	0.00252	0.00207	0.000205
y	$\mathrm{Max}(|T_{exact}-T_{adi}|)$	0.0567	0.00503	0.00279	0.000275
	$\mathrm{Mean}((T_{exact}-T_{adi})^2)^{1/2}$	0.0179	0.00265	0.00195	0.000191
z	$\mathrm{Max}(|T_{exact}-T_{adi}|)$	0.0569	0.00514	0.00364	0.000294
	$\mathrm{Mean}((T_{exact}-T_{adi})^2)^{1/2}$	0.0187	0.00241	0.00250	0.000201

Table 35   Neumann conditions comparisons

		t = 0.05	t = 0.5	t = 2.0	Steady state
x	$\mathrm{Max}(|T_{exact}-T_{adi}|)$	0.0134	0.00434	0.0227	0.0643
	$\mathrm{Mean}((T_{exact}-T_{adi})^2)^{1/2}$	0.00597	0.00283	0.0203	0.0628
y	$\mathrm{Max}(|T_{exact}-T_{adi}|)$	0.0128	0.00517	0.00810	0.00581
	$\mathrm{Mean}((T_{exact}-T_{adi})^2)^{1/2}$	0.00568	0.00427	0.00717	0.00514
z	$\mathrm{Max}(|T_{exact}-T_{adi}|)$	0.0157	0.00592	0.00827	0.00584
	$\mathrm{Mean}((T_{exact}-T_{adi})^2)^{1/2}$	0.00702	0.00481	0.00727	0.00517
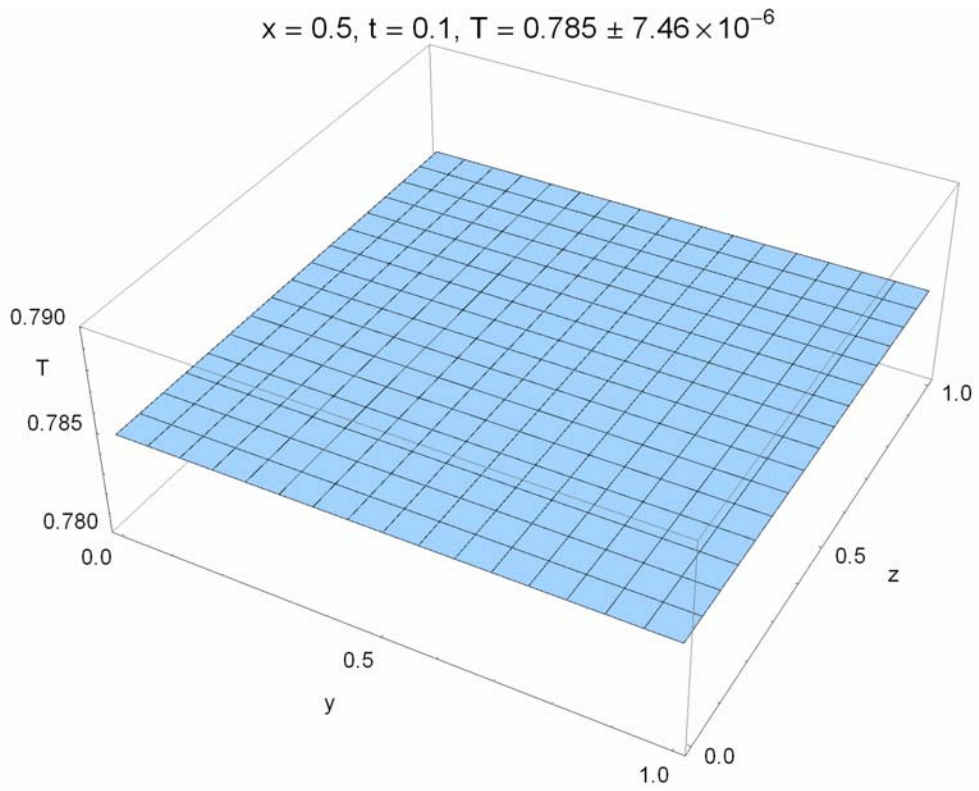
Figure 104   Sample 1-D slice (x-direction, Dirichlet conditions)
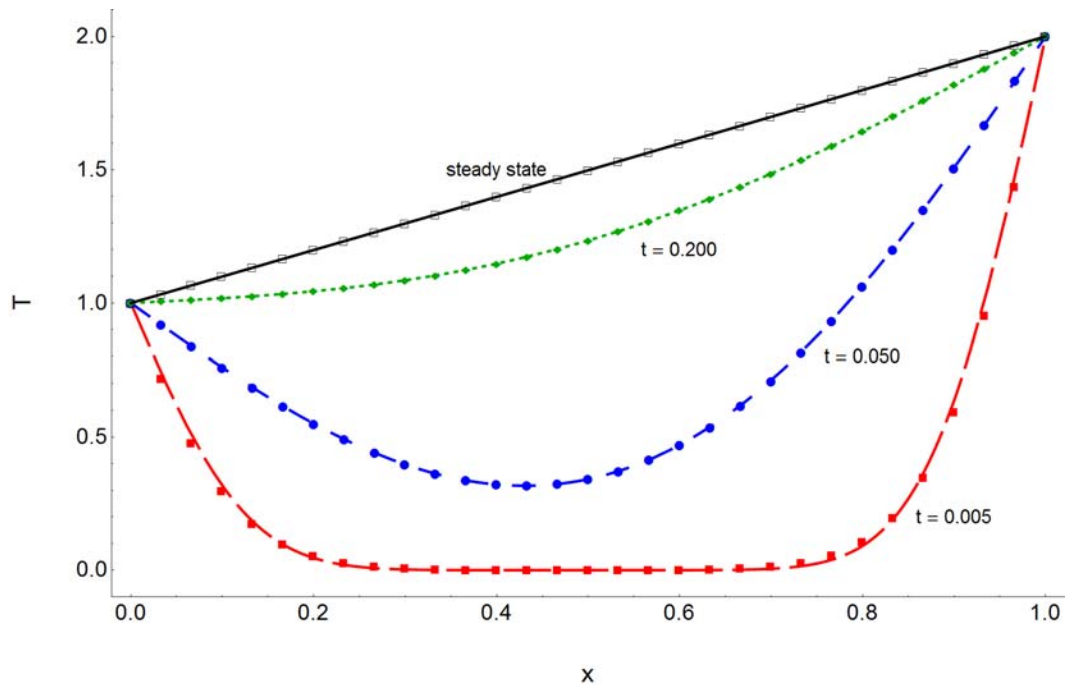
Figure 105   Comparison between exact and numerical solutions (x-direction,
              Dirichlet conditions)

173
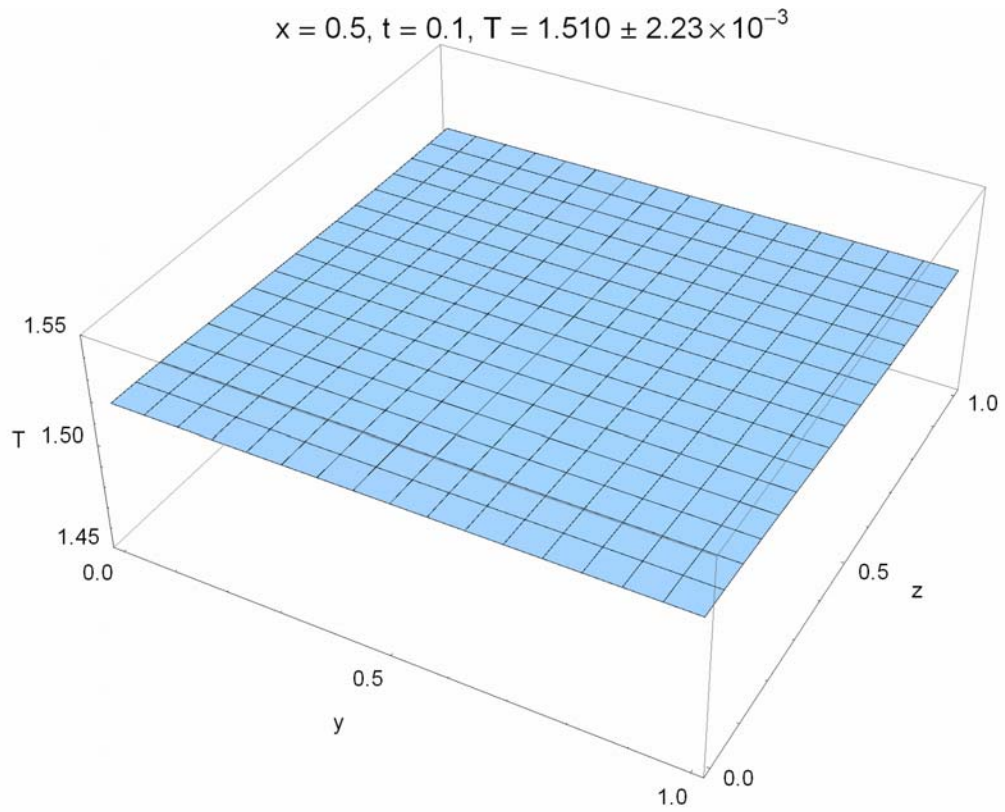
Figure 106   Sample 1-D slice (x-direction, Neumann conditions)
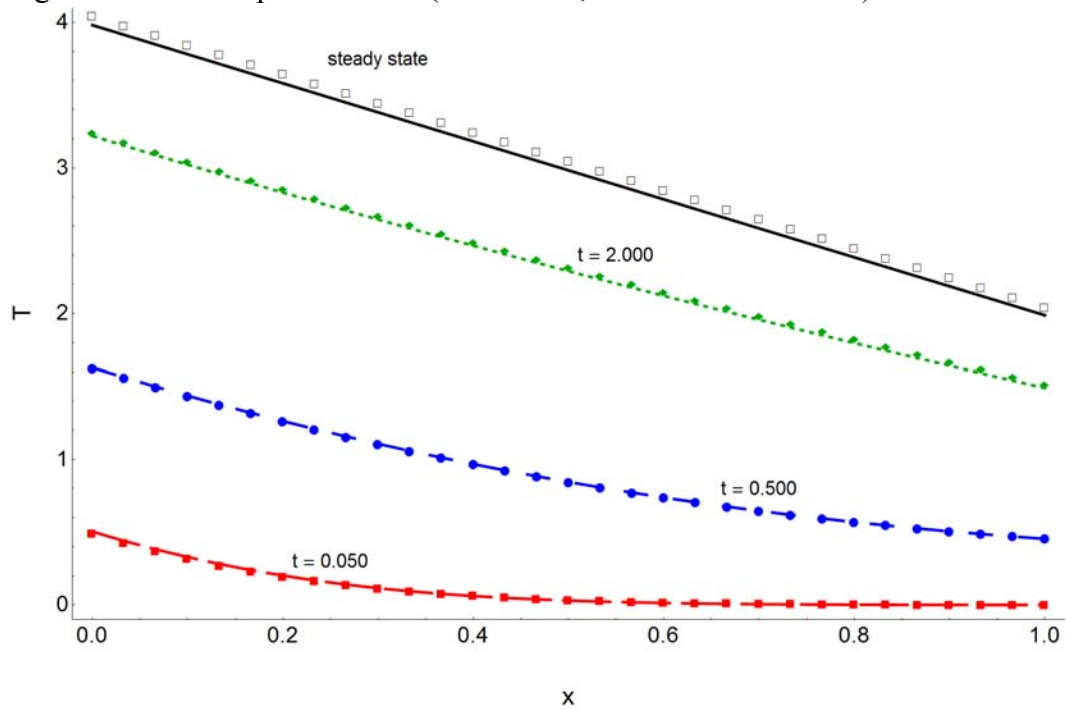
Figure 107   Comparison between exact and numerical solutions (x-direction, Neumann conditions)
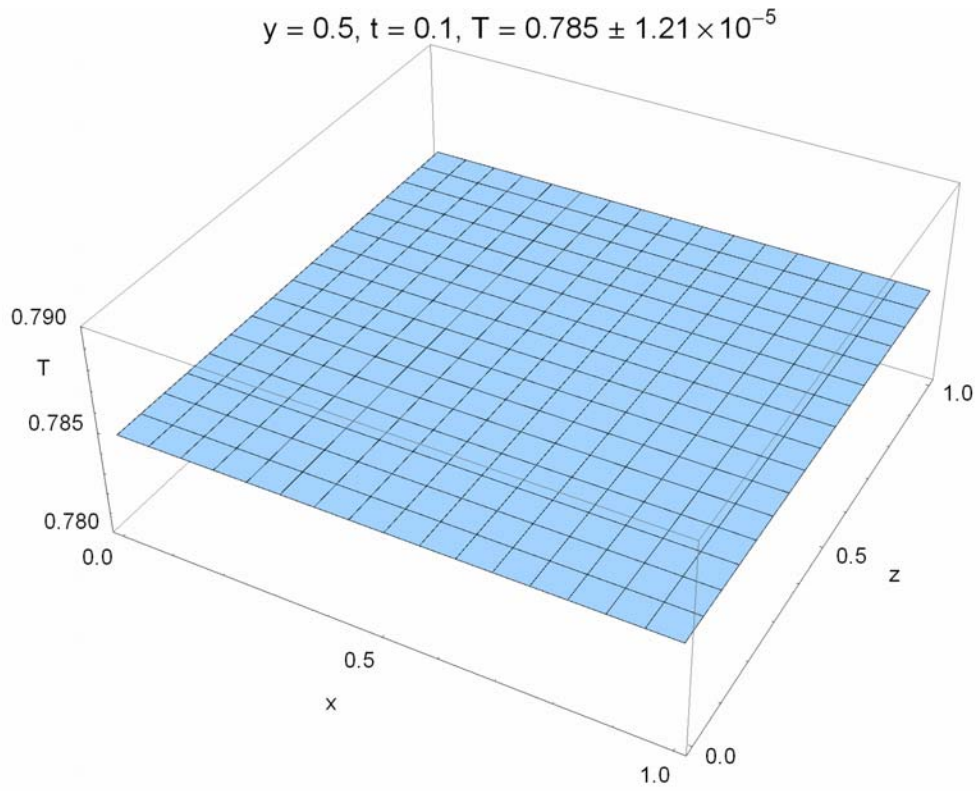
Figure 108   Sample 1-D slice (y-direction, Dirichlet conditions)
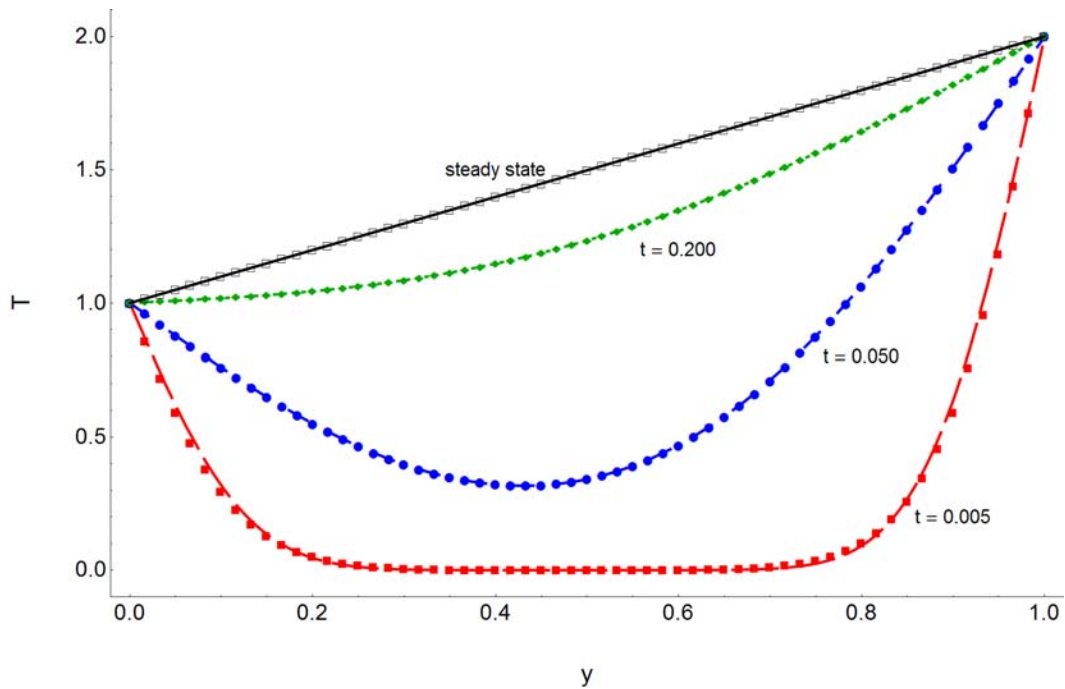
Figure 109   Comparison between exact and numerical solutions (y-direction, Dirichlet conditions)

175
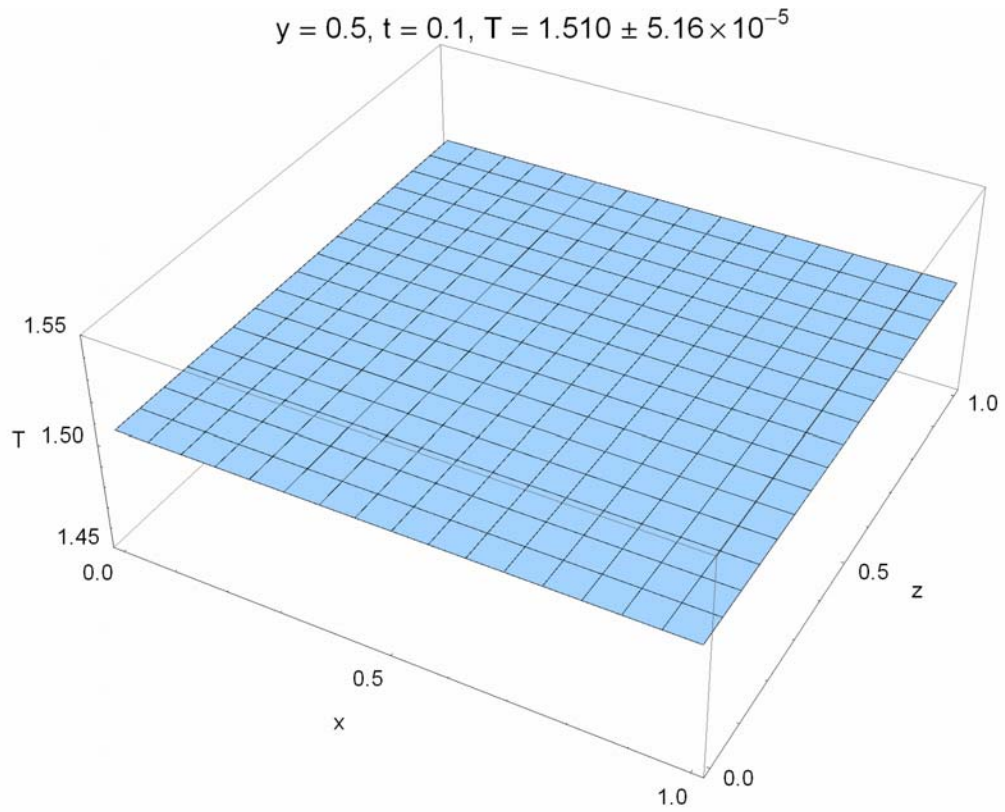
Figure 110   Sample 1-D slice (y-direction, Neumann conditions)
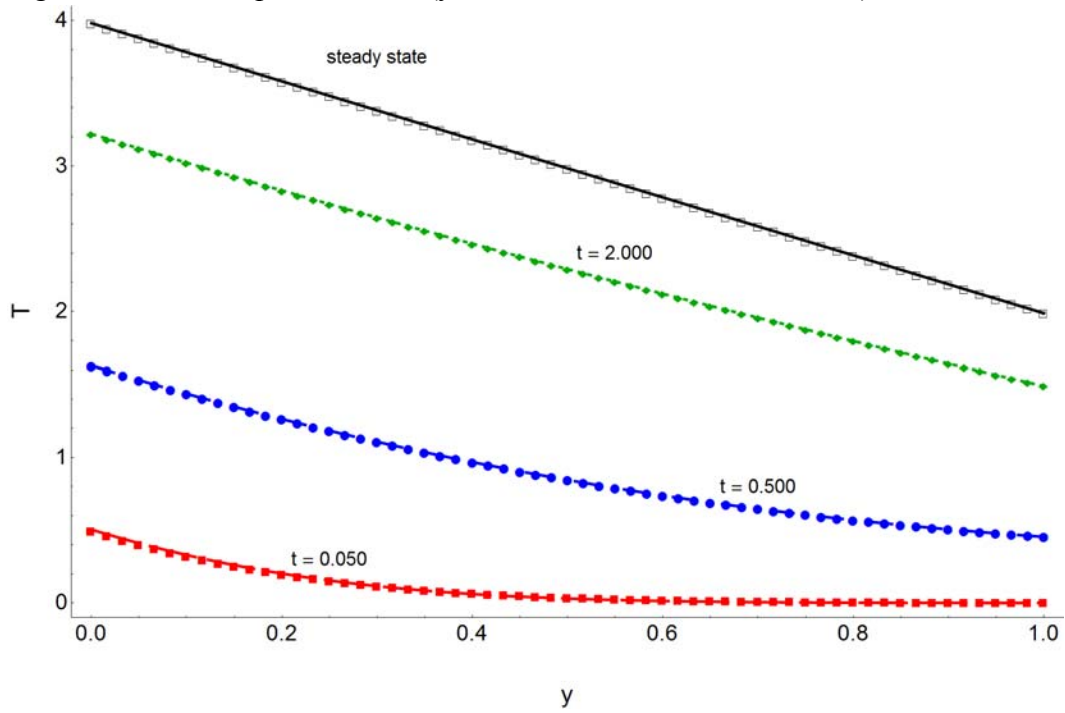
Figure 111   Comparison between exact and numerical solutions (y-direction,
              Neumann conditions)

176
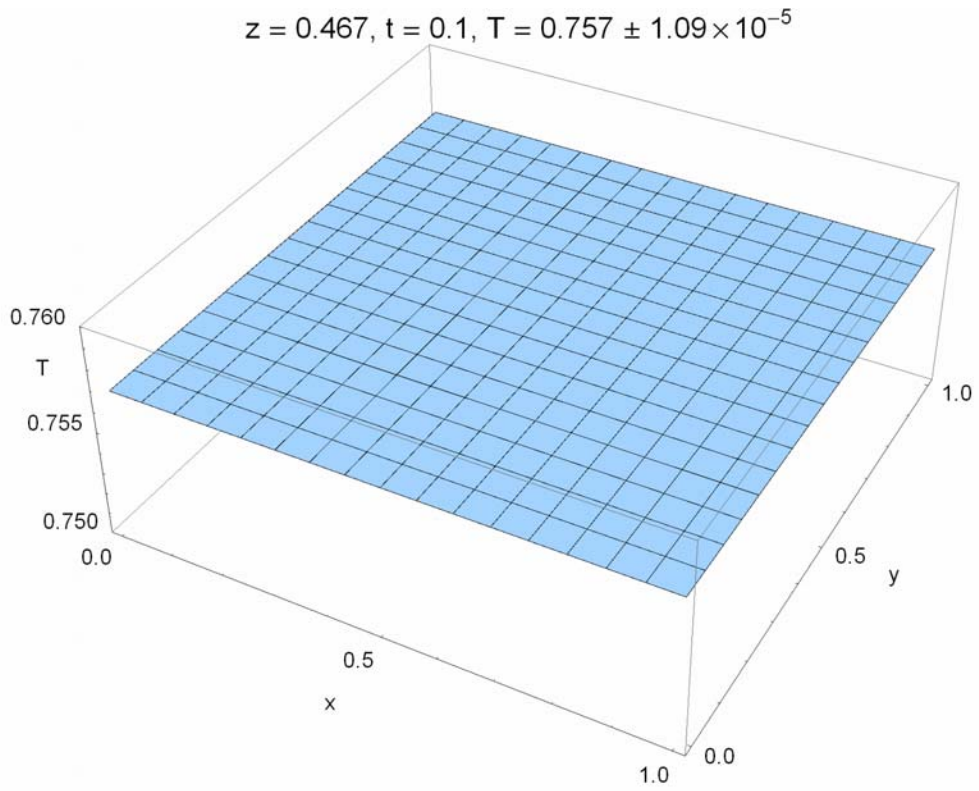
Figure 112   Sample 1-D slice (z-direction, Dirichlet conditions)
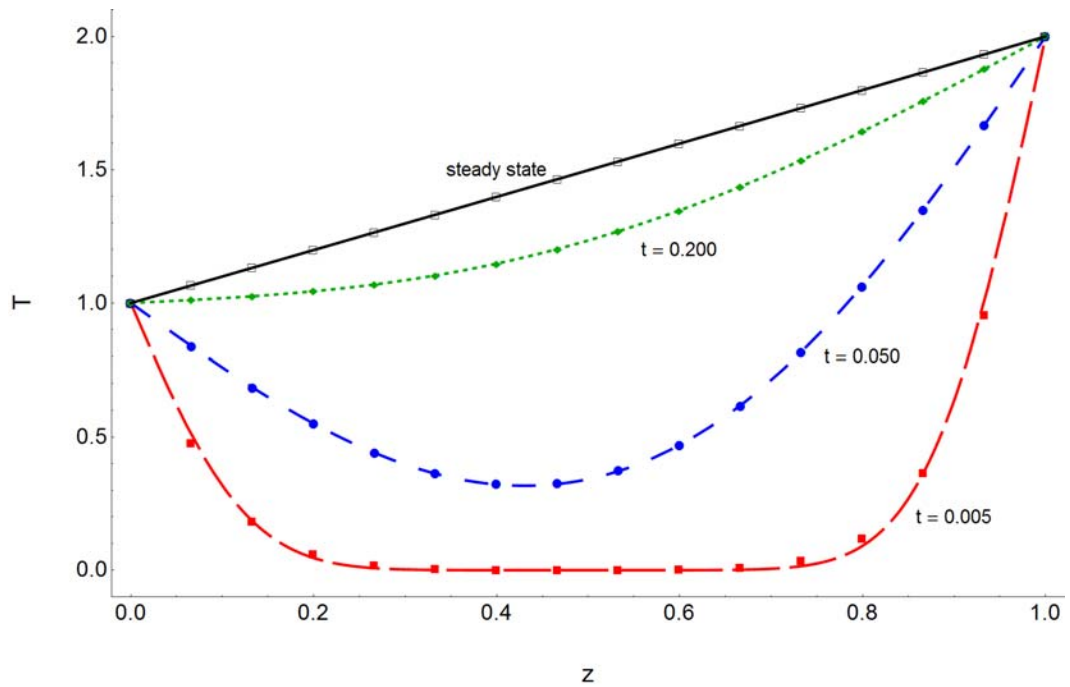
Figure 113   Comparison between exact and numerical solutions (z-direction, Dirichlet conditions)
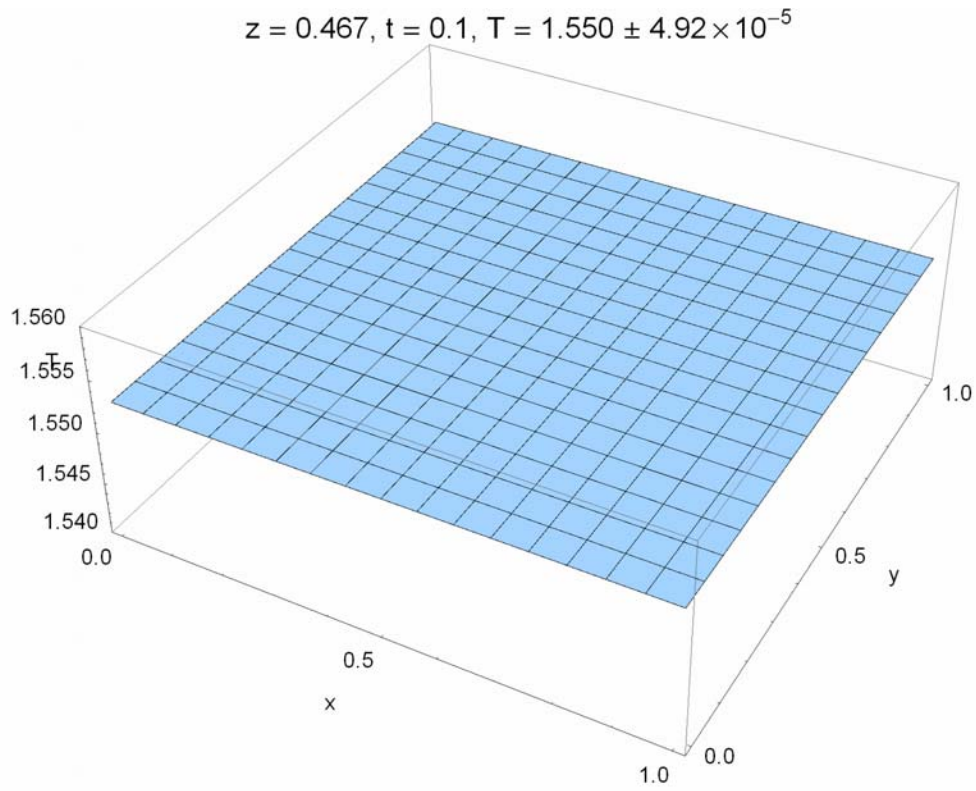
Figure 114   Sample 1-D slice (z-direction, Neumann conditions)
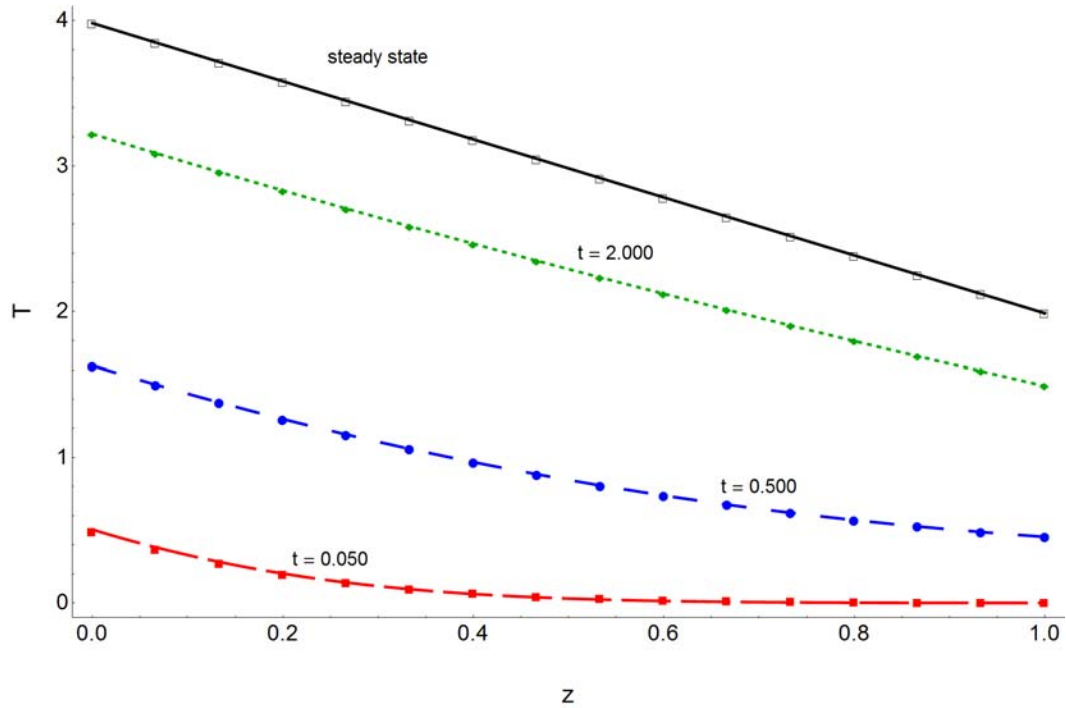
Figure 115   Comparison between exact and numerical solutions (z-direction, Neumann conditions)

References

1. Yang, W.-J.; Tsutsui, K. Overview of boiling on microstructures - Macro bubbles from micro heaters. Microscale Thermophysical Engineering 4[1], 7-24. 2000. Taylor and Francis Ltd.

2. Nukiyama, S. The maximum and minimum values of the heat Q transmitted from metal to boiling water under atmospheric pressure. *International Journal of Heat and Mass Transfer* **1966,** *9*, 1419-1433.

3. Coursey, J. S. Enhancement of spray cooling heat transfer using extended surfaces and nanofluids. University of Maryland, College Park, MD.

4. Tong, L. S. and Tang, Y. S. Boiling heat transfer and two-phase flow. 1997. Washington D.C., Taylor & Francis. Series in chemical and mechanical engineering . Hewett, G. F. and Tien, C. L.

5. Carey, V. P. Liquid-vapor phase-change phenomena: An introduction to the thermophysics of vaporization and condensation processes in heat transfer equipment. 1992. Washington D.C., Hemisphere Publishing Corporation. Series in chemical and mechanical engineering. Hewitt, F. and Tien, C. L.

6. Kim, J. ENME 647: Multiphase flow and heat transfer. Oct 21, 2003. College Park, MD, University of Maryland, College Park.

7. Incropera, Frank P. and De Witt, David P. Fundamentals of heat and mass transfer. 1990. New York, John Wiley & Sons.

8. Martin, H. Heat and mas stransfer between impinging gas jets and solid surfaces. In *Advances in Heat Transfer*, Hartnett, J., Irvine, T. F.Jr., Eds.; Academic Press: New York, 1977; pp 1-60.

9. Webb, B. W.; Ma, C. F. Single phase liquid jet impingement heat transfer. In *Advances in Heat Transfer*, Hartnett, J., Irvine, T. F.Jr., Eds.; Academic Press: New York, 1995; pp 105-217.

10. Zuckerman, N.; Lior, N. Jet impingement heat transfer: physics, correlations, and numerical modeling. In *Advances in Heat Transfer*, Hartnett, J., Cho, Y. I., Bar-Cohen, A. , Eds.; Elsevier Inc: New York, 2006; pp 565-631.

11.   Feynman, Richard P., Leighton, Ralph, and Sands, Matthew. Feynman lectures on physics. 1. 1963. Reading, MA, Addison Wesley.

12.   Quinn, T. J. *Temperature;* Academic Press: London, 1983.

13.   Coyne, G. S. *The laboratory companion: a practical guide to materials, equipment, and technique;* John Wiley and Sons, Inc.: New York, 1997.

14.   Middleton, W. E. K. *A history of the thermometer and its use in metrology;* The Johns Hopkins Press: Baltimore, MD, 1966.

15.   Bureau International des Poids et Mesures. The international system of units (SI). 2006.

16.   Childs, P. R. N. Advances in temperature measurement. In *Advances in Heat Transfer* , Hartnett, J., Irvine, T. F.Jr., Eds.; Academic Press : New York, 2002; pp 111-181.

17.   Theofanous, T. G.; Tu, J. P.; Dinh, A. T.; Dinh, T. N. The boiling crisis phenomenon Part I: nucleation and nucleate boiling heat transfer. Experimental Thermal and Fluid Science 26, 775-792. 2002.

18.   Hofmann, H. M.; Kind, M.; Martin, H. Mesaurements on steady state heat transfer and flow structure and new correlations for heat and mass transfer in submerged impinging jets. *International Journal of Heat and Mass Transfer* **2007,** *50*, 3957-3965.

19.   Kohn, D.; Popa, S. Heat Transfer at Boiling of Aqueous Solutions of Substances with Limited Solubility. *Experimental Heat Transfer* **1999,** *12*, 193-202.

20.   Dally, J. W.; Riley, W. F.; McConnell, K. G. *Instrumentation for engineering measurements;* Second ed.; John Wiley and Sons, Inc.: New York, 1993.

21.   Berenson, P. J. Experiments on pool-boiling heat transfer. *International Journal of Heat and Mass Transfer* **1962,** *5*, 985-999.

22.   Han, C.-Y.; Griffith, P. The mechanism of heat transfer in nucleate pool boiling -- part 1 (bubble initiation, growth, and departure). *International Journal of Heat and Mass Transfer* **1965,** *8*, 887-904.

23.   Son, G.; Dhir, V. K.; Ramanujapu, N. Dynamics and heat transfer associated witha single bubble during nucleate boiling on a horizontal surface. *Transactions of the ASME Journal of Heat Transfer* **1999,** *121*, 623-631.

24.   Héas, S.; Robidou, H.; Raynaud, M.; Lallemaud, M. Onset of transient nucleate boiling from a thick flat sample. *International Journal of Heat and Mass Transfer* **2003,** *46*, 355-365.

25.   Yu, C.-L.; Mesler, R. B. A Study of nucleate boiling near the peak heat flux through measurement of transient surface temperature. *International Journal of Heat and Mass Transfer* **1977,** *20*, 827-840.

26.   Qi, Y.; Klausner, J. F.; Mei, R. Role of surface structure in heterogenous nucleation. *International Journal of Heat and Mass Transfer* **2004,** *47*, 3097-3107.

27.   Qi, Y.; Klausner, J. F. Heterogeneous nucleation with artificial cavities. In *Proceedings of the ASME Summer Heat Transfer Conference*; American Society of Mechanical Engineers, New York, NY 10016-5990, United States: San Francisco, CA, United States, 2005; pp 79-89.

28.   Chen, J. C.; Hsu, K. K. Heat transfer during liquid contact on superheated surfaces. *Journal of Heat Transfer* **1995,** *117*, 693-697.

29.   Liaw, S. P.; Dhir, V. K. Void fraction measurements during saturated pool boiling of water on partially wetted vertical surfaces. *Journal of Heat Transfer* **1989,** *111*, 731-738.

30.   Wayner Jr., P. C.; Coccio, C. L. Heat and mass transfer in the vicinity of the triple interline of a meniscus. AIChE Journal 17[3], 569-74. 1971.

31.   Buchholz, M. ; Luttich, T.; Auracher, H.; Marquardt, W. Experimental investigation of local processes in pool boiling along the entire boiling curve. *International Journal of Heat and Mass Transfer* **2004,** *25*, 243-261.

32.   Vader, D. T. ; Incropera, F. P.; Viskanta, R. Local convective heat transfer from a heated surface to an impinging, planar jet of water. *International Journal of Heat and Mass Transfer* **1991,** *34* (3), 611-623.

33.   Wolf, D. H.; Viskanta, R.; Incropera, F. P. Turbulence dissipation in a free-surface jet of water and its effect on local impingement heat transfer from a heated surface: part 2 -- local heat transfer. *Journal of Heat Transfer* **1995,** *117*, 95-103.

34.   Stevens, J.; Webb, B. W. Local heat transfer coefficients under an axisymmetric, single-phase liquid jet. *Journal of Heat Transfer* **1991,** *113*, 71-78.

35.   Womac, D. J. ; Ramadhyani, S.; Incropera, F. P. Correlating equations for impingement cooling of small heat sources with single circular liquid jets. *Journal of Heat Transfer* **1993,** *115*, 106-115.

36.   Mohanty, A. K.; Tawfek, A. A. Heat transfer due to a round jet impinging normal to a flat surface. *International Journal of Heat and Mass Transfer* **1993,** *36* (6), 1639-1647.

37.   Sun, H.; Ma, C. F.; Nakayama, W. Local characteristics of convective heat transfer from simulated microelectronic chips to impinging submerged round water jets. *Journal of Electronic Packaging* **1993,** *115*, 71-77.

38.   Elison, B.; Webb, B. W. Local heat transfer to impinging liquid jets in the initially laminar, transitional, and turbulent regimes. *International Journal of Heat and Mass Transfer* **1994,** *37* (8), 1207-1216.

39.   Li, C.-Y.; Garimella, S. V. Prandtl-number effects and generalized correlations for confined and submerged jet impingement. *International Journal of Heat and Mass Transfer* **2001,** *44*, 3471-3480.

40.   Nukiyama, S.   The maximum and minimum values of the heat Q transmitted from metal to boiling water under atmospheric pressure. Journal of the Japanese Society of Mechanical Engineers 37, 367-374 . 1934. International Journal of Heat and Mass Transfer. 1996.

41.   Lurie, H.; Johnson, H. A. Tranisient pool boiling of water on a vertical surface with a step in heat generation. *Journal of Heat Transfer* **1962,** 217-224.

42.   Kim, J. H.; You, S. M.; Pak, J. Y. Effects of heater size and working fluids on nucleate boiling heat transfer. *International Journal of Heat and Mass Transfer* **2006,** *49*, 122-131.

43.   Cooper, M. G.; Lloyd, A. J. P. The microlayer in nucleate pool boiling. *International Journal of Heat and Mass Transfer* **1969,** *12*, 895-913.

44.   Rule, T. D.; Kim, J. Heat transfer behavior on small horizontal heaters during pool boiling of FC-72. Journal of Heat Transfer 121, 386-393. May, 1999.

45.   Kim, J.; Benton, J. F. Highly subcooled pool boiling heat transfer at various gravity levels. International Journal of Heat and Fluid Flow 23, 497-508. 2002.

46.   Kim, J.; Benton, J. F.; Wisniewski, D. Pool boiling heat transfer on small heaters: effect of gravity and subcooling. *International Journal of Heat and Mass Transfer* **2002,** *45*, 3919-3932.

47.   Henry, C. D.; Kim, J. Thermocapillary effects on low-g pool boiling from microheater arrays of various aspect ratio. Microgravity Science and Technology 15 [1], 170-175. 2005. ZARM Tec Publishing, Bremen, D 28359, Germany.

48.   Liu, Z.; Herman, C.; Kim, J. Heat transfer and bubble detachment in subcooled pool boiling from a microheater array under the effect of a nonuniform electric field. 2007 ASME/JSME Thermal Engineering Summer Heat Transfer Conference, HT 2007, Jul 8-12 2007 2, 263-270. 2007. Vancouver, BC, Canada, American Society of Mechanical Engineers, New York, NY 10016-5990, United States. 2007 Proceedings of the ASME/JSME Thermal Engineering Summer Heat Transfer Conference - HT 2007.

49.   Myers, J. G. ; Yerramilli, V. K.; Hussey, S. W.; Yee, G. F. ; Kim, J. Time and space resolved wall temperature and heat flux measurements during nucleate boiling with constant heat flux boundary conditions. *International Journal of Heat and Mass Transfer* **2005,** *48*, 2429-2442.

50.   Chen, T.; Klausner, J. F.; Garimella, S. V.; Chung, J. N. Subcooled boiling incipience on a highly smooth microheater. International Journal of Heat and Mass Transfer 49[23-24], 4399-4406. 2006. Elsevier Ltd, Oxford, OX5 1GB, United Kingdom.

51.   Moghaddam, S.; Kiger, K. T.; Modafe, A.; Ghodssi, R. A novel benzocyclobutene-based device for studying the dynamics of heat transfer during the nucleation process. Journal of Microelectromechanical Systems 16[6], 1355-1366. 2007. Institute of Electrical and Electronics Engineers Inc., Piscataway, NJ 08855-1331, United States.

52.   Lin, L.; Pisano, A. P.; Carey, V. P. Thermal bubble formation on polysilicon micro resistors. Journal of Heat Transfer, Transactions ASME 120[3], 735-742 . 1998. ASME, Fairfield, NJ, USA.

53.   Tsai, J.-H.; Lin, L. Transient thermal bubble formation on polysilicon micro-resisters. Micro/nanoscale heat transfer: Journal of Heat Transfer 124[2], 375-382. 2002. American Society of Mechanical Engineers, New York, NY 10016-5990, United States.

54.   Jung, J.-Y.; Lee, J.-Y.; Park, H.-C.; Kwak, H.-Y. Bubble nucleation on micro line heaters under steady or finite pulse of voltage input. International Journal of Heat and Mass Transfer 46[20], 3897-3907. 2003. Elsevier Ltd.

55.   Jung, J.-Y.; Kwak, H.-Y. Effect of surface condition on boiling heat transfer from silicon chip with submicron-scale roughness. International Journal of Heat and Mass Transfer 49[23-24], 4543-4551. 2006. Elsevier Ltd, Oxford, OX5 1GB, United Kingdom.

56.   Hallcrest *Handbook of thermochromic liquid crystal technology;* 1991.

57.   Ireland, P. T.; Jones, T. V. The response time of a surface thermometer employing encapsulated thermochromic liquid crystals. *Journal of Physics E: Scientific Instrumentation* **1987,** *20*, 1195-1199.

58.   Kenning, D. B. R. Wall temperature patterns in nucleate boiling. *International Journal of Heat and Mass Transfer* **1992,** *35* (1), 73-86.

59.   Ireland, P. T.; Jones, T. V. Liquid crystal measurements of heat transfer and surface shear stress. Measurement Science and Technology 11[7], 969-986. 2000. Institute of Physics Publishing, Bristol, Engl.

60.   Anderson, M. R.; Baughn, J. W. Hysteresis in liquid crystal thermography. Journal of Heat Transfer 126[3], 339-346. 2004. American Society of Mechanical Engineers, New York, United States.

61.   Kenning, D. B. R.; Yan, Y. Pool boiling heat transfer on a thin plate: features revealed by liquid crystal thermography. International Journal of Heat and Mass Transfer 39[15], 3117-3137. 1996. Pergamon Press Ltd, Oxford, Engl.

62.   McSharry, P. E.; Ellepola, J. H.; von Hardenburg, J.; Smith, L. A.; Kenning, D. B. R.; Judd, K. Spatio-temporal analysis of nucleate pool boiling: identification of nucleation sites using non-orthogonal empirical functions. *International Journal of Heat and Mass Transfer* **2002,** *45*, 237-253.

63.   Chin, Y.; Lakshminarasimhan, M. S.; Lu, Q.; Hollingsworth, D. K.; Witte, L. C. Convective heat transfer in vertical asymmetrically heated narrow channels. Journal of Heat Transfer 124[6], 1019-1025. 2002. American Society of Mechanical Engineers.

64.   Sodtke, C.; Kern, J.; Schweizer, N.; Stephan, P. High resolution measurements of wall temperature distribution underneath a single vapour bubble under low gravity conditions. International Journal of Heat and Mass Transfer 49[5-6], 1100-1106. 2006. Elsevier Ltd, Oxford, OX5 1GB, United Kingdom.

65.   Sodtke, C.; Schweizer, N.; Wagner, E.; Stephan, P. Experimental study of nucleate boiling heat transfer under low gravity conditions using TLCs for high resolution temperature measurements. 2006.

66.   Goldstein, R. J.; Franchett, M. E. Heat transfer from a flat surface to an oblique impinging jet. *Journal of Heat Transfer* **1988,** *110* , 84-90.

67.   Baughn, J. W.; Shimzu, S. Heat transfer measurements from a surface with uniform heat flux and an impinging jet. *Journal of Heat Transfer* **1989,** *111*, 1096-1098.

68.   Yan, X.; Baughn, J. W.; Mesbah, M. The effect of Reynolds number on the heat transfer distribution from a flat plate to an impinging jet. Metzger, D. E., Crawford, M. E., Eds.; ASME: 1992; pp 1-7.

69.   Harris, Herbert Jun, 1961.

70. McNamara, A. G. Semiconductor diodes and thransistors as electrical thermometers. *Review of Scientific Instruments* **1962,** *33* (3), 330-333.

71. Sclar, N.; Pollock, D. B. On diode thermometers. *Solid State Electronics* **1972,** *15*, 473-480.

72. Shwarts, Yu. M.; Borblik, V. L.; Kulish, N. R.; Venger, E. F.; Sokolov, V. N. Limiting characteristics of diode temperature sensors. Sensors and Actuators, A: Physical 86[3], 197-205. 2000. Elsevier Science B.V., Lausanne, Switzerland.

73. Treharne, R. W.; Riley, J. A. A linear response diode temperature sensor. Instrumentation Technology 25[6], 59-61. 1978.

74. Vader, D. T.; Chrysler, G. M.; Chu, R. C.; Simons, R. E. Experimental investigation of subcooled liquid nitrogen impingement cooling of a silicon chip. IEEE Transactions on Components, Packaging, and Manufacturing Technology Part A 18[4], 788-794. 1995. IEEE, Piscataway, NJ, USA.

75. Arik, M.; Bar-Cohen, A. Effusivity-based correlation of surface property effects in pool boiling CHF of dielectric liquids. International Journal of Heat and Mass Transfer 46[20], 3755-3764. 2003. Elsevier Ltd.

76. Pautsch, A. G.; Shedd, T. A. Spray impingement cooling with single- and multiple-nozzle arrays. Part I: Heat transfer data using FC-72. *International Journal of Heat and Mass Transfer* **2005,** *48*, 3167-3175.

77. Kim, J.; Whitten, M.; Quine, R. W.; Kalkur, T. S. Technique for measuring surface temperature fluctuations on a silicon wafer during boiling. In *American Society of Mechanical Engineers, Heat Transfer Division, (Publication) HTD*; ASME, Fairfield, NJ, USA: Anaheim, CA, USA, 1998; pp 197-202.

78. Han, I. Y.; Kim, S. J. Diode temperature sensor array for measuring micro-scale surface temperatures with high resolution. Sensors and Actuators, A: Physical 141[1], 52-58. 2008. Elsevier, Amsterdam, 1000 AE, Netherlands.

79. Massobrio, G.; Antognetti, P. *Semiconductor device modeling with Spice;* 2nd ed.; McGraw-Hill, Inc: New York, 1993.

80. Blackburn, D. L. Temperature measurements of semiconductor devices -- a review. 2004; pp 70-80.

81. Baker, R. J.; Li, H. W.; Boyce, D. E. *CMOS circuit design, layout, and simulation;* IEEE Press.

82.   "What is MOSIS?"; *http://www.mosis.com/about/whatis.html* (Retrieved: May 25,2008)

83.   "AMIS 1.5 micron ABN process"; *http://www.mosis.com/products/fab/vendors/amis/abn/* (Retrieved: May 25,2008)

84.   Tannehill, J. C.; Anderson, D. A.; Pletcher, R. H. *Computational fluid mechanics and heat transfer;* 2nd ed.; Taylor & Francis: Philadelphia, PA, 1997.

85.   Wang, T.-Y.; Lee, Y.-M.; Chen, C. C.-P. 3D thermal-ADI - An efficient chip-level transient thermal simulator. 2003 International Symposium on Physical Design, Apr 6-9 2003 , 10-17. 2003. Monterey, CA, United States, Association for Computing Machinery. Proceedings of the International Symposium on Physical Design.

86.   Zhou, D. W.; Ma, C. F. Radial heat transfer behavior of impinging submerged circular jets. *International Journal of Heat and Mass Transfer* **2006,** *49*, 1719-1722.